SURFACE OXIDATION AND DISSOLUTION OF METAL NANOCATALYSTS IN ACID MEDIUM

A Dissertation

by

JUAN RAFAEL CALLEJAS-TOVAR

Submitted to the Office of Graduate Studies of
Texas A&M University
in partial fulfillment of the requirements for the degree of

DOCTOR OF PHILOSOPHY

August 2012

Major Subject: Chemical Engineering

Surface Oxidation and Dissolution of Metal Nanocatalysts in Acid Medium

SURFACE OXIDATION AND DISSOLUTION OF METAL NANOCATALYSTS IN ACID MEDIUM

A Dissertation

by

JUAN RAFAEL CALLEJAS-TOVAR

Submitted to the Office of Graduate Studies of
Texas A&M University
in partial fulfillment of the requirements for the degree of

DOCTOR OF PHILOSOPHY

Approved by:

Chair of Committee,	Perla B. Balbuena
Committee Members,	Manuel P. Soriaga
	Hae-Kwon Jeong
	Victor Ugaz
Head of Department,	Charles Glover

August 2012

Major Subject: Chemical Engineering

ABSTRACT

Surface Oxidation and Dissolution of Metal Nanocatalysts in Acid Medium.

(August 2012)

Juan Rafael Callejas-Tovar, B.S., Instituto Tecnológico de Celaya, Guanajuato, México;
M.S., Instituto Tecnológico de Celaya, Guanajuato, México

Chair of Advisory Committee: Dr. Perla B. Balbuena

One of the most important challenges in low-temperature fuel cell technology is improving the catalytic efficiency at the electrode-catalyst where the oxygen reduction reaction (ORR) occurs. Platinum is the best pure catalyst for this reaction but its high cost and scarcity hinder the commercial implementation of fuel cells in automobiles. Pt-based alloys are promising alternatives to substitute platinum while maintaining the efficiency and life-time of the pure catalyst. However, the acid medium and the oxidation of the surface reduce the activity and durability of the alloy catalyst through changes in its local composition and structure. Molecular simulation techniques are applied to characterize the thermodynamics and dynamic evolution of the surface of platinum-based alloy catalysts under reaction conditions. A simulation scheme of the surface oxidation is proposed which combines classical molecular dynamics (MD) and density functional theory (DFT). This approach is able to reproduce the main features of the oxidation phenomena observed experimentally, it is concluded that the dissolution mechanism of metal atoms involves: 1) Surface segregation of alloy atoms, 2) oxygen absorption into the subsurface of the catalyst, and 3) metal detachment through the interaction with ions in the solvent. Therefore, to improve the durability of platinum-based alloy catalysts, the steps of the dissolution mechanism must be prevented.

A versatile 3-D kinetic Monte Carlo (KMC) code is developed to study the degradation and dealloying in nanocatalysts. The results on the degradation of Pt nanoparticles under different potential regimes demonstrate that the dissolution depends on the potential path to which the nanocatalyst is exposed. Metal atoms detach from the

boundaries of (111) facets expecting a reduction in the activity of the nanoparticle. Also, the formation of Pt hollow nanoparticles by the Kirkendall effect is addressed, the role of vacancies is crucial in the removal of the non-noble core that yields to hollow nanoparticles. To investigate the reasons for the experimentally found enhanced ORR activity in porous/hollow nanoparticles, the effect of subsurface vacancies on the main ORR activity descriptors is studied with DFT. It is found that an optimum amount of vacancies may enhance the ORR activity of Pt-monolayer catalysts over certain alloy cores by changing the binding energies of O and OH.

DEDICATION

To my family with love, there are no words to describe how grateful I am for your love and support.

ACKNOWLEDGEMENTS

I would like to thank my committee chair, Prof. Perla B. Balbuena for her valuable advice and support throughout the course of this research, as well as my committee members, Prof. Hae-Kwon Jeong, Prof. Manuel P. Soriaga, Prof. Victor Ugaz, and Prof. Haiyan Wang.

This work is supported by the Department of Energy, grant DE-FG02-05ER15729. The author acknowledges the following institutions for providing computing resources that were essential in the research reported in this dissertation: Texas A&M University Brazos HPC cluster, Texas A&M University Supercomputing Facility, Texas Advanced Computing Center (UT-Austin), Argonne National Laboratory, National Energy Research Scientific Computing Center (supported by the Office of Science of the U.S. Department of Energy under Contract No. DE-AC03-76SF00098), and Army Research Laboratory (ARL).

NOMENCLATURE

AFM	Atomic force microscopy
CF1	Central force 1 potential
CN	Coordination number
DFT	Density functional theory
EXAFS	Extended X-ray absorption fine structure
FCC	Face centered cubic
FRM	First-Reaction method
GGA	Generalized gradient approximation
HRTEM	High-Resolution transmission electron microscopy
KMC	Kinetic Monte Carlo
LJ	Lennard Jones potential
MD	Molecular dynamics
NSAs	Near-surface alloys
ORR	Oxygen reduction reaction
PAW	Projector augmented wave pseudo–potentials
PBC	Periodic boundary conditions
PBE	Perdew, Burke and Ernzerhof
PEMFC	Proton exchange membrane fuel cell
RDF	Radial distribution function
SPC/E	Single point charge model for water
STM	Scanning tunneling microscope
VASP	Vienna ab-initio simulation package
XPS	X-ray photoelectron spectroscopy

TABLE OF CONTENTS

Page

LIST OF FIGURES

Page

LIST OF TABLES

Page

CHAPTER I

INTRODUCTION

An important challenge in low-temperature fuel cell technology is improving the catalytic efficiency of the electrode-catalyst where the oxygen reduction reaction (ORR) takes place. The ORR is a kinetically slow reaction in which molecular oxygen is reduced and combines with protons producing water. Platinum is the most widely used electrocatalyst for the ORR in fuel cells. However, as a noble metal, Pt is extremely expensive and the relatively sluggish ORR kinetics on Pt surfaces limits its catalytic efficiency[1]. The electrocatalysis of the ORR is carried out on nanoparticles with the goal of employing the smallest amount of material that is able of maximizing the catalytic activity and stability. Pt-based alloy catalysts reduce the required amount of platinum and some of them have shown enhanced ORR activity compared to pure Pt catalysts, specifically the Pt_3Co alloy[2-4] and recently core-shell catalysts consisting of a Pt monolayer shell over cores made of porous/hollow Pd—Cu alloy,[5] acid treated Pt_3Co[2,6,7] alloy, or dealloyed $PtCu_3$[8,9] have demonstrated remarkable activity. In the case of the Pt_3Co alloy, the enhanced activity is partially attributed to the formation of a "Pt-skin" structure produced by an exchange of Pt and Co in the first two layers.[3] Recent studies have shown that the activity enhancement of Pt-based alloys varies from 2-4[3,10,11] to 10-25 times.[12] Since the detailed reaction mechanisms are not yet fully understood, the origin of the enhanced oxygen reduction activity remains unclear, although it is generally accepted that the effect can arise from the modification of surface geometries and/or electronic structures. Despite of their enhanced activity, Pt-based alloys catalysts exhibit dissolution during the fuel cell operation, decreasing their activity.[13]

The current challenge in designing metal electrode nanocatalysts in acid medium for low-temperature fuel cell technologies is not activity but durability. It has been reported that platinum electrode surface area loss significantly shortens the lifetime of fuel cells[14]. The existence of a correlation between the onset of the oxide formation and

---

This dissertation follows the style of *The Journal of Physical Chemistry C.*

the concentration of dissolved Pt has been found experimentally,[15] suggests that the surface oxide may play a critical role in the stability of ORR catalysts. The dissolution process may involve interactions between the topmost layers of the catalyst, atomic oxygen, oxygenated species, and the electrolyte. However, the actual mechanism of the dissolution process and particularly its effects on the catalyst structure are not well understood. For the ORR, various oxygenated species are likely to be adsorbed on the cathode catalyst surface.[16] At high oxygen concentrations, the formation of a surface oxide is associated with the initial stages of metal dissolution,[15] although there is still a controversy regarding the dissolution mechanism and the conditions (oxidation or reduction) that trigger maximum dissolution.[17] In previous work it has been shown using density functional theory (DFT) and ab initio molecular dynamics (MD) calculations that surface buckling effects are caused by adsorbed and absorbed oxygen as function of oxygen coverage,[18-21] and that acid species and solvent result in enhanced buckling and surface charges.[22] In summary it has been found that as the degree of surface oxidation increases, surface atoms experience different degrees of buckling which is enhanced by the presence of hydronium and other oxidants such as chloride ions. Buckling is a distortion of the position of the metal atoms with respect to such in the crystal structure.

In this work we address the effect of the adsorbed oxygen and its interactions with the solvent on the top surface layers as the degree of oxidation increases, equivalent to increasing electrochemical potentials. Variations in surface structure and composition are evaluated providing novel insights about the segregation of alloy atoms to the surface and surface reconstruction effects as the degree of oxidation increases. We recently proposed[23-25] a two-stage simulation approach combining DFT and classical MD that is able to provide information at a molecular level of the mechanisms of oxidation and metal dissolution that causes the degradation of ORR catalysts. The novelty of these simulations is that they are able to capture surface evolution under oxidation and reduction conditions. The model is able to capture such evolution including the segregation of Co atoms to the surface, migration of oxygen to the subsurface, place exchange between metal and oxygen atoms, and surface reconstruction.

Dealloying is the selective removal of elements from an alloy. According to recent experimental reports[26-28] dealloying taking place during the synthesis of ORR catalysts may yield to remarkable activity enhancement by creating characteristic porous or hollow structures. However, the dealloying process that occurs during the fuel cell operation causes the degradation of the catalyst which is enhanced by the concomitant presence of oxygen that promotes metal dissolution. A recurrent question is how the catalyst surface evolves under these circumstances. Moreover, electrochemical and surface science experiments,[5,13,29,30] and continuum[31] and kinetic Monte Carlo[32] (KMC) simulations suggest that a porous structure might be present after the dealloying process. Experimental studies by Dimitrov et al.[33] have concluded that dealloying of a less-noble component is sometimes accompanied by surface oxide formation involving the less-noble element, increasing the retention of such element in the porous matrix and modifying the catalytic activity. However, the structural models inferred from the experiments lack specific information and are only qualitative. On the other hand, a recent assessment of the catalytic activity of bimetallic and trimetallic alloys of composition PtM_3 and $PtNi_3M$ (with M = Co, Cu, Cr)[29] has clearly shown an enhanced ORR electrocatalytic activity claimed to be the highest activity currently achieved along with that given by the nanostructured thin film developed by 3M whose technical details have not been published. But the actual reasons of the activity benefit which are attributed to the "nanoscale structure" of the dealloyed particles are not yet explained. Here we study the driving forces and the effect of dealloying on the structure of alloy nanocatalysts during their synthesis and operation with a multi-scale approach involving KMC simulations and DFT calculations. The KMC method allows simulating the dynamic evolution of a catalyst in a long time scale, comparable to experiments. The required information for the method is the correct representation of all the relevant processes in the system in the form of rate expressions, the processes are selected based on the magnitude of their rate combined with a random approach. In typical KMC simulations, the atoms or species involved in the processes typically occupy sites in 2-D a lattice. However, a main contribution of this work is the development of a versatile 3-

D simulation code to study the degradation and dealloying processes in ORR catalysts. The scope of the proposed KMC model can be expanded to simulate the entire synthesis of porous or hollow catalysts, starting from the galvanic replacement, followed by the formation of their characteristic structure through dealloying, until the analysis of their performance during operation. Two relevant cases of study for the improvement of state-of-the-art ORR catalysts are reported. The degradation of Pt nanoparticles under different potential regimes is studied, in order to determine their effect on the durability of the nanoparticles, and the formation of Pt and Pt—Pd and hollow nanoparticles by the Kirkendall effect, to understand the role of the applied potential and of vacancies that yields to the hollow structure.

CHAPTER II
OXYGEN ADSORPTION AND SURFACE SEGREGATION IN (211) SURFACES OF Pt(SHELL)/M(CORE) AND Pt_3M (M=Co, Ir) ALLOYS*

II.1 Motivation

Near-surface alloys (NSAs) are defined as alloys wherein a solute metal is present near the surface of a host metal in concentrations different from the bulk (e.g. Pt monolayers on base metals). The understanding and development of NSAs is a promising area of research in catalyst design.[34-37] For example, recent studies show that NSAs of Pt enhance the catalytic properties of pure Pt for H_2 activation kinetics, whereas at the same time they bind adsorbates much weaker than pure Pt.[34-36] In addition, NSAs represent an alternative configuration where minimum amounts of Pt are required. The core-shell structure studied in this work can be visualized as a representation of a NSA. On the other hand, we chose $Pt_3M(211)$ (M = Cr, Ir) alloy systems because these compositions have been found among the most successful.[2]

Although most studies focus on the understanding of the interactions of adsorbates with perfect crystal surfaces, much of the physics and chemistry that takes place on real materials occurs at defects.[38] Therefore, investigating the role of defects may improve our knowledge of real systems. In our case of interest, Pt nanoparticles in the range of 2-5nm have about 40% (111) facets, a similar percent of edges and corners whereas the additional 20% are (100) surfaces.[39] High Miller index surfaces, like (211) surfaces, provide useful means to create a range of local atomic environments such as steps or terraces[38]. The studied (211) stepped surface can be classified as a surface with (111) terraces separated by monatomic (100) steps as shown in Figure II-1.

---

* Reprinted with permission from "Oxygen adsorption and surface segregation in (211) surfaces of Pt(shell)/M(core) and Pt_3M (M=Co,Ir)" by Callejas-Tovar, R.; Balbuena, P. B. *Surface Science*, Volume 602, 3531-3539, Copyright © 2008 by Elsevier Limited.

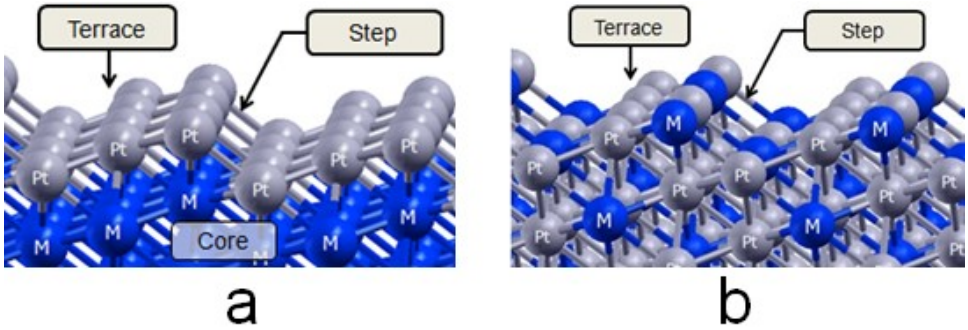

Figure II-1. The studied (211) surface formed by (111) terraces separated by monatomic (100) steps. (a) core-shell structure. (b) Pt_3M alloy system. Grey and blue spheres represent Pt and M atoms, respectively.

For alloys, it has been reported that catalytic activity depends dramatically on how the atoms arrange in the first 2-3 layers of the catalyst surface[40-43] and it is influenced by the surface segregation phenomenon. Therefore, it is important to characterize the surface atomic distribution of catalytic alloys and to elucidate the effect of segregation on surface structure. In this work, we investigate the surface segregation phenomenon carried out in stepped (211) surfaces and how it is affected by the adsorption of oxygen. Also, we discuss the effect of steps and terraces on the oxygen adsorption energy as well as their effect on surface segregation in comparison with that on (111) surfaces.

II.2 Computational details

We apply density-functional-theory (DFT) which has been successfully used to study the adsorption and reaction on catalytic surfaces.[36,38,40,44-53] The DFT calculations were performed using the Vienna Ab-initio Simulation Package (VASP).[54-58] In VASP the Kohn–Sham equations are solved by self-consistent algorithms. In order to improve the calculation efficiency, core electrons were replaced by the projector augmented wave (PAW) pseudo–potentials[59,60] and the valence electrons were described by plane wave basis sets. In this work, the plane wave was expanded up to a cutoff energy of 340 eV.

Brillouin zone integration was made on an 11 × 11 × 1 Monkhorst–Pack k-point mesh. The exchange-correlation functional was described within the generalized gradient approximation (GGA) proposed by Perdew, Burke and Ernzerhof (PBE).[61] Spin polarization was taken into account in the calculations and the Methfessel–Paxon

method was employed to determine electron occupancies with a smearing parameter σ of 0.2 eV. The convergence criteria for the electronic self-consistent iteration and the ionic relaxation loop were set to 10^{-4} eV and 10^{-3} eV, respectively.

The Pt_3M (M=Co, Ir) alloys possess close-packed FCC structures,[62-64] in which the Pt atoms occupy the face-centered positions and the M atoms are located at the corners in the unit cell, as shown in Figure II-2. The (211) stepped surface was created cleaving the FCC unit cell through the corresponding Miller plane.

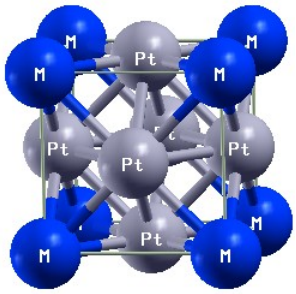

Figure II-2. Unit cell of close-packed FCC Pt_3M crystal. Pt atoms occupy face-centered positions and M atoms are located at the corners in the unit cell. The unit cell was cleaved through the (211) Miller plane in order to create the stepped surface. Grey and blue spheres represent Pt and M atoms, respectively.

Simulation supercells for the Pt_3M alloy system and core-shell structure are shown in Figure II-3, they consist of a 4-layer slab and a 6-layer vacuum space (~12 Å). In the core-shell super cell the first layer is formed by Pt atoms only, whereas the core (the other three layers) is constituted by either pure Co or Ir (denoted by M atoms in Figure II-3c). The core was built as pure Co or Ir in FCC arrangements, bulk calculations provided the lattice constants of 3.520 Å and 3.876 Å, respectively. These lattice constant values compare with the experimental values of 3.56 Å[65] for FCC Co and 3.84 Å for Ir.[66] Although Co is hcp in bulk, it has been reported that it adopts FCC structure in nanoparticles of diameters below 20 nm.[67] In both surface configurations, Pt_3M and core-shell structure, the atoms in the top three layers were allowed to relax to the lowest energy configuration, while the atoms of the bottom layer were fixed to their bulk positions.

The (211) surface has (111) terraces separated by monatomic (100) steps as shown in Figure II-3, where site 1 corresponds to a step site while sites 2 and 3 are terrace sites. The segregation structures in the core-shell structure were obtained exchanging Pt atoms of the first layer and core atoms of the second layer through any of sites 1 to 3, whereas for the Pt_3M system the segregation structures were the result of exchanging M atoms from the first layer and Pt atoms at the second layer through sites 1 or 3.[52] Segregation structures were studied with and without the presence of oxygen adsorbed.

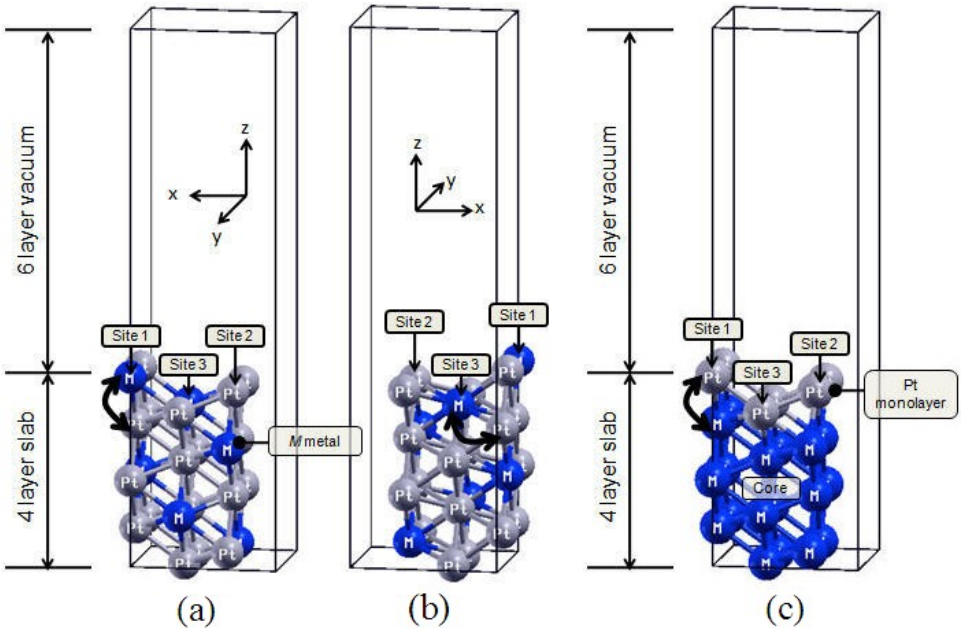

Figure II-3. Proposed slab model for DFT calculations of oxygen adsorption and surface segregation in Pt_3M and Pt(shell)/M(core) (211) stepped surfaces. The structures are composed of a 4-layer slab and a 6-layer vacuum. Site 1 corresponds to a monatomic (100) step site while sites 2 and 3 are terrace (111) sites. (a) and (b) are different views of the Pt_3M system, whereas (c) depicts the core-shell structure. Gray and blue spheres represent Pt and M atoms, respectively.

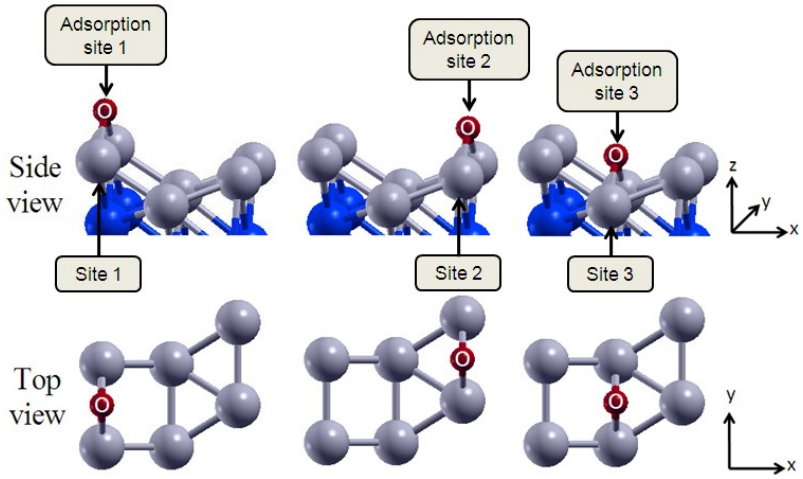

Figure II-4. Initial configuration used for the simulation of oxygen adsorption. We placed an oxygen atom in a bridge position involving any of the atoms of sites 1 to 3 and an adjacent atom in y-direction. O atom represented in red.

For the simulation of oxygen adsorption, as initial configuration we placed an oxygen atom in a bridge position involving any of the atoms of sites 1 to 3 and its adjacent atom in the y-direction as shown in Figure II-4. The oxygen atom was allowed to relax together with the atoms in the top three layers to its lowest energy configuration. We chose a bridge site as initial configuration based in our calculations of oxygen adsorption on pure Pt(211) discussed in the next section.

The surface segregation energy, E_{segr}, is generally defined as the energy of moving an atom from the interior to the surface of a crystal. In this work, it is characterized as the difference of total energies of the slab with the segregated structure and that with the non-segregated structure.[52] For the core-shell structures having pure Pt in their shell we test M segregation to the surface, thus a negative value of segregation energy indicates that the M atoms are able to segregate to the surface, while a positive segregation energy suggest no M segregation on the surface. In the case of the Pt_3M we test the segregation of Pt, negative values of surface segregation energy imply that Pt atoms segregate to surface, whereas positive segregation energies mean no Pt segregation to the surface. On the other hand, the adsorption energy, E_{ads}, was evaluated subtracting from the total energy of the slab with oxygen adsorbed the total energy of the slab without oxygen and the total energy of the oxygen atom. In the present study, we will denote with $(E_{segr}')_i$ the

segregation energy calculated in the presence of oxygen bonded to surface involving adsorption site *i*, as defined in Figure II-3.

II.3 Results and discussion

We begin this section discussing the results of oxygen adsorption on pure Pt(211) surfaces; such results provide information about the most stable sites for oxygen adsorption. Then, we analyze the adsorption of oxygen and its effect over surface segregation on $Pt_3M(211)$ and Pt/M (211) core-shell surfaces.

II.3.1 Oxygen adsorption on pure Pt(211)

First we identify the most stable adsorption sites on pure Pt (211) surfaces. The adsorption energies corresponding to different adsorption sites are shown in Figure II-5, sites (a) to (f) are different types of bridge sites, whereas (g) and (h) depict hollow sites. The most energetically favorable adsorption site with E_{ads} =-4.55 eV corresponds to the bridge site over and parallel to the (100) step, denoted with (a) in Figure II-5. We found that the adsorption sites located on the (111) terraces are less energetically stable than step sites. These results are in agreement with scanning tunneling microscopy experiments that indicate that oxygen atoms resulting from dissociation of the molecular precursor state locate on upper sites of Pt step edges.[68] In addition, our results agree with reports indicating that steps on Pt(111) bind oxygen molecules and atoms more strongly than terrace sites[68-71] and with the experimental observation of a minority of O atoms on the terraces in the dissociation of O_2 over Pt.[68] Based on these results we decided to use bridge sites as initial configurations for the study of oxygen adsorption in Pt_3M systems and core-shell structures. We have also tested the 4-fold binding site on the step of the Pt(211) surface, and found that is unstable. After relaxation, the oxygen atom adsorbs on the bridge site over the step.

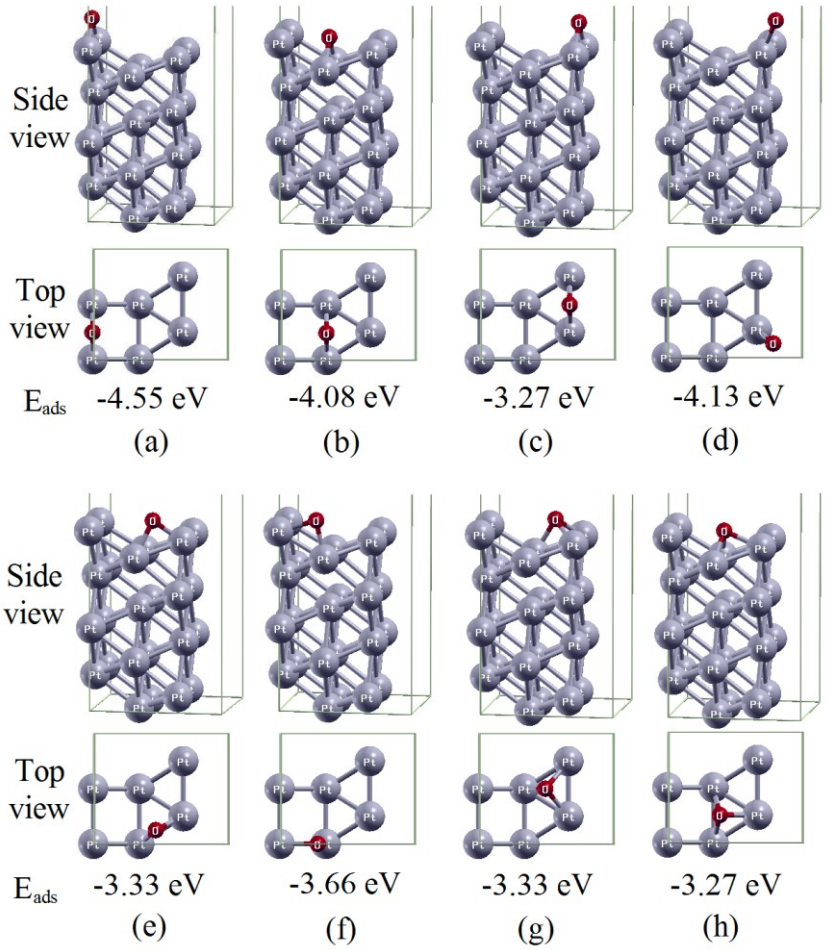

Figure II-5. Adsorption sites investigated for Pt(211) surfaces. Sites (a) to (f) are different types of bridge sites; (g) and (h) are hollow sites. Note that in (d) the O is adsorbed in a bridge site formed by one Pt atom (shown) and another from an image cell (not shown). In the top view, only the top layer is shown to improve the visualization, Pt atoms represented in gray and O atoms in red.

II.3.2 Adsorption on $Pt_3Co(211)$ and $Pt_3Ir(211)$

The most stable oxygen adsorption sites and their corresponding adsorption energies for $Pt_3Co(211)$ and $Pt_3Ir(211)$ surfaces are shown in Figure II-6. Our calculations show that O adsorption on a PtM bridge site over and parallel to the (100) step is more favorable energetically than that on the Pt—Pt terrace bridge site for both surfaces, having an energy difference of 1.03 eV and 1.40 eV between both sites for Pt_3Co and Pt_3Ir, respectively. The obtained adsorption energies in the step sites, -4.80 eV for Pt_3Co and -5.23 eV for Pt_3Ir, imply stronger oxygen binding than that in the

equivalent site of the Pt(211) surface in which the adsorption energy is -4.55 eV (Figure II-5a). Moreover, the oxygen adsorption in $Pt_3M(211)$ surfaces is stronger than in the Pt(111) surface, where the experimental adsorption energy reported is -4.32 eV[72] and DFT studies provide -3.86 eV for a bridge site and -4.48 eV for a FCC site.[73] The oxygen binding energy of the bridge site over the step in the $Pt_3Co(211)$ surface is 0.43 eV higher than the equivalent site in the (111) surface.[73] We found that the oxygen adsorption in the terrace site next to the (100) step, denoted as adsorption site 3 in Figure II-3, is not stable. We also tested the top sites on Pt_3Co, yielding the following results: O bound to Co, E_{ads} = -4.34 eV, O bound to Pt, E_{ads} = -3.74 eV. Thus, both cases show a weaker adsorption energy than the bridge site over the step (Eads = -4.80 eV). On Pt_3Ir: O bound to Ir, Eads = -4.77 eV, O bound to Pt, Eads = -3.45 eV. Again, both cases show a weaker adsorption energy than that on the bridge site over the step (Eads = -5.23 eV).

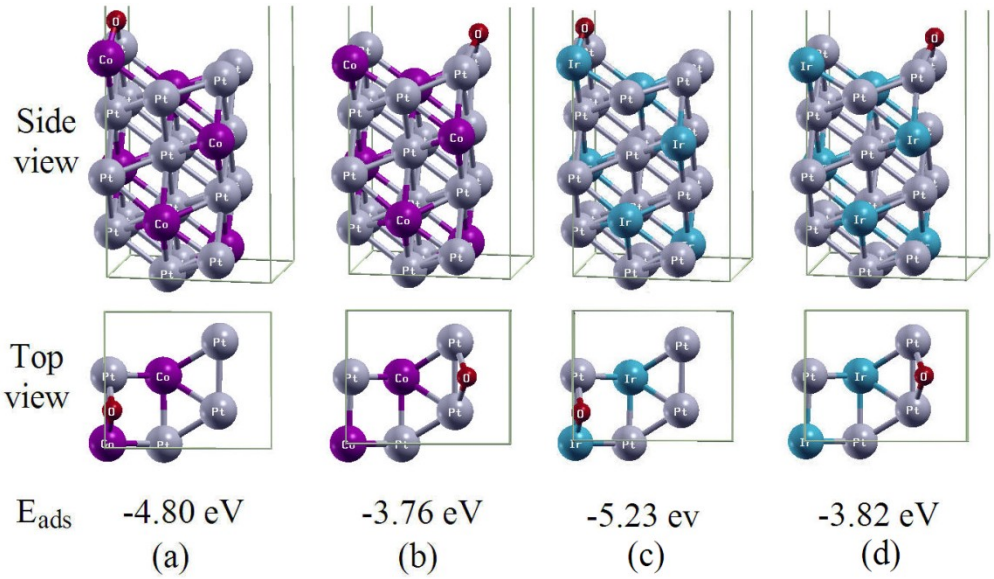

Figure II-6. Oxygen adsorption on $Pt_3Co(211)$ and $Pt_3Ir(211)$. Step sites (a) and (c), terrace sites (b) and (d). Pt, Co, Ir and O atoms represented as gray, purple, blue and red spheres, respectively.

II.3.3 Surface segregation in $Pt_3Co(211)$ and $Pt_3Ir(211)$

The results of our analysis of surface segregation in clean surfaces and in presence of oxygen adsorbed for $Pt_3Co(211)$ and $Pt_3Ir(211)$ surfaces are shown in Figure II-7 and

Figure II-8, respectively. For both systems in vacuum we find that there is Pt segregation to the surface, with a pure Pt top layer being the most stable configuration. The corresponding segregation energies are -0.87 eV for Pt_3Co and -1.20 eV for Pt_3Ir. These energies are higher than those reported by Ma and Balbuena[52] for $Pt_3Co(111)$ and $Pt_3Ir(111)$ surfaces, whose segregation energies are -0.61 eV and -0.54 eV, correspondingly. Experimental results from Menning et. al.[74] also suggested that (111) surfaces of Pt-Co-Pt structures are relatively stable, with outward segregation and inward diffusion of Co atoms coexisting.

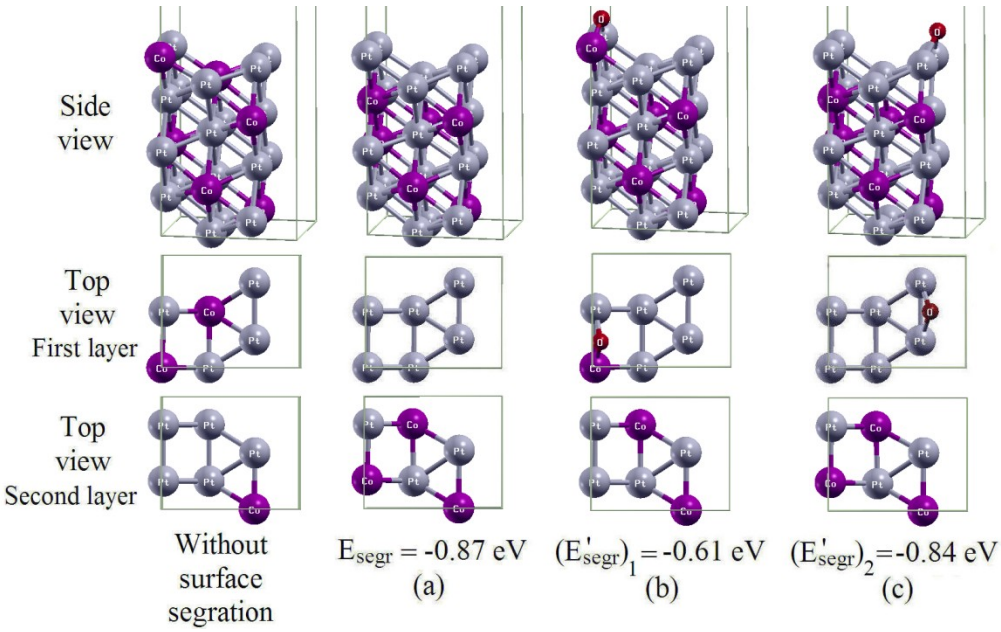

Figure II-7. Segregated structures in Pt_3Co (211) surface. Pt segregation: (a) in vacuum, (b) in presence of oxygen adsorbed on step site, and (c) on terrace site. Pt, Co and O atoms represented as gray, purple and red spheres, respectively.

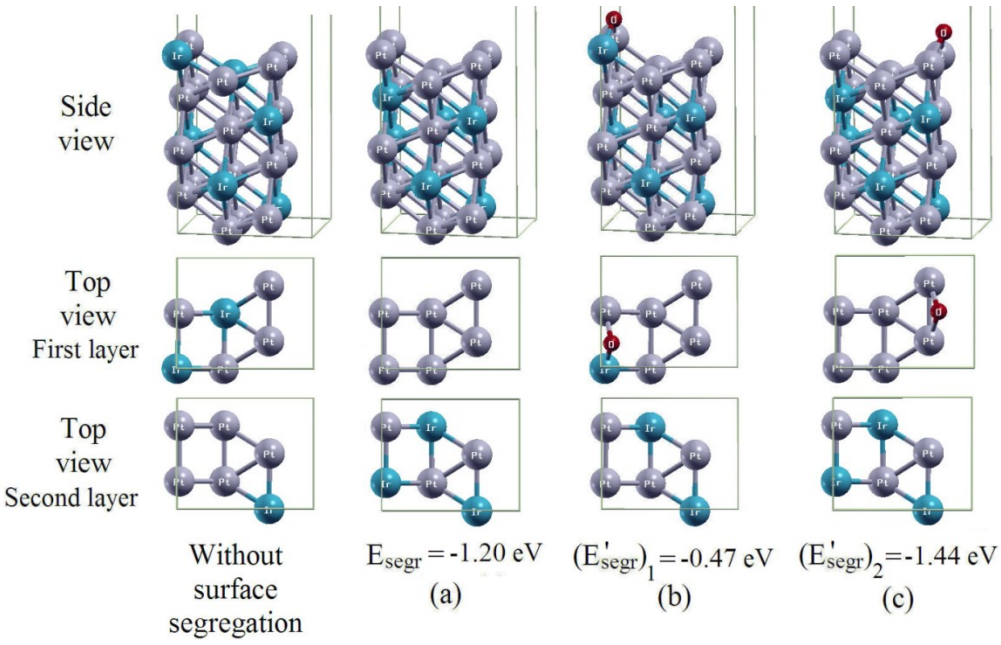

Figure II-8. Segregated structures in Pt_3Ir (211) surface. Pt segregation: (a) in vacuum, (b) in presence of oxygen adsorbed on step site, and (c) on terrace site. Pt, Ir and O atoms represented as gray, blue and red spheres, respectively.

When oxygen is present, the most stable configuration is again the adsorption on a bridge site over the step; in this case we observe for both alloys that Pt segregation takes place only through the terrace site and the Co or Ir atoms in the step remain in the surface. Our calculations provide surface segregation energies, $(E_{segr}')_1$, of -0.61 eV and -0.47 eV for Pt_3Co and Pt_3Ir, respectively. If oxygen adsorption takes place in a bridge site over a terrace (adsorption site 2 in Figure II-4), we find Pt segregation through step and terrace sites, which is the same behavior observed on the clean surfaces. The segregation energies obtained, $(E_{segr}')_2$, are -0.84 eV for Pt_3Co and -1.44 eV for Pt_3Ir. However such adsorption site has weaker adsorption energies for both alloys (Figure II-6). We observe for both systems that the oxygen adsorption over the step decreases the Pt segregation energy, being this effect more dramatic for the Pt_3Ir surface.

In Table II-1 and Table II-2 we present the effect of oxygen adsorption on the distance between the first and second layers (d_{12}) and the surface segregation energies for the various sites of the Pt_3Co and Pt_3Ir (211) surfaces. We observe that the oxygen adsorption in a bridge site over the step (site 1 in Figure II-4) increases the distance

between the first and second layers for the non-segregated and segregated structures of both systems (see $(d'_{12})_1$ column in Table II-1 and Table II-2 compared to d_{12} column). In contrast, the effect of the oxygen adsorption on the terrace site is to reduce the distance (see $(d'_{12})_2$ column) between those two layers. On the other hand, the oxygen adsorption over the step site increases the Pt segregation energy when it occurs through site 3 (referred to Figure II-3) in the Pt_3Co surface. For the Pt_3Ir system, the oxygen binding to the step site (site 1) decreases the Pt segregation energy for all the segregation structures, even making energetically unfavorable the Pt segregation through the step site. When the oxygen adsorption takes place on the terrace site (site 2), the Pt segregation energies of the Pt_3Co surface decrease slightly, whereas for the Pt_3Ir system the Pt surface segregation is enhanced.

Table II-1. Effect of oxygen adsorption on the distance between the first and second layers and surface segregation energy for the $Pt_3Co(211)$ surface

Segregation site	d_{12} (Å)	$(d'_{12})_1$ (Å)	$(d'_{12})_2$ (Å)	$\Delta(d_{12})_1$ (Å)	$\Delta(d_{12})_2$ (Å)	E_{segr} (eV)	$(E'_{segr})_1$ (eV)	$(E'_{segr})_2$ (eV)	$\Delta(E'_{segr})_1$ (eV)	$\Delta(E'_{segr})_2$ (eV)
Non-segregated	2.40	2.52	2.38	0.12	-0.02	-	-	-	-	-
Site 1	2.40	2.51	2.39	0.11	-0.01	-0.58	-0.08	-0.50	-0.51	-0.08
Site 3	2.38	2.49	2.37	0.11	-0.01	-0.38	-0.61	-0.39	0.23	0.00
Sites 1 and 3	2.41	2.48	2.34	0.07	-0.07	-0.87	-0.32	-0.84	-0.55	-0.03

d_{12} and $(d'_{12})_i$ denote the distance between the first and second layer in the clean surface and when oxygen is adsorbed in site *i* referred to Figure II-4, respectively.
$\Delta(d_{12})_i = (d'_{12})_i - d_{12}$
$\Delta(E'_{segr})_i=(E'_{segr})_i - E_{segr}$ is the difference of the segregation energies with oxygen adsorbed in site *i* and when the surface is clean.

Table II-2. Effect of oxygen adsorption on the distance between the first and second layers and surface segregation energy for the $Pt_3Ir(211)$ surface

Segregation site	d_{12} (Å)	$(d'_{12})_1$ (Å)	$(d'_{12})_2$ (Å)	$\Delta(d_{12})_1$ (Å)	$\Delta(d_{12})_2$ (Å)	E_{segr} (eV)	$(E'_{segr})_1$ (eV)	$(E'_{segr})_2$ (eV)	$\Delta(E'_{segr})_1$ (eV)	$\Delta(E'_{segr})_2$ (eV)
Non-segregated	2.50	2.52	2.46	0.02	-0.04	-	-	-	-	-
Site 1	2.49	2.51	2.45	0.03	-0.04	-0.75	+0.05	-0.93	-0.80	0.17
Site 3	2.48	2.49	2.44	0.02	-0.03	-0.48	-0.47	-0.51	-0.01	0.03
Sites 1 and 3	2.45	2.48	2.43	0.03	-0.02	-1.20	-0.41	-1.44	-0.79	0.23

d_{12} and $(d'_{12})_i$ denote the distance between the first and second layer in the clean surface and when oxygen is adsorbed in site *i* referred to Figure II-4, respectively.
$\Delta(d_{12})_i = (d'_{12})_i - d_{12}$
$\Delta(E'_{segr})_i=(E'_{segr})_i - E_{segr}$ is the difference of the segregation energies with oxygen adsorbed in site *i* and when the surface is clean.

II.3.4 Adsorption on Pt/Ir and Pt/Co (211) core-shell structures

The most stable adsorption sites and their corresponding adsorption energies for Pt/Co(211) and Pt/Ir(211) core-shell structures are shown in Figure II-9. For both systems the energetically most stable adsorption site is the bridge site over and parallel to the (100) step, with oxygen adsorption energies of -4.52 eV for Pt/Co and -4.33 eV for Pt/Ir. These binding energies are slightly higher than the adsorption energy of -4.32 eV[72] found in the Pt(111) surface, also following a similar trend to that reported by Menning et al.[75] If the oxygen adsorption takes place over a terrace (adsorption site 2 in Figure II-4), the binding energy in both systems is smaller than the one observed in the Pt(111) surface; however, the oxygen adsorption in the terrace is less energetically favorable than the adsorption over the steps.

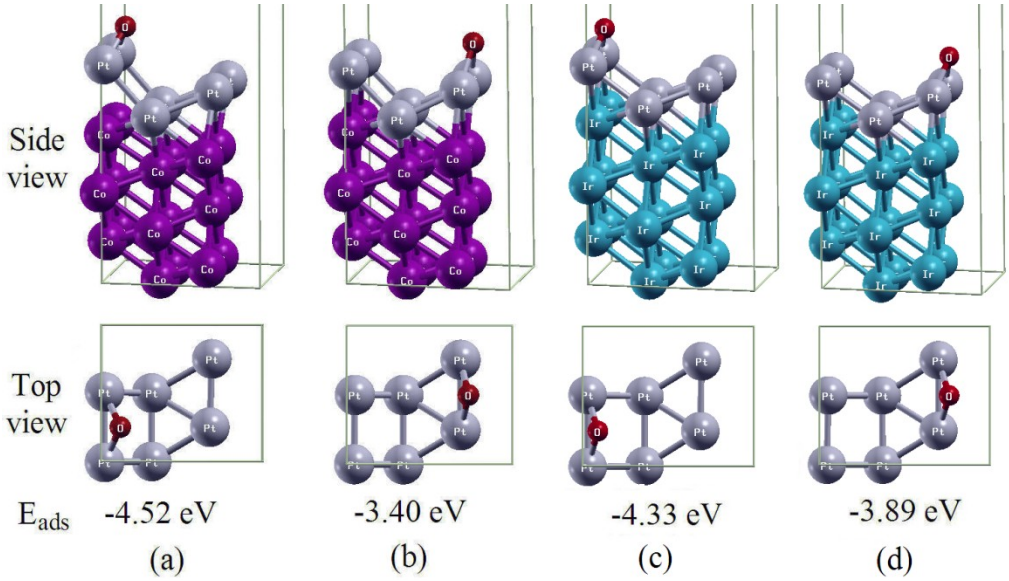

Figure II-9. Oxygen adsorption on Pt/Co(211) and Pt/Ir(211) core-shell structures. Step sites (a) and (c), terrace sites (b) and (d). Pt, Co, Ir and O atoms represented as gray, purple, blue and red spheres, respectively.

II.3.5 Surface segregation in Pt/Ir and Pt/Co (211) core-shell structures

In the core-shell structures we investigate segregation of the core elements (Co and Ir) to the surface. The most stable segregation structures in vacuum and with oxygen adsorbed in Pt/Co(211) core-shell configuration are shown in Figure II-10. We observe Co segregation through a terrace (site 3 in Figure II-3c) in the clean surface and when oxygen adsorption occurs in a terrace site. However, the most energetically favorable segregation structure in presence of oxygen involves the adsorption over the step site; in this case the Co segregation occurs through the step with segregation energy of -0.27 eV. The Co segregation behavior agrees with DFT calculations on (111) and (100) surfaces.[75] In contrast, for the Pt/Ir(211) surface our calculations show that there is no Ir segregation to the top layer neither in vacuum nor with oxygen adsorbed in any of the two stable adsorption sites. The structures with the highest antisegregation energies are shown in Figure II-11. The Ir antisegregation behavior observed in the Pt/Ir(211) is comparable to the Ir antisegregation observed in the (111) surface;[76] however, for the (211) surface even in the presence of oxygen adsorbed, the Ir segregation is still not favorable.

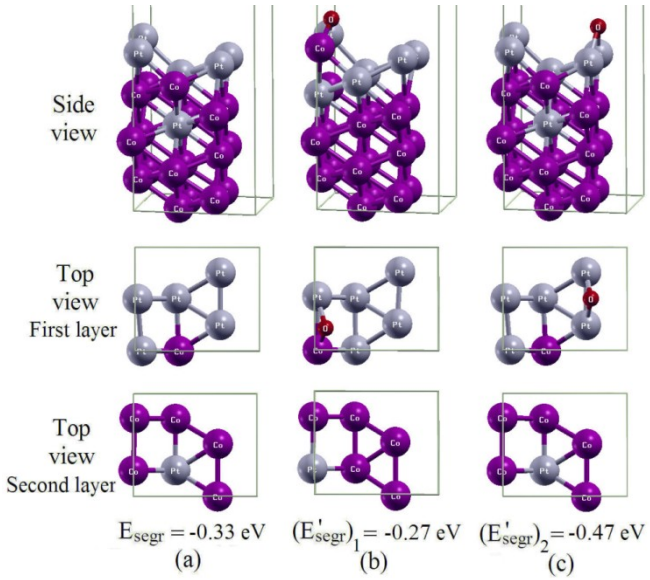

Figure II-10. Segregated structures in Pt/Co core-shell structure (211) surface. Co segregation in vacuum (a) and in presence of oxygen adsorbed on step site (b) and on terrace site (c).

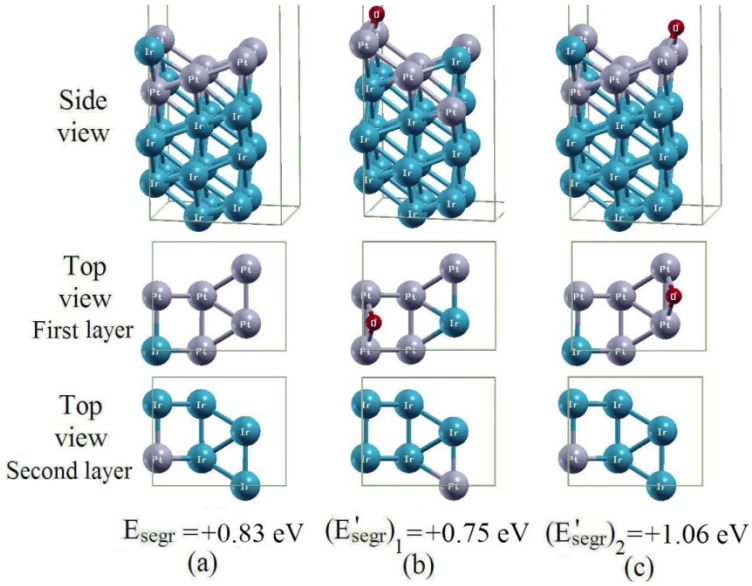

Figure II-11. Structures with the highest antisegregation energies in Pt/Ir core-shell structure (211) surface. Ir antisegregation in vacuum (a) and in presence of oxygen adsorbed on step site (b) and on terrace site (c).

Table II-3 and Table II-4 show the effect of oxygen adsorption on the distance between the first and second layer and surface segregation energies for the Pt/Co and Pt/Ir (211) core-shell surfaces, respectively. The effect of the oxygen adsorption in a bridge site over the step (site 1) is to increase slightly the distance between the first and

second layer for the segregated structures of both alloys. When the oxygen adsorption occurs on a terrace site, its effect on the distance between the first and second layers is not uniform for all the segregation structures.

Table II-3. Effect of oxygen adsorption on the distance between the first and second layer and surface segregation energy for the Pt(shell)/Co(core) structure

Segregation site	d_{12} (Å)	$(d'_{12})_1$ (Å)	$(d'_{12})_2$ (Å)	$\Delta(d_{12})_1$ (Å)	$\Delta(d_{12})_2$ (Å)	E_{segr} (eV)	$(E'_{segr})_1$ (eV)	$(E'_{segr})_2$ (eV)	$\Delta(E'_{segr})_1$ (eV)	$\Delta(E'_{segr})_2$ (eV)
Non-segregated	2.43	2.51	2.38	0.08	-0.05	-	-	-	-	-
Site 1	2.50	2.51	2.52	0.01	0.02	+0.28	-0.27	+0.11	0.54	0.16
Site 2	2.42	2.46	2.38	0.05	-0.03	-0.19	-0.07	-0.38	-0.12	0.19
Site 3	2.31	2.34	2.29	0.03	-0.02	-0.33	-0.16	-0.47	-0.17	0.14

d_{12} and $(d'_{12})_i$ denote the distance between the first and second layer in the clean surface and when oxygen is adsorbed in site *i* referred to Figure II-4, respectively.
$\Delta(d_{12})_i = (d'_{12})_i - d_{12}$
$\Delta(E'_{segr})_i=(E'_{segr})_i - E_{segr}$ is the difference of the segregation energies with oxygen adsorbed in site *i* and when the surface is clean.

Table II-4. Effect of oxygen on the distance between the first and second layer and surface segregation energy for the Pt(shell)/Ir(core) structure

Segregation site	d_{12} (Å)	$(d'_{12})_1$ (Å)	$(d'_{12})_2$ (Å)	$\Delta(d_{12})_1$ (Å)	$\Delta(d_{12})_2$ (Å)	E_{segr} (eV)	$(E'_{segr})_1$ (eV)	$(E'_{segr})_2$ (eV)	$\Delta(E'_{segr})_1$ (eV)	$\Delta(E'_{segr})_2$ (eV)
Non-segregated	2.45	2.48	2.42	0.03	-0.03	-	-	-	-	-
Site 1	2.47	2.48	2.45	0.01	-0.03	+0.83	+0.03	+1.06	0.80	-0.23
Site 2	2.44	2.46	2.45	0.02	0.01	+0.59	+0.75	+0.14	-0.16	0.45
Site 3	2.40	2.42	2.38	0.02	-0.01	+0.51	+0.50	+0.43	0.01	0.08

d_{12} and $(d'_{12})_i$ denote the distance between the first and second layer in the clean surface and when oxygen is adsorbed in site *i* referred to Figure II-4, respectively.
$\Delta(d_{12})_i = (d'_{12})_i - d_{12}$
$\Delta(E'_{segr})_i=(E'_{segr})_i - E_{segr}$ is the difference of the segregation energies with oxygen adsorbed in site *i* and when the surface is clean.

On the other hand, the surface segregation is enhanced when oxygen binds to the step and it takes place through the step site for Pt/Co and Pt/Ir systems. However, this increment in the segregation energy is not high enough to make the Ir segregation

energetically favorable in the Pt/Ir surface. The oxygen adsorption on the terrace site increases the segregation energy for almost all segregation structures. Nevertheless, the Ir segregation remains unfavorable even in presence of oxygen adsorbed.

II.4 Summary of results

In Table II-5 we summarize the calculated adsorption and segregation energies for the studied systems. As we mentioned before, the most stable configurations in all cases involve the oxygen adsorption over the (100) step, corresponding to a stronger oxygen binding compared with the less energetically favorable terrace adsorption site. We observe that higher adsorption energies are related to smaller segregation energies. The Pt/Ir(core) system is the only one that exhibits antisegregation behavior even under the presence of oxygen, this implies that the Pt monolayer may remain at the top of the surface. Moreover, the calculated adsorption energy for the Pt/Ir(core) (211) surface is only 0.1 eV higher than such reported for the Pt(111) surface.[72] Therefore, the Pt/Ir(core) system is a good candidate for further research.

Table II-5. Adsorption and segregation energies in presence of oxygen adsorbed in (211) surfaces. In parenthesis are the metals that are tested for segregation in each case.

	E_{ads} at step, (eV)	$(E_{segr}')_1$ (eV)	E_{ads} at terrace (eV)	$(E_{segr}')_2$ (eV)
Pt_3Co	-4.80	-0.61 (Pt)	-3.76	-0.84 (Pt)
Pt_3Ir	-5.23	-0.47 (Pt)	-3.82	-1.44 (Pt)
Pt/Co(core)	-4.52	-0.27 (Co)	-3.40	-0.47 (Co)
Pt/Ir(core)	-4.33	+0.75 (Ir)	-3.89	+1.06 (Ir)

As a final comment, is worth to mention that segregation at the step might occur when oxygen is adsorbed. Even if step edge segregation is not as exothermic as segregation through the terrace when oxygen remains adsorbed at the step edge, it is possible that desorption of oxygen from the step edge might make step edge segregation more exothermic than terrace segregation.

CHAPTER III
MOLECULAR DYNAMICS SIMULATIONS OF SURFACE OXIDATION OF Pt(111) AND Pt/PtCo/Pt_3Co(111)*

III.1 Motivation

The electrocatalysis of the ORR is carried out on nanoparticles with the goal of employing the smallest amount of material that is able of maximizing the catalytic activity and stability. Pt-based alloy catalysts reduce the required amount of platinum and some of them have shown enhanced ORR activity compared to pure Pt catalysts, specifically the Pt_3Co alloy has demonstrated remarkable activity,[2-4] partially attributed to the formation of a "Pt-skin" structure produced by an exchange of Pt and Co in the first two layers,[3] denoted in this work as Pt/PtCo/Pt_3Co. Despite of its enhanced activity, the Pt_3Co catalysts exhibit Co dissolution during the fuel cell operation, decreasing their activity.[13] The dissolution process may involve interactions between the topmost layers of the catalyst, atomic oxygen, oxygenated species, and the electrolyte. The existence of a correlation between the onset of the oxide formation and the concentration of dissolved Pt has been found experimentally.[15] Moreover, several experimental papers have investigated the effects of acid-treated, annealed, or electrochemically dealloyed nanocatalyst particles and have suggested the evolution of the catalyst towards a nanoporous matrix with a Pt-rich surface.[5,6,8,33,77] However, in spite of the new insights provided by illuminating STM-based experiments[13,17,78] the actual mechanism of the dissolution process and particularly its effects on the catalyst structure are not well understood. In this study we apply molecular dynamics to identify molecular level changes on the structure caused by oxidation of Pt(111) and Pt/PtCo/Pt_3Co(111) catalysts. We use classical molecular dynamics (MD) simulations modeling the surface as a slab that is exposed to increasing amounts of atomic oxygen and water. Our MD

---

model considers electrostatic interactions between the adsorbates, atomic oxygen and water, and the two topmost layers of the catalyst, where the atoms in the 1st and 2nd surface layers are charged with average values obtained from DFT calculations. Our simulations include a wide range of oxidative conditions corresponding to approximately from 0.6 to 1.3 V with respect to SHE, to emulate not only normal operative conditions but also transient conditions that could occur during startup or shut down.[79]

III.2 Computational details

The MD simulations were performed using DL_POLY 2.20[80-82] in the NVT ensemble with Evans thermostat at the fuel cell operation temperature of 353.15 K. The system consists of ten slabs in the arrangement of the (111) face of a FCC crystal. The 10 × 10 atom-surface is composed by either pure platinum or Pt/PtCo/Pt_3Co, as is shown in Figure III-1. The latter configuration is the result of segregation of Pt atoms from the subsurface to the topmost layer in a Pt_3Co alloy.[52,83,84]

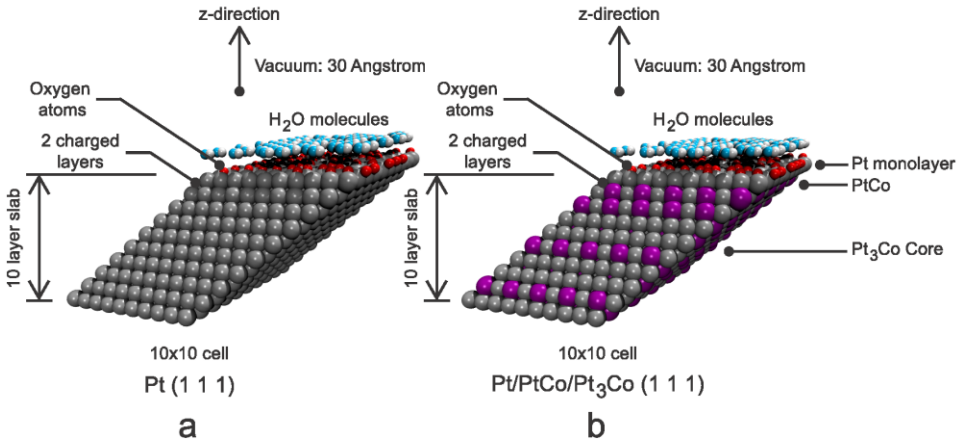

Figure III-1 Initial configurations used to represent the surfaces exposed to oxygen and water.

Oxygen atoms are placed on the topmost layer of the surface (initially at a distance of about 6.0 Å) together with an equal number of water molecules which are located above them. Parallelepiped periodic boundary conditions were used with a vacuum of 30 Å in the z-direction perpendicular to the surface. The total simulated time was 600 ps in all cases except those involving water and oxygen on the Pt/PtCo/Pt_3Co

surface, for which the total simulated time was 1200 ps; in all cases the time step was 1×10^{-3} ps.

The short-range interactions were represented through the Lennard-Jones (LJ) potential using the parameters reported in Table III-1 and the Lorentz-Berthelot mixing rules. The LJ parameters for the Pt—Pt and Co—Co interactions were obtained by fitting to the Sutton-Chen[85,86] potential energy surface for pure species.[87] For Pt—Pt the LJ parameters were taken from the literature,[88] a new parameterization was done for the Co—Co interactions,[89] whereas the LJ parameters for the O—O interactions were taken from the SPC/E model.[90]

Table III-1. Interaction energy (ε) and length (σ) parameters for the Lennard-Jones potential

Interaction	ε (eV)	σ (Å)
Pt-Pt	0.2013	2.410
Co-Co	0.1513	2.180
O-O	0.0067	3.165

Long-range Coulombic interactions were considered among the oxygen atoms, water molecules, and the metal atoms of the two topmost layers of the slab. Such interactions were calculated using the Ewald sum method[91,92] with a relative error of $1x10^{-3}$, the accuracy of the method was verified comparing the coulombic energy and the coulombic virial. The water molecules were modeled using the SPC/E model[90] with charges of -0.8476 e and +0.4238 e for their constituent oxygen and hydrogen atoms, respectively.

Because we want to represent the oxidation state of the surface and first subsurface layer, we assigned a negative charge to the oxygen atoms and a positive charge to the atoms forming the two topmost layers of the surface; the different sets of charges introduced in this paper are listed in Table III-2. The magnitude of such charges was set accordingly to the average surface or subsurface values obtained with the Bader charge analysis[93-96] from density functional theory (DFT) calculations performed using Vienna Ab-initio Simulation Package (VASP).[54-58,60,97] In the Bader charge analysis, the

electronic charge density that is contained in the Bader volume of an atom is a good approximation of the total electronic charge of such atom. In such calculations the core electrons were replaced by the projector augmented wave (PAW) pseudo—potentials, [59,60] the exchange-correlation functional was described within the generalized gradient approximation (GGA) proposed by Perdew, Burke, and Ernzerhof (PBE);[61] and spin polarization was taken into account.

Table III-2. Charges of the species for different coverages of oxygen (e)

Pt(111)				
Element	0.50 ML O	0.60 ML O	0.75 ML O	0.85 ML O
O	-0.50	-0.60	-0.60	-0.70
Pt in topmost layer	+0.20	+0.30	+0.40	0.50
Pt in second layer	+0.05	+0.06	+0.05	+0.10
$Pt/PtCo/Pt_3Co(111)$				
Element	0.50 ML O	0.60 ML O	0.75 ML O	0.85 ML O
O	-0.50	-0.60	-0.60	-0.70
Pt in topmost layer	+0.05	+0.135	+0.15	+0.195
Pt in second layer	0.00	0.00	0.00	0.00
Co in second layer	+0.40	+0.45	+0.60	+0.80

The figures and plots presented in this paper were prepared using VMD,[98] gnuplot,[99] and sK1.[100]

III.3 Results and discussion

We begin our discussion with the analysis of the Pt(111) and $Pt/PtCo/Pt_3Co(111)$ surfaces under vacuum. Then, we address the changes in the structure of the studied surfaces due to adsorption of different coverages of oxygen in the presence of water molecules. Finally we briefly discuss simulations of the reduction process.

III.3.1 Pt(111) and $Pt/PtCo/Pt_3Co(111)$ under vacuum

Figure III-2 depicts the structure of the pure platinum (111) slab under vacuum. The z-density profile and radial distribution function, Figure III-2a and Figure III-2b, provide information about interlayer separation and nearest-neighbor distances. These

values are in agreement with experimental information thus confirming that the Pt slab preserves its crystalline structure during the entire simulation period. Moreover, the topography and top view of the topmost layer, Figure III-2c and Figure III-2d, demonstrates its flat configuration.

The z-density profiles of the Pt/PtCo/Pt_3Co(111) and Pt_3Co(111) configurations under vacuum are shown in Figure III-3a and Figure III-3b, in both systems the Pt:Co ratio is 3:1. We observe that both slabs conserve their crystalline structure and their layers preserve their composition during all the simulation period. The Pt/PtCo/Pt_3Co slab is thermodynamically 0.023 eV/atom more favorable than the Pt_3Co slab. This difference was calculated by subtraction of the energies of the Pt_3Co and Pt/PtCo/Pt_3Co systems, and divided by the total number of atoms in the slab. This result is consistent with our DFT calculations in which the energy of the Pt/PtCo/Pt_3Co configuration is 0.03 eV/atom lower than such of the Pt_3Co configuration. Therefore, our further discussion considers only the Pt/PtCo/Pt_3Co(111) configuration, whose topography and top view of its topmost layer, Figure III-3c and Figure III-3d, show mainly a flat arrangement although small regions of steps and kinks are observed due to the lattice mismatch and vibrations of the Pt and Co atoms.

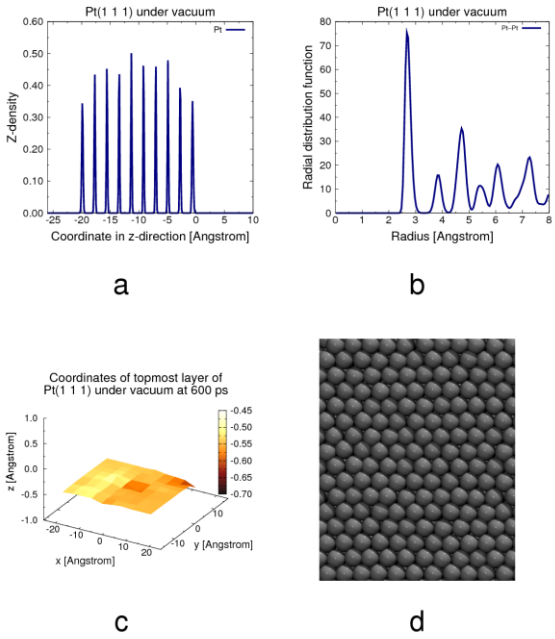

Figure III-2. Structure of Pt(111) under vacuum. Z-density profile (a), radial distribution function (b), topography of the topmost layer (c), and top view of the topmost layer (d).

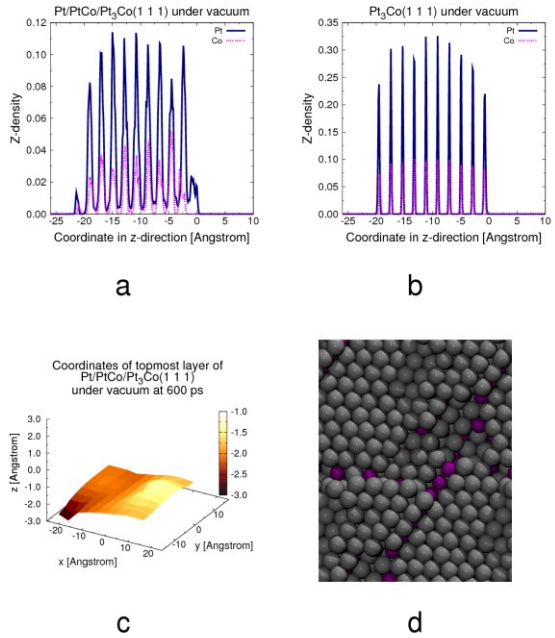

Figure III-3. Structure of Pt/PtCo/Pt_3Co(111) and Pt_3Co (111) under vacuum. Z-density profiles of Pt/PtCo/Pt_3Co (a) and Pt_3Co (b), energy profiles (c), topography (d) and top view of the topmost layer of Pt/PtCo/Pt_3Co.

III.3.2 Pt(111) covered by oxygen and water

Figure III-4 shows the z-density profiles of the species on Pt(111) under different oxygen coverages in presence of water molecules. At the lowest oxygen coverage and charge, 0.5 ML and -0.5 e, we observe in Figure III-4a that the structure of the topmost surface layers remains well-organized and all the oxygen atoms stay adsorbed on the preferred sites (Figure III-5a). As the oxygen coverage and its charge increase to values of 0.6 to 0.85 ML and -0.6 to -0.7 e (Figure III-4b to Figure III-4d) oxygen atoms migrate to the subsurface of the slab and buckling of the topmost Pt atoms is observed. Pt buckling results are in agreement with those obtained from DFT calculations shown in Table III-3. Buckling of Pt atoms in the topmost layer is evident at coverages of oxygen greater than 0.5 ML, and it is proportional to the electrostatic charge of the Pt atom. When the oxygen coverage increases to 0.85 ML with a corresponding oxygen charge of -0.7 e (Figure III-4d) practically all the oxygen atoms are absorbed in the subsurface, this is consistent with DFT calculations[20] which show that the increasing surface coverage of atomic oxygen can stabilize subsurface atomic oxygen. The simulations were all tested for convergence of the total energy.

Table III-3. Maximum buckling and maximum charge of surface atoms on Pt(111) under different oxygen coverages obtained from DFT calculations

Oxygen Coverage (ML)	Pt maximum buckling (Å)	Pt maximum charge (e)
0.5625	1.35	0.76
0.7500	1.92	1.13
0.8125	2.11	1.16

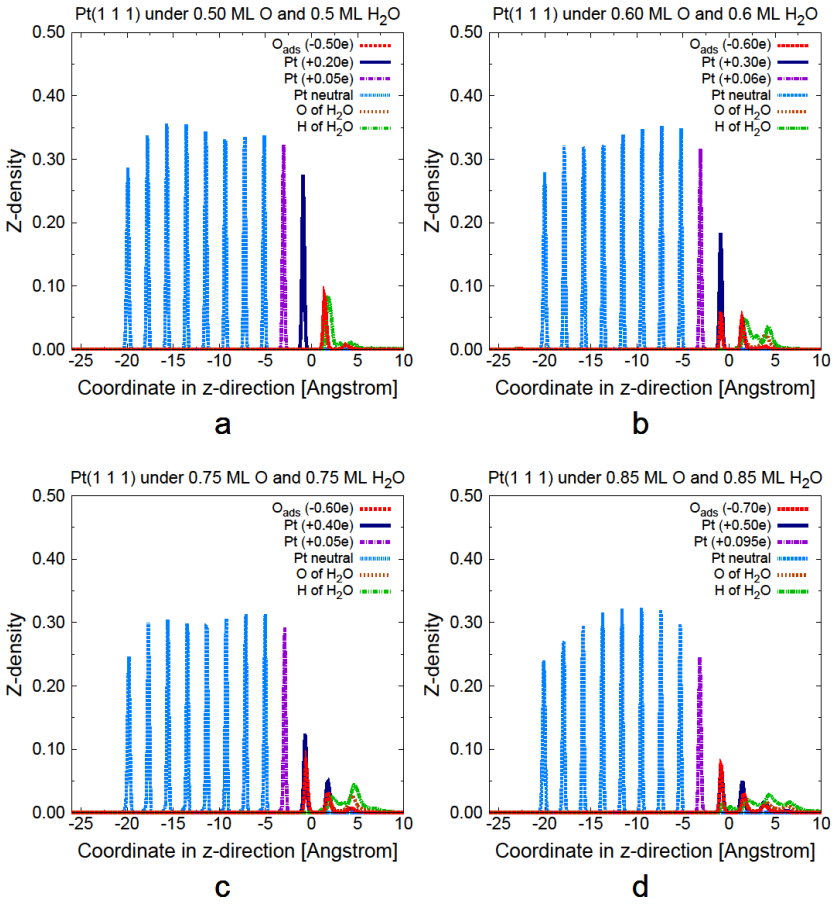

Figure III-4. Z-density profiles of Pt(111) under increasing coverages of oxygen atoms and water molecules.

These observations are also supported by the top view of a snapshot of the surface taken at the end of the simulation length as depicted in Figure III-5. The surface under 0.5 ML of oxygen with charge of -0.5 e (Figure III-5a) conserves essentially its flat arrangement with the oxygen atoms adsorbed evenly over the surface, most of them in the hollow sites. In contrast, the topmost layer of the surface under 0.85 ML of oxygen, with a charge of -0.7 e, (Figure III-5d) shows a dramatic change in its shape and a great extent of the oxygen atoms is absorbed in the subsurface.

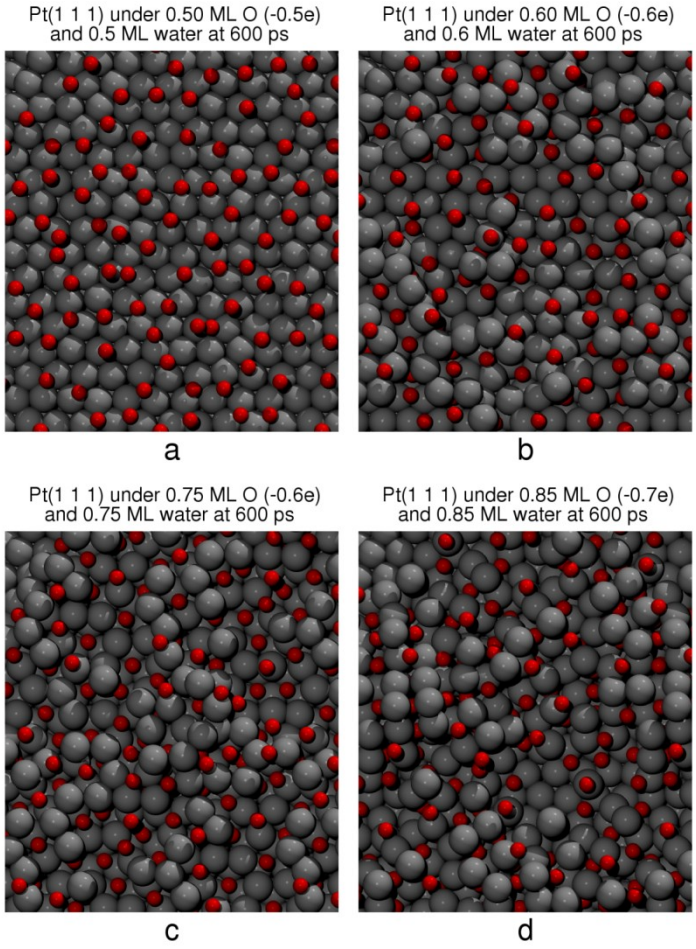

Figure III-5. Snapshots of top view of the surface of Pt(111) under different coverages of oxygen and water taken at the end of the simulation time. Oxygen and platinum atoms are represented as red and gray spheres, respectively. Periodic images are shown to improve the visualization and the water molecules are not shown.

Buckling of some atoms at the topmost layer of the surface with respect to vacuum conditions caused by the interactions with oxygen may be observed in Figure III-6. The changes in the topography of the topmost layer are more evident as the coverage of oxygen increases, starting with a buckling of 1.2 Å for 0.6 ML of oxygen (Figure III-6b) and increasing up to 3.0 Å for 0.85 ML of oxygen (Figure III-6d), this behavior is in agreement with the DFT results shown in Table III-3. Moreover, we found for oxygen coverages greater than 0.6 ML, the topmost layer of the surface loses its crystalline structure; it only conserves its nearest-neighbor distance. However, the structure of the subsurface Pt atoms remains virtually unaffected, in agreement with X-

ray spectroscopy studies.[78,101] We believe that the absorption of oxygen in the interstitial sites between the topmost and second layers is responsible of most of the buckling of the Pt atoms on the topmost layer. These observations agree with in situ EXAFS studies [102] of a Pt/C catalyst which reveal that the existence of the Pt—O bond weakens and/or changes the Pt—Pt bond of atoms near the surface. Also, our results are supported by reports of the lifting of Pt atoms of the surface layer from in situ X-ray reflectivity studies of the oxidation of Pt(111),[103] and by the observation of the height increase of cubic Pt nanoparticles due to the formation oxide species in their inner layer using atomic force microscopy (AFM).[104]

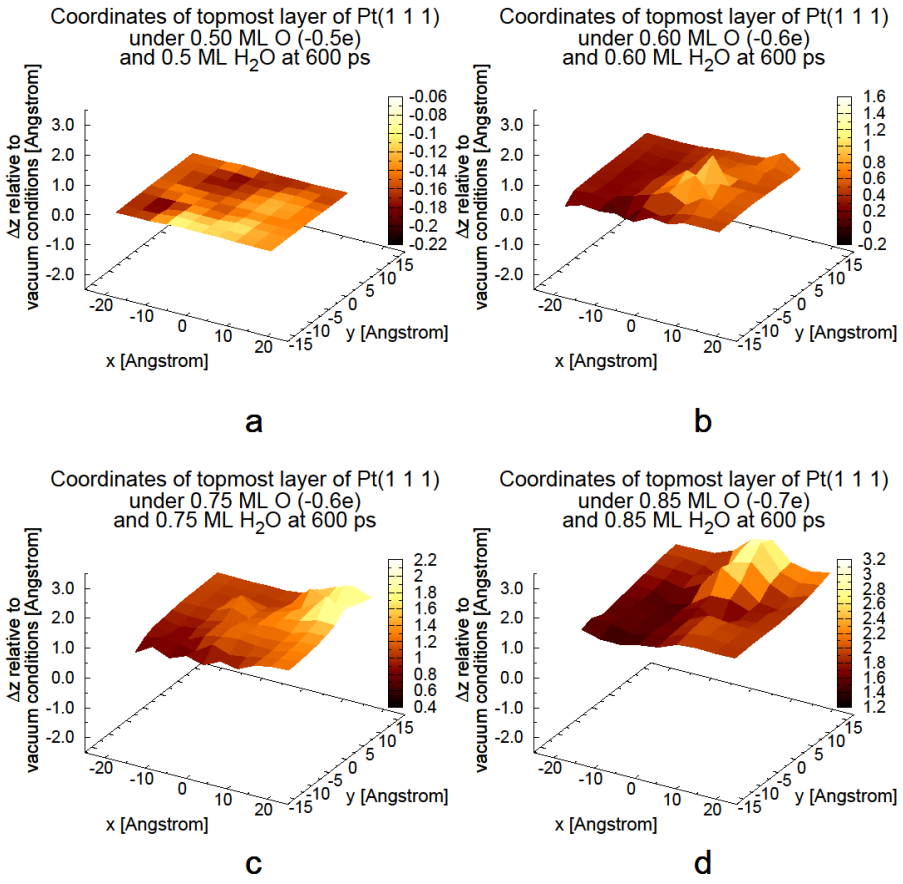

Figure III-6. Topographies of the topmost layer of Pt(111) under different coverages of oxygen atoms and water molecules. Buckling of the atoms in the topmost layer increases with the charge of the oxygen atoms.

For oxygen coverage of 0.5 ML, the adsorbed atoms form a flat layer at a distance of approximately 3.0 Å over the surface. As the oxygen coverage and its charge increases, such distance decreases and the topmost layer is distorted by buckling of some Pt atoms. For the highest oxygen coverage studied, 0.85 ML and -0.70 e it was found a layer of absorbed oxygen atoms in the subsurface whose shape matches that of the topmost layer. In addition, under these conditions the Pt—Pt bond of topmost atoms expanded from 2.80 to 2.95 Å and the arrangement of the absorbed oxygen atoms is ordered, showing nearest-neighbors distances of 3.35 , 4.75 , and 7.65 Å for the first, second, and third nearest-neighbors, respectively. These findings are evidence of a structured oxide lattice at high oxygen coverages in which a place exchange between oxygen and platinum atoms have occurred due to strong electrostatic interactions among them. The formation of the surface oxide reproduces features observed in experimental measurements on polycrystalline Pt electrodes using cyclic-voltammetry, electrochemical quartz-crystal nanobalance, and Auger electron spectroscopy,[105] and by in situ and real-time monitoring of oxide growth on Pt nanoparticles with X-ray spectroscopy,[78]

In all the cases in this study most of the water molecules form a flat layer over the surface at a distance of approximately 4.0 Å. Hydrogen bonding interactions between the hydrogen in water molecules and the oxygen atoms on the surface are stronger as the charge of the latter increases, the mean distance between such species is approximately 1.6 Å. However, in all cases we do not observe a hydrated oxide on the surface, in agreement with the experimentally determined molecular weight of the Pt surface oxide of 15.8 g mol^{-1}.[105]

It is worth mentioning that a dislocation in the Pt(111) surface may be formed depending on the initial configuration of the oxygen atoms in the simulation when the slab is exposed to coverages of 0.75 ML of oxygen or higher. A dislocation is formed if the initial distance between the layer of oxygen atoms and the topmost layer of the surface is less than 2.1 Å. Interestingly, the energy of the complete system with the dislocation is lower than such of the system without it, as is shown in Table III-4.

However, we decided to focus our previous discussion only on the surfaces without the dislocation, since such dislocation is artificially produced due to the initial configuration of the system. Moreover, we found the non-dislocated systems to be stable during the complete simulation length.

Table III-4. Average energy of the Pt(111) surface with and without dislocation.

Coverage of oxygen and water (ML)	Energy of the system with dislocation (eV/atom)	Energy of the system without dislocation (eV/atom)
0.75	-1.211	-1.173
0.85	-1.210	-1.205

III.3.3 Pt/PtCo/Pt_3Co(111) surfaces covered with oxygen and water

Figure III-7 shows the z-density profiles of the species on Pt/PtCo/Pt_3Co(111) under different coverages of oxygen in the presence of water molecules. It is evident that in all the studied cases oxygen is deeply absorbed into the surface, reaching the third layer. Moreover, we observe migration to such layer of the platinum atoms originally located in the subsurface. This dynamic behavior of the surface is caused by the high mobility of the cobalt atoms initially in the subsurface driven by the presence of the oxygen atoms. The cobalt atoms tend to segregate to the topmost layer due to their affinity with oxygen, leaving vacancies in the subsurface that are occupied by platinum atoms and by absorbed oxygen atoms once the topmost layer has been distorted, average compositions of the buckled and first three layers of the slab are shown in Table III-5.

Table III-5. Composition of the first three and bucked layers of Pt/PtCo/Pt_3Co(111) under different coverages of oxygen and water.

	Buckled layer			First layer			Second layer			Third layer		
O, H_2O coverage (ML)	Pt	Co	O	Pt	Co	O	Pt	Co	O	Pt	Co	O
0.60	0.35	0.35	0.30	0.67	0.11	0.22	0.43	0.43	0.14	0.75	0.25	0.00
0.75	0.10	0.45	0.45	0.73	0.10	0.17	0.84	0.06	0.10	0.75	0.16	0.09
0.85	0.17	0.33	0.50	0.42	0.22	0.36	0.90	0.02	0.08	0.78	0.18	0.04

The z-density profiles of neutral Pt and Co shown in Figure III-7a, corresponding to 0.5 ML oxygen, illustrate the formation of a dislocation caused by the surface segregation of charged cobalt atoms. Unlike the dislocation in the Pt(111) surface discussed previously, the formation of the dislocation in the Pt/PtCo/Pt_3Co(111) surface under 0.5 ML oxygen is independent of the initial configuration of the system. The formation of such dislocation is presented in Figure III-8. It starts in the early stages of the simulation at approximately 2.5 ps (Figure III-8b) when the first cobalt atom segregates to the surface, several oxygen atoms are adsorbed along the dislocation line enhancing the migration of the cobalt atoms to the topmost layer through the dislocation. After 20 ps (Figure III-8e) the dislocation is completely formed and it remains during all the simulation length.

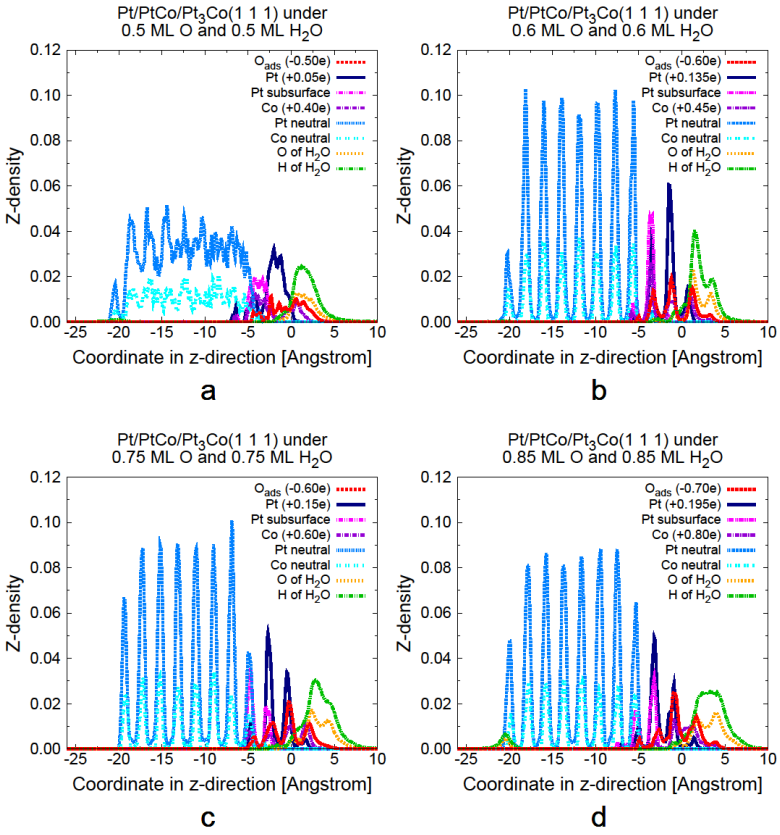

Figure III-7. Z-density profiles of Pt/PtCo/Pt_3Co(111) under different coverages of oxygen atoms and water molecules.

The described dislocation has characteristics of edge and screw dislocations; therefore it might be classified as a mixed dislocation. Since the local composition of the crystal changes as a result of the surface segregation of Co atoms, it is hard to define the Burgers vector at a given simulation time. However, we recognize that portions of slab shift in opposite directions of the z-axis. This is an interesting example of the irreversible changes in the structure of the alloy surface that may occur due to the adsorption of oxygen even at moderate coverages.

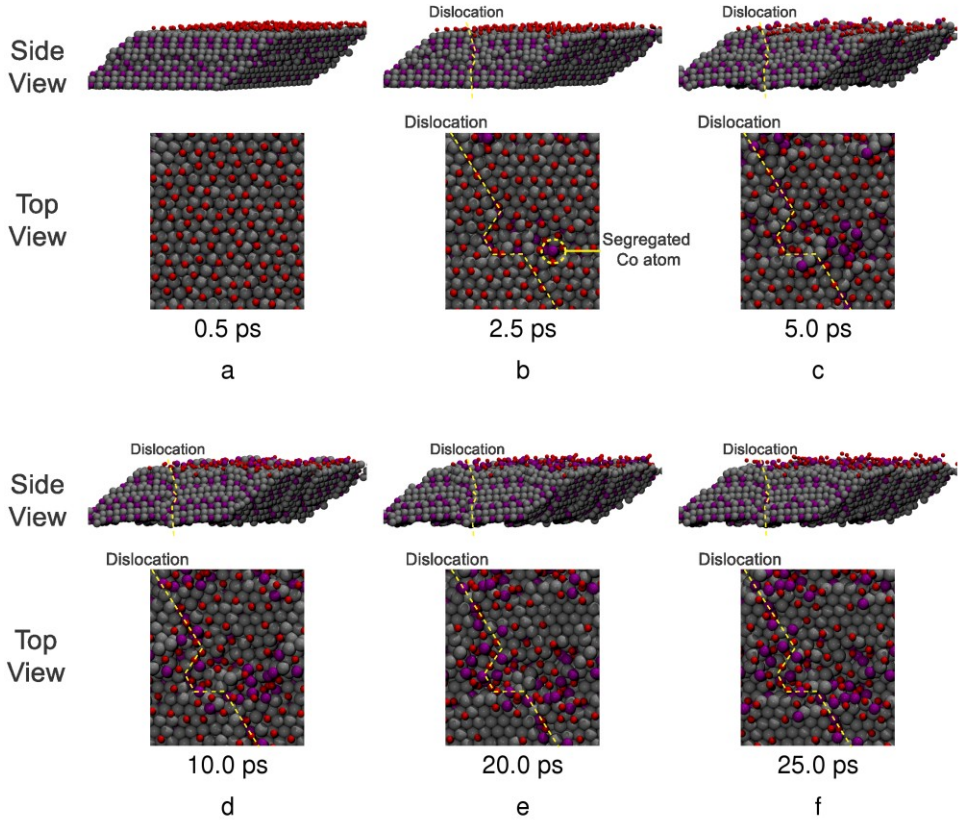

Figure III-8. Dynamics of the formation of a dislocation in the Pt/PtCo/Pt_3Co(111) surface under 0.5 ML of oxygen and 0.5 ML of water. The dislocation is identified with the dashed line, whereas oxygen, platinum, and cobalt atoms are represented as red, gray, and purple spheres, respectively. Periodic images are shown to improve the visualization and the water molecules are not shown.

The segregation of cobalt atoms to the topmost layer at the end of the simulation, clearly observed in Figure III-9, is proportional to the coverage and charge of oxygen

and may be intensified by electrostatic repulsions between charged platinum and cobalt atoms.

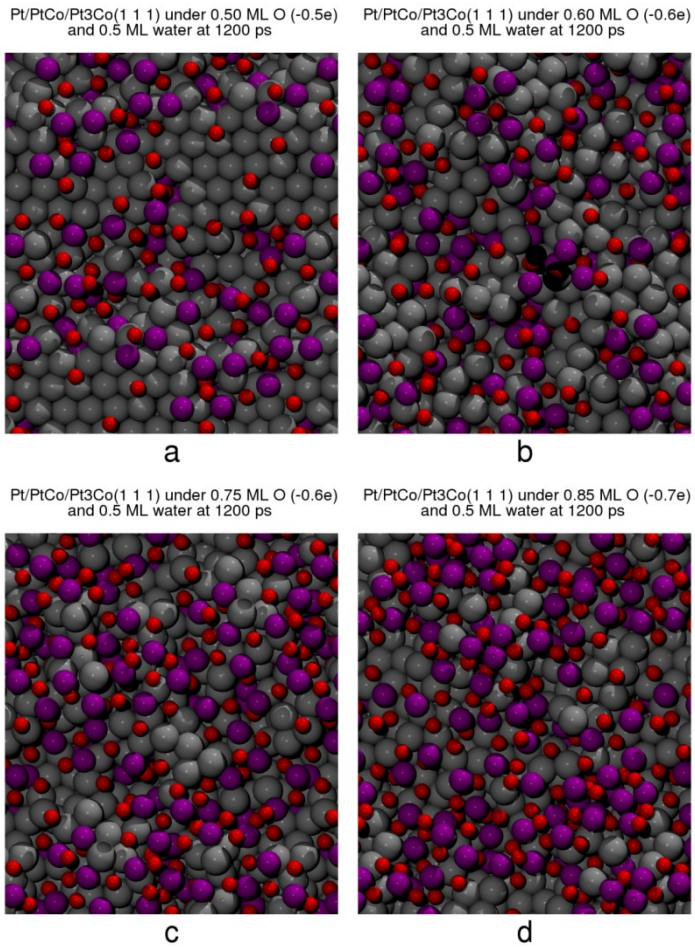

Figure III-9. Snapshots of the top view of the surface of Pt/PtCo/Pt_3Co(111) under different coverages of oxygen and water taken at the end of the simulation time. Oxygen, platinum, and cobalt atoms are represented as red, gray, and purple spheres, respectively. Periodic images are shown to improve the visualization and the water molecules are not shown.

Such Co segregation arises from the stronger affinity of Co for O than that of Pt, and is consistent with experimental and theoretical studies[52,74,75,83,84,106-108] of surface segregation in Pt-Co alloy surfaces. For coverages of oxygen higher than 0.6 ML, the topmost layer is formed mostly by cobalt atoms originally located in the subsurface. The structure of the segregated cobalt atoms is disordered with a mean distance of 3.5 Å

between them. The segregation of cobalt atoms should promote their dissolution as observed experimentally,[13] leaving in the surface zones rich in low-coordinated platinum atoms which may further dissolve.

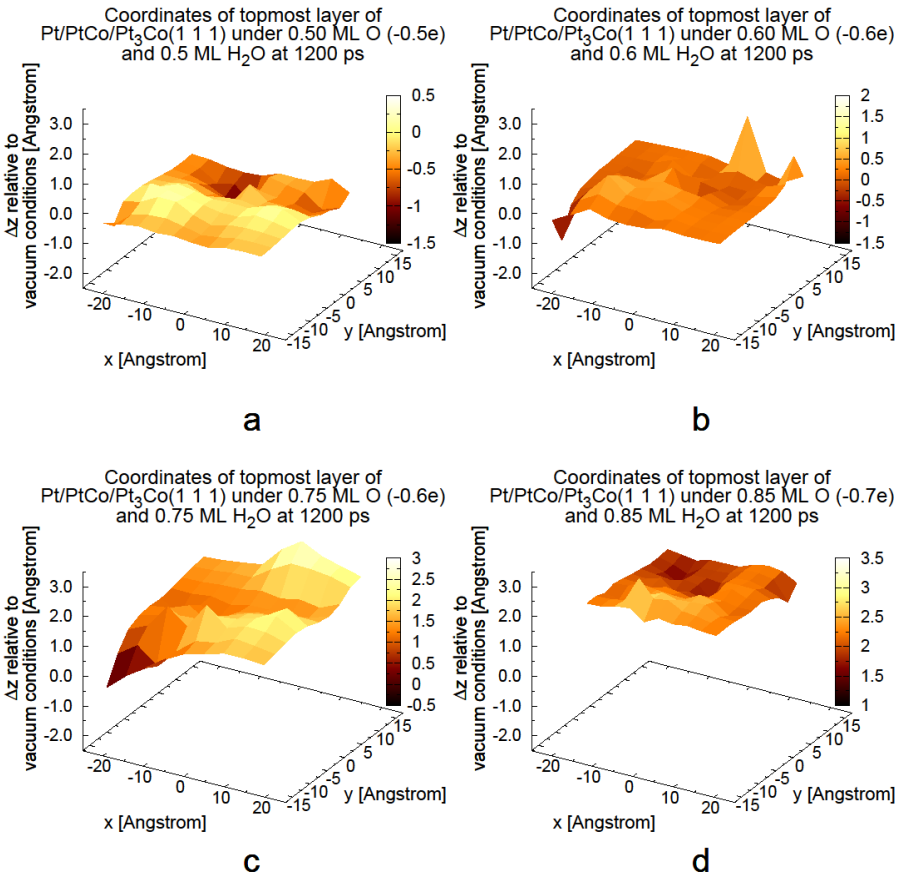

Figure III-10. Topographies of the topmost layer of Pt/PtCo/Pt_3Co(111) under different coverages of oxygen atoms and water molecules. Buckling of the atoms in the topmost layer increases with the charge of the oxygen atoms.

The effect of the coverage of oxygen on the topography of topmost layer of the Pt/PtCo/Pt_3Co surface is shown in Figure III-10. As we observed for the pure platinum surface, buckling of the topmost platinum atoms increases with the coverage of oxygen; however, for the alloy surface the magnitude of such buckling is approximately 0.5 Å greater than that for the pure Pt surface for all the coverages of oxygen. Furthermore, the charged cobalt atoms lose their ordered structure for coverages of oxygen of 0.6 ML or

greater, whereas the platinum and cobalt atoms in the core of the slab conserve their crystalline structure regardless of the presence of oxygen.

At oxygen coverages of 0.5 and 0.6 ML, most of the oxygen atoms remain adsorbed on the surface and Co—O bond is only twice more frequent than the Pt—O bond. However, for oxygen coverage of 0.85 ML most of the oxygen atoms are absorbed deeply into the subsurface and the Co—O bond is three times more frequent than the Pt—O bond. Also, the absorbed oxygen atoms show a structure with mean O—O distances of 3.2 Å, 5.0 Å, and 7.5 Å, for the first, second, and third nearest-neighbors, respectively.

As it was found for the pure Pt surface, the water molecules form a flat layer at approximately 3.5 Å from the topmost layer of the Pt/PtCo/Pt_3Co for all the coverages of oxygen.

In order to emulate the reduction process in a cyclic voltammetry experiment, we gradually reduced the charge of the oxygen atoms starting from the relaxed configuration with 0.85 ML coverage of oxygen. The oxygen atoms located in the subsurface desorb for charges of oxygen lower than -0.3e, practically all the absorbed oxygen atoms have been desorbed from the surface when their charge is 0.0e. The changes in the shape of the surface caused by the interactions with oxygen are irreversible, although most of the segregated Co atoms migrate to the core of the surface after desorption of oxygen, the steps formed in the surface remain showing Pt-rich terraces.

CHAPTER IV
MOLECULAR DYNAMICS SIMULATIONS OF SURFACE OXIDE—WATER INTERACTIONS ON Pt (111) AND PT/PTCO/ Pt/PtCo/Pt_3Co (111)*

IV.1 Motivation

Since the ORR takes place in acid medium, both activity and durability of the catalyst decay continuously while being exposed to such harsh environment. It has been shown experimentally[109] that there is a direct relationship between the degree of surface oxidation and the extent of metal dissolution, and they both correlate with the electrochemical potential. The effect of adsorbed oxygen and other adsorbates on the surface and subsurface of fuel cell catalysts has been previously studied by several theoretical reports.[19-21,110-114] Hawkins et al.[110] examined the initial stages of oxidation of the Pt(111) surface at total coverages of 0.25 to 1.0 ML using density functional theory (DFT) calculations. These authors found a strong preference for the formation and growth of one-dimensional Pt oxide chains, specifically at coverages above 0.50 ML additional oxygen atoms tend to aggregate inducing a large buckling of ~1.8 Å and oxidizing the surface Pt atoms, as reflected in their positive charges. Previous work showed the most stable configurations of oxygen absorbed in Pt(111) and Pt(100) surfaces based on DFT calculations.[19,109,113] Moreover, it was shown that increasing the on-surface oxygen or OH coverages can energetically and kinetically stabilize subsurface atomic oxygen.[19,20] Previously we showed through density functional theory (DFT) and ab initio molecular dynamics (MD) calculations that surface buckling effects are caused by adsorbed and absorbed oxygen as function of oxygen coverage, [18-21] and they are affected by the presence of acid species and solvent.[17,111] It was reported that as the degree of surface oxidation increases, surface atoms experience different degrees of buckling which is enhanced by the presence of hydronium and other oxidants such as chloride ions.[111] The detachment of buckled atoms is favored by interactions with the

---

solvent and other non-reacting species.[17] In the case of platinum alloys, large surface modifications are observed due to migration of non-noble metals from the core towards the surface.[5,8,13,14,77]

To elucidate these aspects, we recently introduced a new simulation approach,[24] aimed to investigate the effects of high surface oxidation levels on the surface structure and evolution under reaction conditions. We focus on pure Pt(111) surfaces but also on Pt-skin surfaces, specifically on Pt/PtCo/Pt_3Co alloys. In our simulations we characterize the oxidation effects by the introduction of positive charges on the metal atoms of the surface and two subsurface layers and negative charges on the adsorbed oxygen atoms. The magnitudes of these charges were obtained from DFT calculations performed under same oxidation conditions.[24] In CHAPTER III the solvent effect was incorporated using the rigid SPC/E model.[90] However, a drawback of that model is that it does not allow water dissociation which may take place on transition metal surfaces especially under certain potential conditions[17] in which also there is a high adsorbed oxygen concentration.

Here we use the CF1 central force model of water[115,116] to take into account the presence of other ORR intermediates different from atomic oxygen, since such intermediates and their interactions with the oxidized surface may be crucial to understand the overall catalytic process, especially the metal dissolution mechanism. The CF1 central force model allows the dissociation of water molecules. This feature enables our model to take into account the presence of adsorbates such OH^- or H_3O^+ in addition to atomic oxygen. Within this model both OH and H_3O bear a negative and positive charge of 0.32983 respectively.[115,116] Our simulation model is not intended to reproduce quantitatively kinetic data of the ORR. Instead, we are interested in obtaining the overall distributions of important ORR intermediates or products present on the catalytic surface and involved in the degradation process and their effect on the surface geometry and composition. The CF1 central force model for water has been validated with experimental data, e.g. it successfully reproduces the static dielectric constant and pH at 25 °C,[115] in addition to the geometric features of water molecules.[116] Further, the

model yields structure factors for liquid water that are in very good agreement with experimental values, dynamic properties as the water self-diffusion constant (monitoring O nuclei), as well as thermodynamic properties such as vaporization energy, specific heat, and isothermal compressibility.[115] In addition, the CF1 model has been recently utilized for describing proton transport in Nafion membrane in molecular simulations modeling the PEMFC.[117] Perhaps one of the most important features of the model for our application is its performance representing the behavior of water near a charged surface[118] which has been shown to be in agreement with experimental data of water near an electrode.

We begin our discussion with the analysis of the water-oxide interactions on Pt(111) and Pt/PtCo/Pt_3Co(111) surfaces with increasing oxygen coverage. Then, we present the changes in the structure and local composition of the catalyst caused by a number of cycles of reduction and oxidation. We also analyze the evolution of water and acid molecules in contact with the catalytic layer, as a function of surface oxidation/reduction conditions. Whenever possible, we refer and compare our results to experimentally observed phenomena.

IV.2 Computational details

The MD simulations were performed using DL_POLY 2.20[80-82] in the NVT ensemble with Evans thermostat at the fuel cell operation temperature of 353.15K. The system consists of ten slabs in the arrangement of the (111) face of a FCC crystal. The 10 × 10 atom-surface is composed by either pure platinum or Pt/PtCo/Pt_3Co, as described in CHAPTER III.[24] The total simulated time was 500ps in all cases (except in some indicated below where the simulation length was extended to 2 ns) with a time step of 1×10^{-4}ps.

Long-range coulombic interactions were considered between the adsorbates and the two topmost layers of the slab. Such interactions were calculated using the Ewald sum method[91,92] with a relative error of 1×10^{-3}, the accuracy of the method was verified comparing the coulombic energy and the coulombic virial. The water molecules were modeled using the CF1central force model[115,116,119] in order to take into account their

dissociation. In the CF1 central force model, water is regarded as a mixture of oxygen and hydrogen,[115] represented as distinct mass points with electrostatic charges interacting through additive pair potentials,[116] which may form stable H_2O molecules capable of dissociating and forming hydrogen bonds. The electrostatic charges of hydrogen and oxygen in the CF1 central force model are +0.32983e and -0.65966e, respectively.[115]

In our study the metal-adsorbate interactions are represented by a combination of Lennard-Jones and electrostatic interactions. The dissociation of water molecules is incorporated through the CF1 model but the dissociation of O_2 molecules is not included in our simulation model. Thus, we assume the presence of atomic oxygen (product of O_2 dissociation) adsorbing on the metal surface. When O adsorbs on the surface at relatively high concentrations ($\geq$ 0.5 ML), the surface atoms become oxidized (at different extents depending on the O concentration) and the adsorbate becomes accordingly reduced. We have determined the charges of the adsorbate (O) at various O coverages, as well as those of the corresponding top surface and subsurface at each O coverage from DFT calculations.[24,111] Therefore, we assign a negative charge to the oxygen atoms that become adsorbed on the surface and a positive charge to the metal atoms forming the two topmost layers of the surface. The different sets of charges used in this paper taken from a previous report[24] are shown in Table IV-1.

Table IV-1. Electrostatic charges (in e) of the key species for different oxygen coverages

Pt(111)				
Element	0.50 ML O	0.60 ML O	0.75 ML O	0.85 ML O
O	-0.50	-0.60	-0.60	-0.70
Pt in topmost layer	+0.20	+0.30	+0.40	+0.50
Pt in second layer	+0.05	+0.06	+0.05	+0.10
$Pt/PtCo/Pt_3Co(111)$				
Element	0.50 ML O	0.60 ML O	0.75 ML O	0.85 ML O
O	-0.50	-0.60	-0.60	-0.70
Pt in topmost layer	+0.05	+0.135	+0.15	+0.195
Pt in second layer	0.00	0.00	0.00	0.00
Co in second layer	+0.40	+0.45	+0.60	+0.80

The magnitude of such charges was set according to the average surface or subsurface values obtained with the Bader charge analysis[93-96] from density functional theory (DFT) calculations. Hence, we incorporate the effect of varying the electrochemical potential by changing the electrostatic charge of the oxygen atoms and topmost metal atoms of the surface. This novel simulation approach has successfully reproduced the main features of the oxide growth observed experimentally [13,78,101-105] as we reported recently.[24]

The short-range metal-metal and metal-adsorbate interactions were represented through the Lennard-Jones (LJ) potential using the parameters reported in Table III-1 and the Lorentz-Berthelot mixing rules. The LJ parameters for the Pt—Pt and Co—Co interactions were obtained by fitting to the Sutton-Chen[85,86,89] potential energy surface for pure species.[87] For Pt—Pt the LJ parameters were taken from the literature;[88] a new parameterization was done for the Co—Co interactions, whereas the LJ parameters for the O—O interactions were taken from the SPC/E model.[90] The LJ interactions of hydrogen atoms with other species were neglected, and the H—H, H—O, and H—cation interactions were represented by the CF1 potential.

Table IV-2. Interaction energy (ε) and length (σ) parameters for the Lennard-Jones potential

Interaction	ε(eV)	σ(Å)
Pt-Pt	0.2013	2.410
Co-Co	0.1513	2.180
O-O	0.0067	3.165
Anion-anion*	0.00495	4.417

* The anion represents chloride ion in HCl. Although HCl is a strong acid, the electrostatic charges of the anion and cation are assigned the same magnitude as that of the CF1 proton, to facilitate acid dissociation in the simulated acidic environment.

The metal-adsorbate potential qualitatively reproduces the geometries on the adsorbates on the surface. O adsorbs in hollow site and OH on top site and average distances taken from the simulations are shown Table IV-3.

Table IV-3. Average bond distances (in Å) of the adsorbates to the metal surface atoms

Adsorbate	Pt(111) under 0.85 ML O and H2O	Pt/PtCo/Pt_3Co(111) under 0.85ML O and H2O	
		to surface Pt	to surface Co
H	2.20	2.35	2.20
O	2.80	2.80	2.60
OH	2.90	2.40	1.90
H2O	3.00	3.10	2.90
H3O	3.37	6.00	4.30

The acid molecules were described as two point charges with opposing magnitudes of 0.32983e to match the proton charges used by the CF1 model. The LJ interactions between chloride anions were taken from the literature,[120] whereas the cations (which can be visualized as H^+) interacted with water molecules using the CF1 model. In the initial configuration, acid molecules were randomly placed at least 5Å from the surface with a bond distance between the constituent ions of 1.27Å.[121] According to the volume of the simulation box, we introduced 10 acid molecules into the central box to represent an approximated value of pH of 3. During the simulation, the acid molecules may dissociate due to their interactions with water molecules. According to experimental and theoretical evidence,[122] four water molecules are required to dissociate a molecule of HCl. In this work the ratio of acid to water molecules is 10:85. Note also that the simulated acid does not exactly correspond to HCl but to a slightly weaker acid, since the magnitudes of the electrostatic charges were reduced to equate the proton charges of water, thus facilitating acid dissociation.

Note that our water model can be viewed as a molten salt (composed by H^+ and O^- species) which is able to form stable H_2O molecules but also hydronium ions. These H_3O^+ ions may be present on the catalytic surface due to water decomposition: $2H_2O \rightarrow H_3O^+ + OH^-$, this is a reaction step in some proposed ORR mechanisms. For example it

is well known that water molecules may directly dissociate into OH radicals due to interactions with atomic oxygen.[123] The H_3O^+ species in our simulation model may in turn dissociate (since it is governed by the CF1 model that allows dissociation) to form other adsorbates like OH^-, H_2O, H^+, due to electrostatic interactions between H_3O^+ and water molecules, adsorbed oxygen atoms, acid species, and the topmost metal layers of the catalyst.

To emulate a cyclic voltammetry experiment, we gradually reduced the charges of the oxygen and surface atoms starting from the relaxed configuration with 0.85 ML coverage of oxygen until reaching neutrality. Then the charges of oxygen and slab surface atoms were gradually increased until their original values are recovered, forming a cycle. We repeated this process several times, relaxing the system for 300 ps for each set of charges and taking the relaxed configuration as the initial one for the next set of charges.

The figures and plots presented in this chapter were prepared using VMD,[98] gnuplot,[99] and sK1.[100]

IV.3 Results and discussion

Figure IV-1 shows the z-density profiles, i.e., the number of atoms found on a plane located at position *z* in the vertical direction perpendicular to the surface. The z-density profiles include the species on Pt(111) and Pt/PtCo/Pt_3Co(111) surfaces under different oxygen coverages (0.5 to 0.85 ML) in presence of 0.85 ML of water molecules. In the pure platinum slab, oxygen is found in the subsurface for coverages of 0.6 ML or higher, whereas in the alloy slab oxygen migrates into the subsurface for all the studied coverages. This is in agreement with DFT studies of O migration into the subsurface of alloys, where it was shown that such migration may become facilitated by the presence of less noble metals such as Co.[19,21] While the metal core and surface structures show their crystallinity in all cases for the pure Pt slab (see Figure IV-1a-d), the alloy structure appears somehow amorphous from the z-density profiles. However, as reported in detail previously[24], this is only a visualization effect caused by a dislocation formed in the Pt/PtCo/Pt_3Co(111) slab under 0.5 ML oxygen (Figure IV-1e) due to the segregation of

Co atoms; i.e., the structure is changed but remains crystalline. The distance between the atomic oxygen on the surface and the oxygen of water molecules is approximately 2.9 Å in both surfaces. Hydrogen bonding is observed between adsorbed atomic oxygen and water hydrogen atoms, and among water molecules, the mean O…H distance is approximately 1.8 Å, such distance decreases slightly with increasing oxygen coverage due to stronger electrostatic interactions.

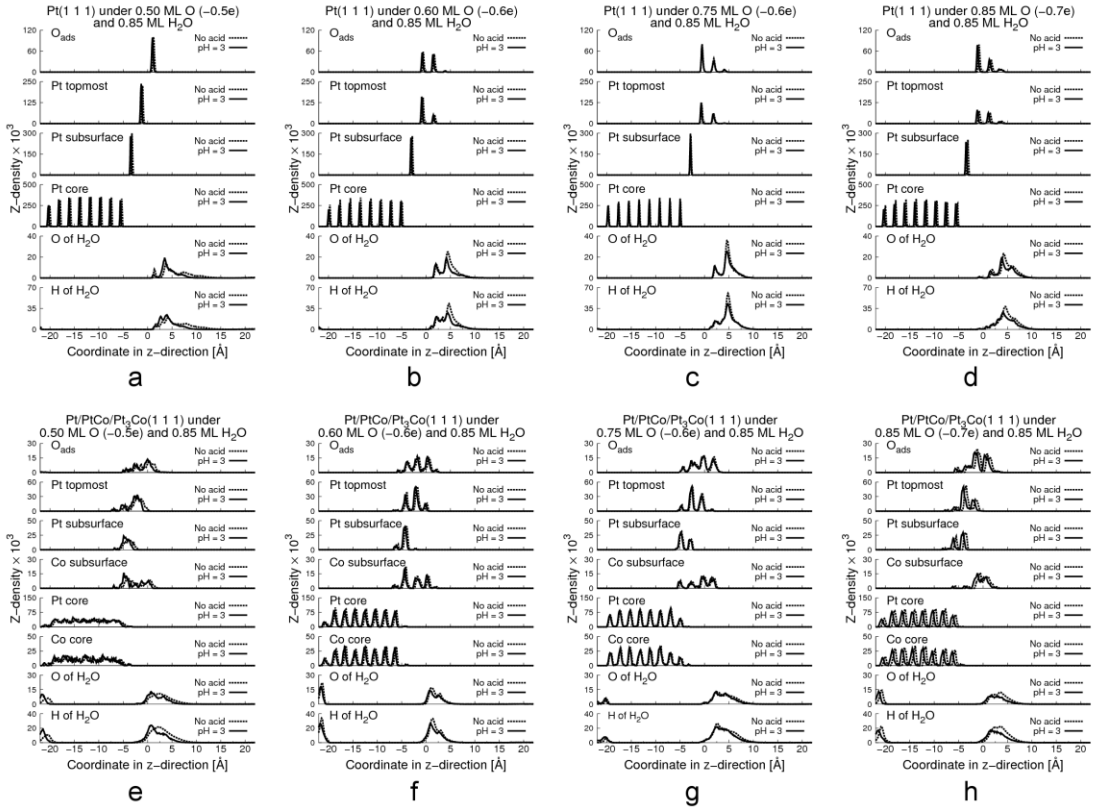

Figure IV-1. Z-density profiles of Pt(111) (a-d)and Pt/PtCo/Pt_3Co(111) (e-h) under increasing coverages of oxygen atoms and 0.85 ML water.

The effect of acid molecules on the overall structure of the surface is practically negligible in both systems. However, they contribute to the formation of OH and H_3O intermediates in both surfaces which become adsorbed as it is shown in Table IV-4 and Table IV-5, and Figure IV-2 to Figure IV-4. The amount of OH radicals observed on the Pt/PtCo/Pt_3Co slab under pH=3 is greater than the one on the pure Pt slab under the

same conditions for oxygen coverages of 0.6ML or greater. This implies, within the framework of our model, a higher activity of the alloy surface than the Pt surface, in agreement with several experimental reports.[6,13,124] On both surfaces under pH=3, the OH radicals are surrounded by approximately 10 water molecules at 2.5 Å forming hydrogen bonds with other water molecules. Compared to the case where no acid is present, the OH radicals' solvation by water is increased in both surfaces due to the presence of ions from dissociated acid molecules. The average number of water molecules increases from 5 water neighbors at 2.5 Å to around 10 water neighbors at the same distance, as it is observed in Figure IV-2 for the Pt/PtCo/Pt_3Co(111) surface. Ions from dissociated acid molecules are located near to OH radicals and induce changes in their orientation, enhancing the formation of hydrogen bonds with water molecules. In the alloy surface, water molecules prefer to arrange over Pt atoms rather than over segregated and oxidized Co atoms to minimize electrostatic repulsions. The results shown in Table 4 correspond to simulation lengths of 500 ps; however, longer simulations of 2 ns yielded negligible variations in the values reported.

Table IV-4. Average number of adsorbates involving H in the simulation cell of Pt(111) surfaces. Acid protons not included.

	0.50 ML O		0.60 ML O		0.75 ML O		0.85 ML O	
Adsorbate	No acid	pH = 3	No acid	pH = 3	No acid	pH = 3	No acid	pH = 3
H	8	16	6	14	7	15	3	17
OH	5	10	5	10	5	4	1	6
H2O	77	68	75	66	75	79	83	74
H3O	1	6	3	8	3	1	0	3

Table IV-5. Average number of adsorbates involving H in the simulation cell of Pt/PtCo/Pt_3Co(111) surfaces.

	0.50 ML O		0.60 ML O		0.75 ML O		0.85 ML O	
Adsorbate	No acid	pH = 3	No acid	pH = 3	No acid	pH = 3	No acid	pH = 3
H	6	20	6	19	2	15	7	18
OH	6	9	6	12	0	6	5	9
H2O	76	68	73	64	84	75	79	72
H3O	2	5	4	7	0	3	0	3

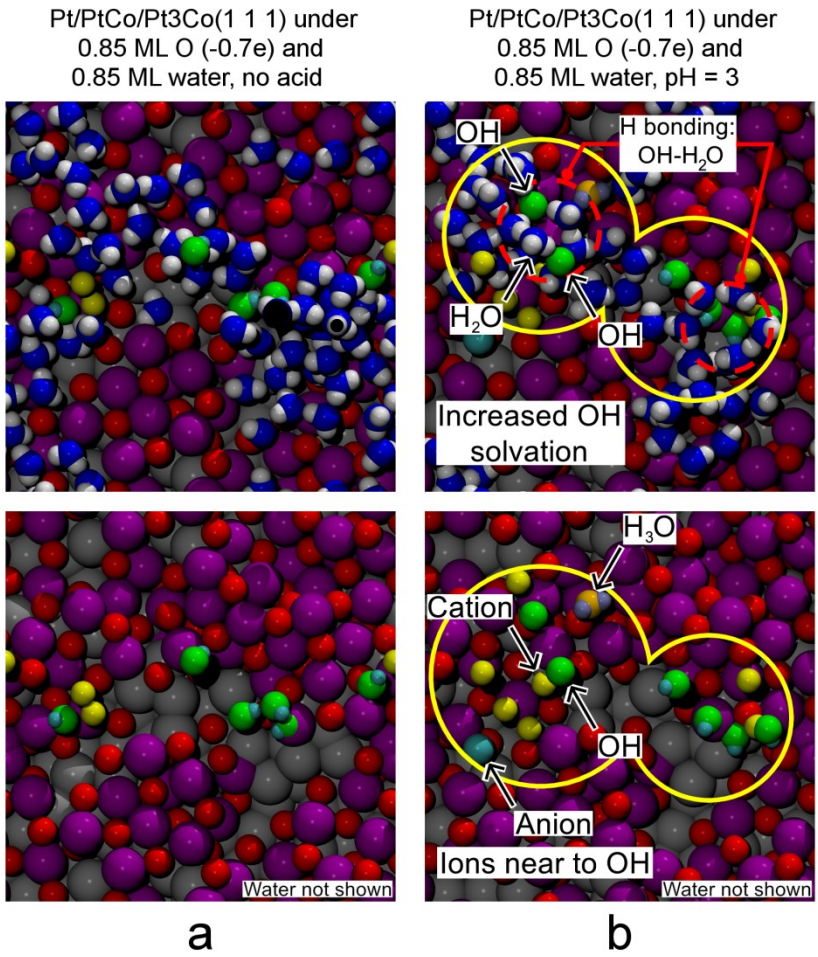

Figure IV-2. Snapshots of the surface of Pt/PtCo/Pt_3Co(111) under 0.85 ML oxygen and water without acid molecules (a) and at pH = 3 (b) after500 ps. The water molecules are not shown in the second row of images. Color key: platinum-grey, cobalt-purple, oxygen-red, cation-yellow, OH-green, H2O-blue and white, H3O-orange and purple, anion-cyan.

Figure IV-3 and Figure IV-4 show snapshots of the configuration of the system after 500 ps for Pt(111) and Pt/PtCo/Pt_3Co(111) surfaces, respectively. Water molecules agglomerate in regions of the surface on both systems under all the studied coverages of oxygen forming hydrogen bonds among themselves and with the adsorbed O atoms. Such agglomerations have been detected experimentally on clean Pt(111) surfaces by Ogasawara et al.[125] using infrared absorption spectroscopy. These authors reported that hydrogen bonding causes strong lateral interactions inducing the clustering of water molecules. In the alloy slab surface, our simulations show that the agglomerations are located over the Pt atoms that remain in the topmost layer (Figure IV-4), the Co

segregation is evident in all cases and it increases with the coverage of oxygen. The formation of OH molecules mainly occurs after water agglomeration and it is favored by the surface steps produced by buckling of metal atoms which takes place mostly in the boundaries of the agglomerations of water. These results are in agreement with temperature-programmed desorption measurements and DFT calculations,[126,127] which show that the adsorption energy of OH is sensitive to the coordination number of the Pt atoms on the surface, and that hydrogen-bonded OH—H_2O dimers are adsorbed along the steps of Pd (101) surfaces. Moreover, in the Pt/PtCo/Pt_3Co system water dissociation occurs in the stepped regions formed by Pt atoms which remain on the topmost layer and Co atoms segregated from the subsurface.

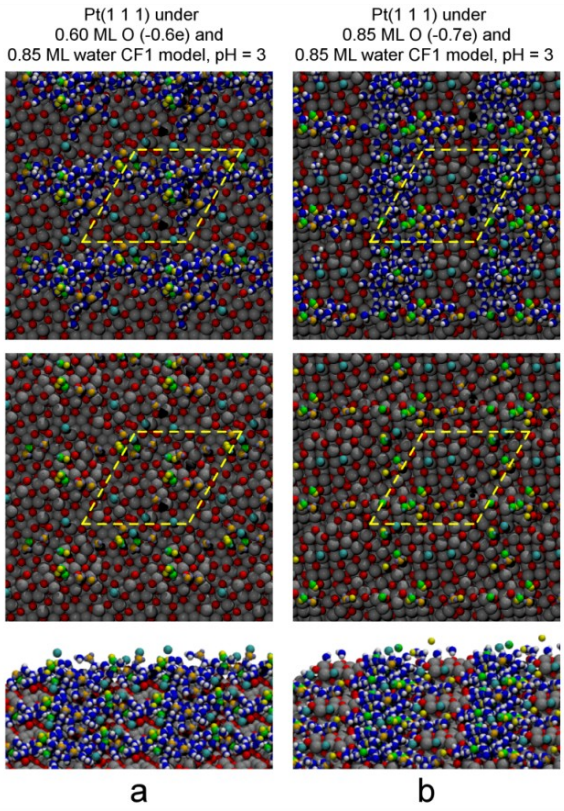

Figure IV-3. Snapshots of the surface of Pt(111) under different coverages of oxygen and 0.85 ML water taken at the end of the simulation time. Periodic images are shown to improve the visualization; the simulation cell is shown as a dashed line. The water molecules are not shown in the second row of images. Color key: platinum-grey, oxygen-red, cation-yellow, OH-green, H2O-blue and white, H3O-orange and purple, anion-cyan.

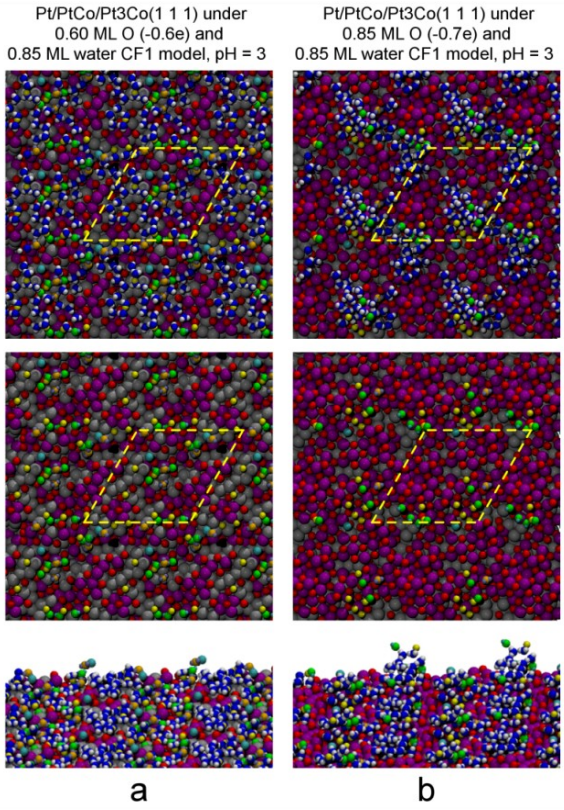

Figure IV-4. Snapshots of the surface of Pt/PtCo/Pt_3Co(111) under different coverages of oxygen and 0.85 ML water taken at the end of the simulation time. Periodic images are shown to improve the visualization; the simulation cell is shown as a dashed line. The water molecules are not shown in the second row of images. Color key: platinum-grey, cobalt-purple, oxygen-red, cation-yellow, OH-green, H2O-blue and white, H3O-orange and purple, anion-cyan.

The agglomeration of water molecules is formed in the early stages of the simulation and it is stable as illustrated in Figure IV-5. The formation of OH and H_3O molecules occur after water is agglomerated. Table IV-6 shows the number of OH and H_3O molecules as a function of time on the alloy system for the highest studied coverage of oxygen, the number of OH radicals increases with time whereas the number of H_3O molecules reaches an approximately constant value after 150 ps. The presence of adsorbed OH—H_2O complexes on oxidized noble metals has been reported experimentally and through DFT analysis in several publications.[106,127-129] Kan et al. [127] studied the adsorption of water on a PdO(101) thin film using temperature-programmed desorption measurements and DFT calculations. They found that water desorbs from a multilayer which appears to be stabilized by direct interactions with the oxidized surface

and that the HO—H_2O complex is highly favored at low water coverages along the coordinatively unsaturated Pd atoms. Moreover, Gong and Zhou[128] studied platinum dioxide and dioxygen complexes using matrix isolation infrared spectroscopy and DFT calculations. These authors showed that the hydrogen bonding interactions between Pt oxide and water molecules affect the binding energy of water. These findings are in qualitative agreement with the results discussed above in which water molecules seem to be stabilized by interactions with the oxidized surface and OH molecules, especially at stepped sites formed by the absorption of oxygen in the subsurface and surface segregation of Co in the alloy system.

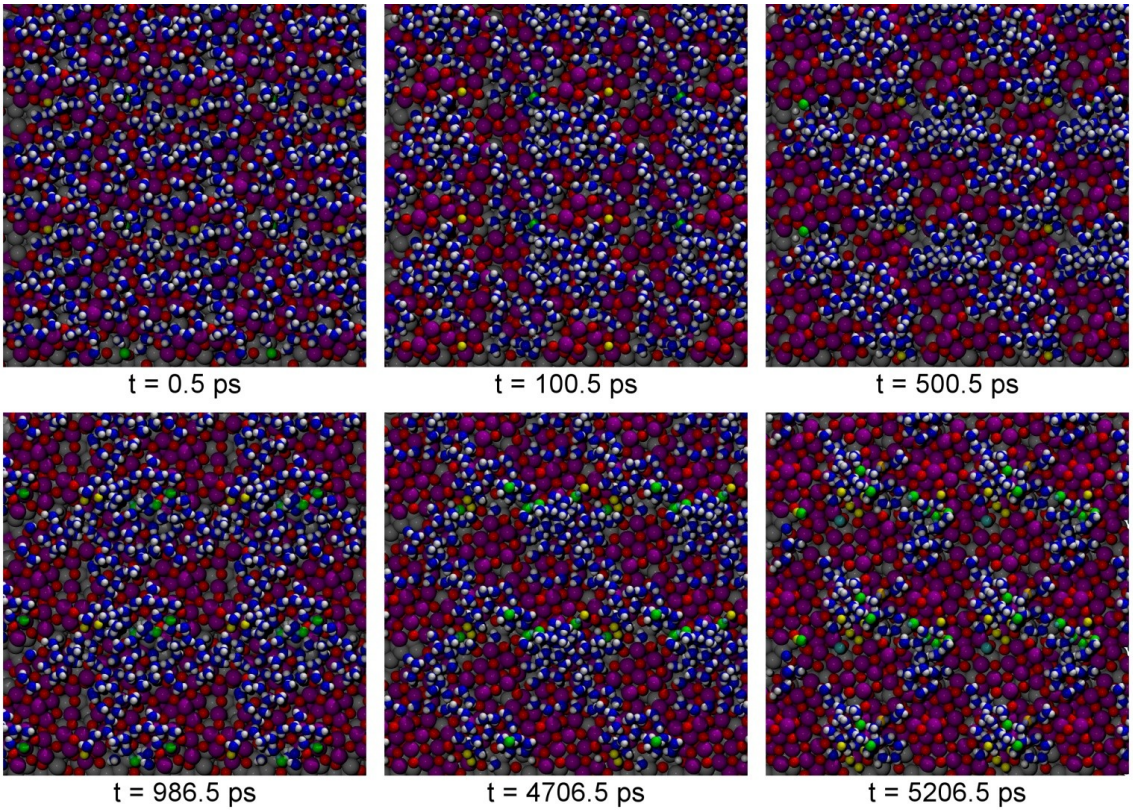

Figure IV-5. Dynamics of water agglomeration on Pt/PtCo/Pt_3Co (111) under 0.85 ML of oxygen, 0.85 ML of water, and pH = 3. Periodic images are shown to improve the visualization. Color key: platinum-grey, cobalt-purple, oxygen-red, cation-yellow, OH-green, H_2O-blue and white, H_3O-orange and purple, anion-cyan.

The simulated time was chosen to be long enough to allow the system to be equilibrated by tracking its overall energy. In all the simulations the total energy of the system converges to a mean value with fluctuations of magnitude of less than 2% of the total energy, as it is shown below in Figure IV-6 for one of the studied cases of the alloy system. Since various different initial configurations have been tested, we conclude that our results are independent of the initial configuration of the system. We incorporated the water molecules into the system using the relaxed oxidized surfaces, in the first stage we used the SPC/E model and the system was equilibrated under these conditions (as we reported previously[24]). Using the resultant relaxed configuration we replaced the SPC/E model with the CF1 model allowing the system to relax again.

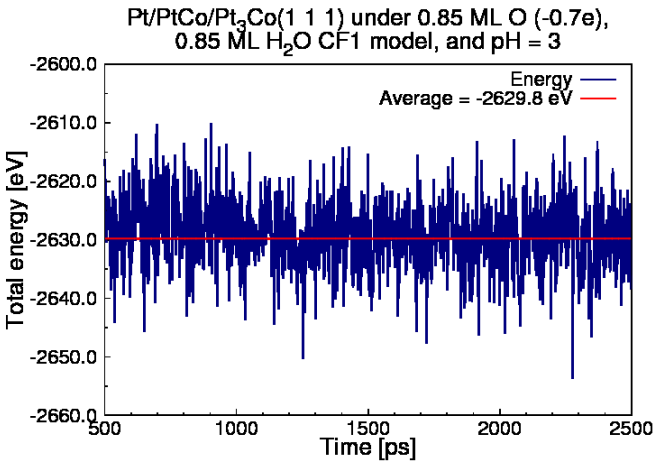

Figure IV-6. Total energy of the Pt/PtCo/Pt_3Co system under 0.85 ML of O, H_2O, and pH=3 as a function of time. After 500 ps this quantity fluctuates around an average value of -2629.8 eV, proving that the system is equilibrated.

The dissociation of water yields to approximately constant values of the number of different adsorbates after the equilibration period, as shown in Figure IV-7.

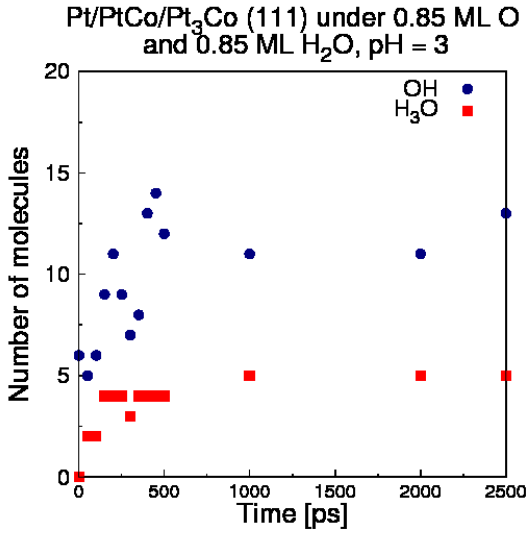

Figure IV-7. Profiles of the number of OH and H_3O molecules per unit cell on Pt/PtCo/Pt_3Co (111) under 0.85 ML of oxygen, 0.85 ML, and pH = 3. After ~500 ps the numbers take an approximately constant value.

In order to emulate a cyclic voltammetry experiment, we gradually reduced the charges of the oxygen and surface atoms of the systems under 0.85 ML of oxygen. Once neutrality was attained, the charges were gradually increased until recovering their original values.

The Z-density profiles and snapshots of the surface of both studied systems after one and ten cycles are shown in Figure IV-8 and Figure IV-9.

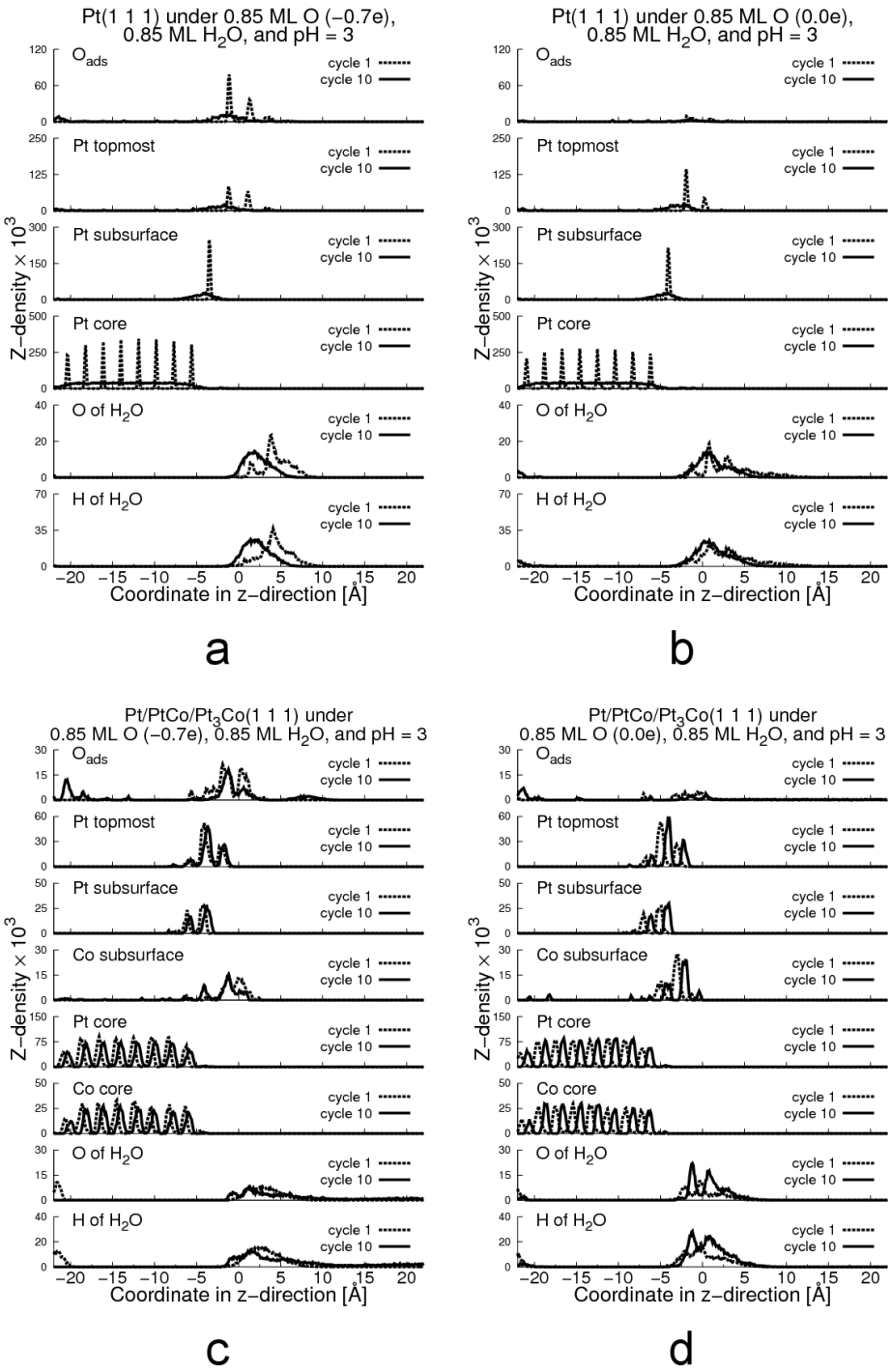

Figure IV-8. Z-density profiles of Pt (111) (a and b) and Pt/PtCo/Pt_3Co (111) (c and d) under cycles of reduction and oxidation.

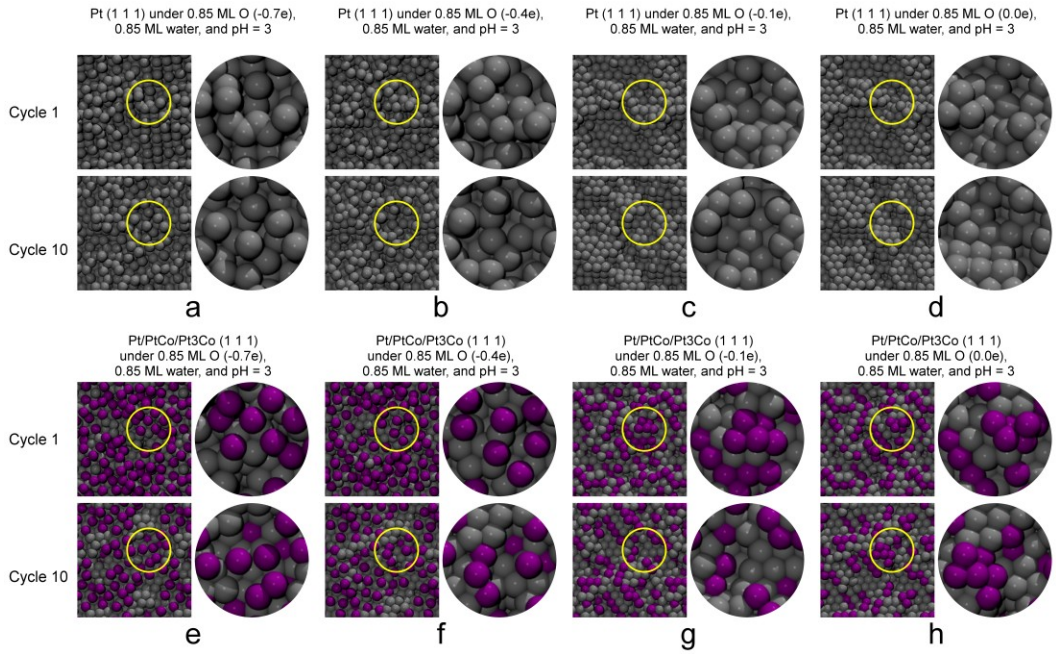

Figure IV-9. Snapshots of Pt (111) (a-d) and Pt/PtCo/Pt_3Co (111) (e-h) under cycles of reduction and oxidation. In order to improve the visualization, periodic images are shown and all the adsorbates are hidden. Pt and Co atoms are represented as gray and purple spheres, respectively.

In the pure Pt slab, the structural changes after ten cycles are dramatic, the core layers are not well defined due to the migration of Pt atoms, this may be observed as an absence of well-defined peaks in the plot of "Pt" species in Figure IV-8a-d. Moreover, regions of steps and kinks are formed on the topmost layers, as it is shown in Figure IV-9a-d. The absorption and desorption of oxygen in the subsurface causes the formation of vacancies in the topmost layers as the reduction-oxidation cycles take place; these vacancies enhance the absorption of oxygen deeper in the core of crystal as the number of cycles increases. This process provokes the rearrangement of the Pt atoms in the core causing a distortion of the layers of the surface. In contrast, in the Pt/PtCo/Pt_3Co system the structural changes are not as evident as in the pure slab. After 10 reduction-oxidation cycles, we only observed a buckling of approximately 1 Å in the z-axis direction in the whole slab.

Table IV-6 and Table IV-7 display the number of adsorbates involving H as a function of the charge of the oxygen atoms and number of cycles of reduction and oxidation on Pt and Pt/PtCo/Pt_3Co surfaces. There is a decrease in the number of OH

molecules as the reduction-oxidation after 10 cycles in the alloy slab, which indicate catalyst degradation, in agreement with several experimental reports.

Table IV-6. Average number of adsorbates involving H on Pt (111) under cycles of reduction and oxidation, and pH = 3. The charge on the atomic O (qO), in e, is indicated.

	qO=-0.70 e		qO=-0.40 e		qO=-0.10 e		qO=0.0 e	
Adsorbate	Cycle 1	Cycle 10	Cycle 1	Cycle 10	Cycle 1	Cycle 10	Cycle 1	Cycle 10
H	17	16	15	17	18	14	13	15
OH	6	5	7	7	7	6	5	7
H2O	74	75	73	72	73	74	75	73
H3O	3	3	4	4	3	4	4	4

Table IV-7. Average number of adsorbates involving H on Pt/PtCo/Pt_3Co(111) under cycles of reduction and oxidation, and pH = 3.

	qO= -0.70 e		qO= -0.40 e		qO= -0.10 e		qO= 0.0e	
Adsorbate	Cycle 1	Cycle 10	Cycle 1	Cycle 10	Cycle 1	Cycle 10	Cycle 1	Cycle 10
H	20	7	22	17	8	17	15	17
OH	9	6	9	6	8	6	7	6
H2O	71	74	70	74	71	74	73	74
H3O	3	3	3	3	4	3	4	3

CHAPTER V
MOLECULAR DYNAMICS SIMULATIONS OF SURFACE OXIDATION ON Pt AND Pt/PtCo/Pt_3Co NANOPARTICLES SUPPORTED OVER CARBON*

V.1 Motivation

The electrode-nanocatalysts are exposed under operating conditions to acid medium and large electrode potential excursions during the start-and-stop process, causing their decay through dissolution of metal atoms. Experimental studies have shown a direct relationship between the degree of surface oxidation and the extent of metal dissolution,[109] and that both correlate with the electrochemical potential. The oxidation of Pt surfaces has been widely studied experimentally and theoretically,[19-21,109-114] although most studies focus on the understanding of the interactions of adsorbates with perfect crystal surfaces, the physicochemical phenomena taking place in a catalytic nanoparticle involves its different facets or defects, since Pt nanoparticles in the range of 2-5nm have about 40% (111) facets, a similar percent of edges and corners whereas the additional 20% are (100) surfaces.[39] It has been found that the different Miller planes of Pt crystals exhibit different behavior in the adsorption and absorption of oxygen.[20,71,130] Moreover, we have shown previously through density functional theory (DFT) and ab initio molecular dynamics (MD) calculations that surface buckling effects are caused by adsorbed and absorbed oxygen as function of oxygen coverage,[18-21] and they are affected by the presence of acid species and solvent.[17,111] Therefore, a realistic simulation model of a catalytic nanoparticle for the ORR needs to consider the different facets of a catalytic nanoparticle, a detailed representation of the adsorbates and water molecules, and it has to take into account the presence of acid molecules. In this work we use the molecular simulation approach we reported recently[24] in which we combine MD and DFT calculations, to simulate the surface oxidation on Pt and Pt/PtCo/Pt_3Co supported nanoparticles over carbon in presence of water and acid molecules, in order to elucidate

---

the mechanism of metal dissolution due to variations in the fuel cell operation conditions.

V.2 Computational details

The MD simulations were performed using DL_POLY 2.20[80-82] in the NVT ensemble with Evans thermostat at the fuel cell operation temperature of 353.15K. The system consists of a nanoparticle supported over a two-layer graphite substrate, as it is shown in Figure V-1. The nanoparticle has a 40 Å diameter and it is composed by either pure platinum or Pt(outmost layer)/PtCo(second layer)/Pt_3Co(core); the latter is the most stable configuration of a Pt_3Co alloy.[52,83,84] The initial configuration of the nanoparticles was generated using face centered cubic (FCC) cells which were added successively around a central one until a cubo-octahedral cluster of the desired diameter was obtained. The number of atoms constituting the nanoparticle and support is shown in Table V-1, a fraction of a monolayer of oxygen atoms (based in the number of outmost charged Pt atoms of the nanoparticle) and an equal number of water molecules are placed randomly surrounding the nanoparticle (at a minimum distance of 6.0 Å from the outmost layer of the nanoparticle). The carbon layers are fixed in all the simulations and orthorhombic periodic boundary conditions were used with a vacuum of 160 Å in the z-direction perpendicular to the surface. The total simulated time was 600 ps in all cases with a time step of 1×10^{-4}ps.

Table V-1. Number of atoms constituting the nanoparticle and support in the two simulation systems used in this work. The metal atoms in the first and second layers are positively charged representing the oxidized surface (see text)

Pt	Number of atoms
Pt charged in outmost layer	665
Pt charged in second layer	441
Pt neutral	1017
C support	9216
Pt/PtCo/Pt3Co	
Pt charged in outmost layer	665
Pt charged in second layer	308
Co charged in second layer	133
Pt neutral	809
Co neutral	208
C support	9216

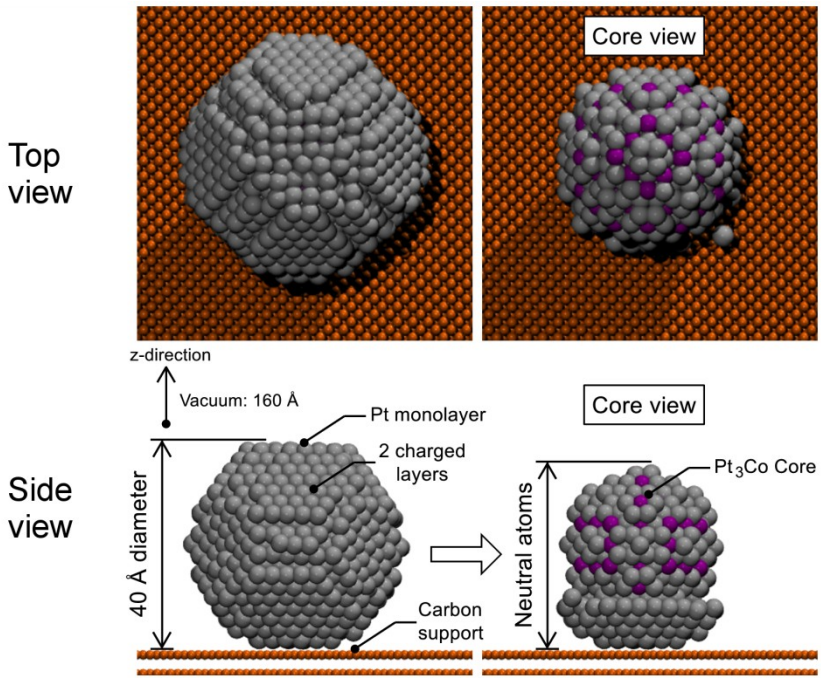

Figure V-1. Initial configurations of the supported alloy nanoparticles exposed to oxygen and water.

Long-range coulombic interactions were considered between the adsorbates and the metal atoms of the two outmost layers of the nanoparticle which are located four layers from the support in the z-direction, all the other atoms constituting the nanoparticle and support are considered neutral, as it is shown in Figure V-1. The

coulombic interactions were calculated using the Ewald sum method[91,92] with a convergence parameter of 0.001 $Å^{-1}$ and 20 × 20 × 4 k-vectors in x, y, and z directions, respectively; the accuracy of the method was verified comparing the coulombic energy and the coulombic virial.

The water molecules were modeled using either with the SPC/E model [90] or the CF1central force model.[115,116,119] The latter model is able to take into account the dissociation of water molecules since they are regarded as a mixture of oxygen and hydrogen[115] represented as distinct mass points with electrostatic charges interacting through additive pair potentials.[116] The oxygen and hydrogen atoms may form stable H_2O molecules capable of dissociating and forming hydrogen bonds. The electrostatic charges of hydrogen and oxygen in the CF1 central force model are +0.32983e and -0.65966e, respectively;[115] whereas in the SPC/E model the charge of H is +0.4238e and the charge of O is -0.8476e.

To represent the oxidized surface, we assigned a negative charge to the oxygen atoms that will become adsorbed on the surface and a positive charge to a fraction of the metal atoms forming the two outmost layers of the nanoparticle. The different sets of charges used in this chapter were taken from a previous report[24] and are shown in Table IV-1. The magnitude of such charges was set according to the average surface or subsurface values obtained with the Bader charge analysis[93-96] from density functional theory (DFT) calculations.

Table V-2. Electrostatic charges (in e) of the key species for different oxygen coverages

Pt				
Element	0.50 ML O	0.60 ML O	0.75 ML O	0.85 ML O
O	-0.50	-0.60	-0.60	-0.70
Pt in outmost layer	+0.20	+0.27	+0.34	+0.45
Pt in second layer	+0.08	+0.14	+0.17	+0.22
$Pt/PtCo/Pt_3Co$				
Element	0.50 ML O	0.60 ML O	0.75 ML O	0.85 ML O
O	-0.50	-0.60	-0.60	-0.70
Pt in outmost layer	+0.18	+0.26	+0.32	+0.43
Pt in second layer	0.00	0.00	0.00	0.00
Co in second layer	+0.36	+0 .51	+0.64	+0.85

The short-range metal-metal and metal-adsorbate interactions were represented through the Lennard-Jones (LJ) potential using the parameters reported in Table III-1 and the Lorentz-Berthelot mixing rules. The LJ parameters for the Pt—Pt and Co—Co interactions were obtained by fitting to the Sutton-Chen[85,86] potential energy surface for pure species.[87 89] For Pt—Pt the LJ parameters were reported previously,[88] a similar new parameterization was done for the Co—Co interactions, whereas the LJ parameters for the O—O interactions were taken from the SPC/E model.[90] The LJ interactions of hydrogen atoms with other species were neglected, except for H—H, H—O, and H—cation interactions that were represented using the CF1 potential. The parameters for the C-C interactions were taken from the literature.[131] The Pt—C interactions are also modeled with LJ potentials as in previous work.[131]

Table V-3. Interaction energy (ε) and length (σ) parameters for the Lennard-Jones potential

Interaction	ε(eV)	σ(Å)
Pt—Pt	0.2013	2.410
Co—Co	0.1513	2.180
O—O	0.0067	3.165
Anion—anion*	0.00495	4.417
C—C	0.00242	3.400

* The anion represents chloride ion in HCl. Although HCl is a strong acid, the electrostatic charges of the anion and cation are assigned the same magnitude as that of the CF1 proton, to facilitate acid dissociation in the simulated acidic environment.

On the other hand, the acid molecules were represented as two point charges with opposing magnitudes of 0.32983e to match the proton charges used by the CF1 model. The LJ interactions between chloride anions were taken from the literature,[120] whereas the cations (which can be visualized as H^+) interacted with water molecules using the CF1 model. In the initial configuration, acid molecules were randomly placed at least 5Å from the outmost layer of the nanoparticle with a bond distance between the constituent ions of 1.27Å.[121] According to the volume of the simulation box, we introduced 67 acid molecules into the system to represent an approximate value of pH of 3. Note that although this pH may be a little higher than that existent in actual fuel cell conditions,

simulations at lower pH values would only require more HCl and H_2O molecules. However, we believe that the used number of acid molecules captures the overall effect of ions and the solvent on the oxidation process because the entire surface of the nanoparticle becomes in contact with the dissociated ions and solvent. During the simulation, the acid molecules may dissociate due to their interactions with water molecules. According to experimental and theoretical evidence,[122] four water molecules are required to dissociate a molecule of HCl. In order to facilitate acid dissociation, the ratios of acid to water molecules used in this work are 67:333, 67:399, 67:499, and 67:566, for coverages of oxygen of 0.5, 0.6, 0.75, and 0.85 ML, respectively. Note also that the simulated acid does not exactly correspond to HCl but to a slightly weaker acid, since the magnitude of the electrostatic charges were reduced to equate the proton charges of water, thus facilitating acid dissociation.

To emulate a cyclic voltammetry experiment, we gradually reduced the charges of the oxygen and charged atoms in the nanoparticle starting from the relaxed configuration with 0.85 ML coverage of oxygen until reaching neutrality. Then the charges of oxygen and outmost atoms of the nanoparticle were gradually increased until their original values are recovered, forming a cycle. We repeated this process several times, relaxing the system for 25 ps for each set of charges and taking the relaxed configuration as the initial one for the next set of charges. The figures and plots presented in this paper were prepared using VMD,[98] gnuplot,[99] and sK1.[100]

V.3 Results and discussion

We begin discussing the simulation of the surface oxidation of pure Pt and Pt/PtCo/Pt_3Co supported nanoparticles under different coverages of oxygen and water, we compare the results obtained using the SCP/E and CF1 central force models to represent the water molecules and considering the presence of acid molecules. Then, we present the results of the emulation of cycling voltammogram experiments through cycles of reduction and oxidation. We observed dissolution of metal atoms after ten cycles under pH = 3.

V.3.1 Oxidation

The R-density profiles presented in this work provide the distribution of the number of atoms of the species as a function of the distance to the center of mass of the nanoparticle. Figure V-2 shows the R-density profiles of Pt and Pt/PtCo/Pt_3Co nanoparticles supported on C under different coverages of oxygen and water, using the SPC/E and CF1 models to represent water molecules. It is observed that the local composition on the surface and the structure of the oxidized nanoparticles is independent of the model used to represent the water molecules and of the presence of acid molecules. The absorption of oxygen into the subsurface occurs when the coverage of oxygen is greater than 0.5 ML in both systems, causing buckling of the outmost atoms of the nanoparticle, in agreement with DFT studies of O migration into the subsurface of alloys, where it was shown that such migration may become facilitated by the presence of less noble metals such as Co.[19,21] Water molecules are located around the nanoparticle at approximately 3 Å from the surface. In the alloy nanoparticle, the surface segregation of Co atoms takes place under all the studied coverages, the number of segregated Co atoms increases with the oxygen coverage, as it is shown in Table V-4.

Table V-4. Composition in atomic percent of the topmost layer of the oxidized Pt/PtCo/Pt3Co nanoparticle on C under different coverages of oxygen and water, and under pH = 3.

Coverage of O (ML)	Pt composition	Co composition	O composition
0.50	0.80	0.10	0.10
0.60	0.73	0.14	0.13
0.75	0.70	0.15	0.15
0.85	0.60	0.18	0.22

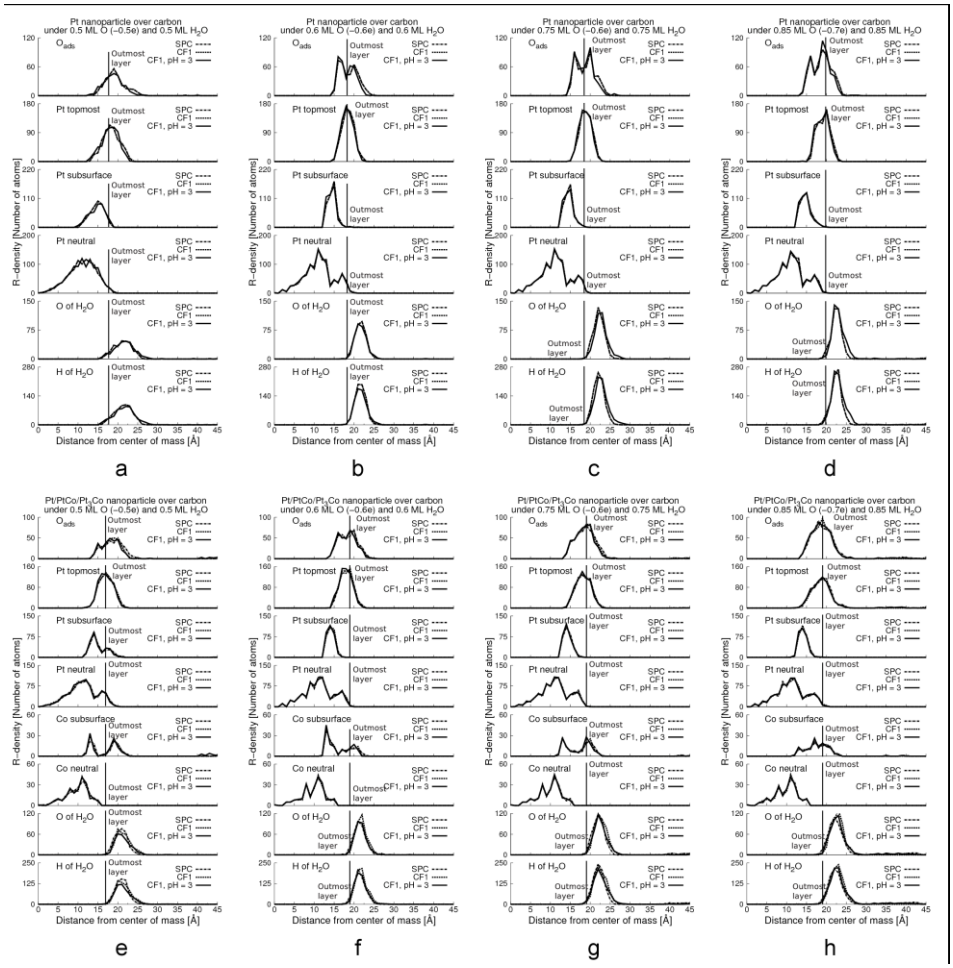

Figure V-2. R-density profiles of Pt (a-d) and Pt/PtCo/Pt3Co (e-h) supported nanoparticles over C under different coverages of oxygen and water, using the SPC/E and CF1 models to represent water molecules. The outmost layer (shown with a vertical line in each graph) is located at approximately at 17.5 Å from the center of mass of the nanoparticle under vacuum conditions.

Figure V-3 and Figure V-4 display snapshots of the surface oxidized pure Pt and Pt/PtCo/Pt_3Co nanoparticles on C at the end of the simulation using the CF1 model and under pH =3, and the final configuration of the system under vacuum. We observe that water molecules agglomerate on defined regions of the nanoparticle surface; the boundaries of such regions are the most active in terms of water dissociation. Water agglomerations have been detected experimentally on clean Pt(111) surfaces by Ogasawara et al.[125] through infrared absorption spectroscopy who reported that hydrogen bonding causes strong lateral interactions inducing the clustering of water molecules.

The dissociation of water involves mainly Pt atoms in the alloy nanoparticle and the OH radicals form hydrogen bonds with water molecules.

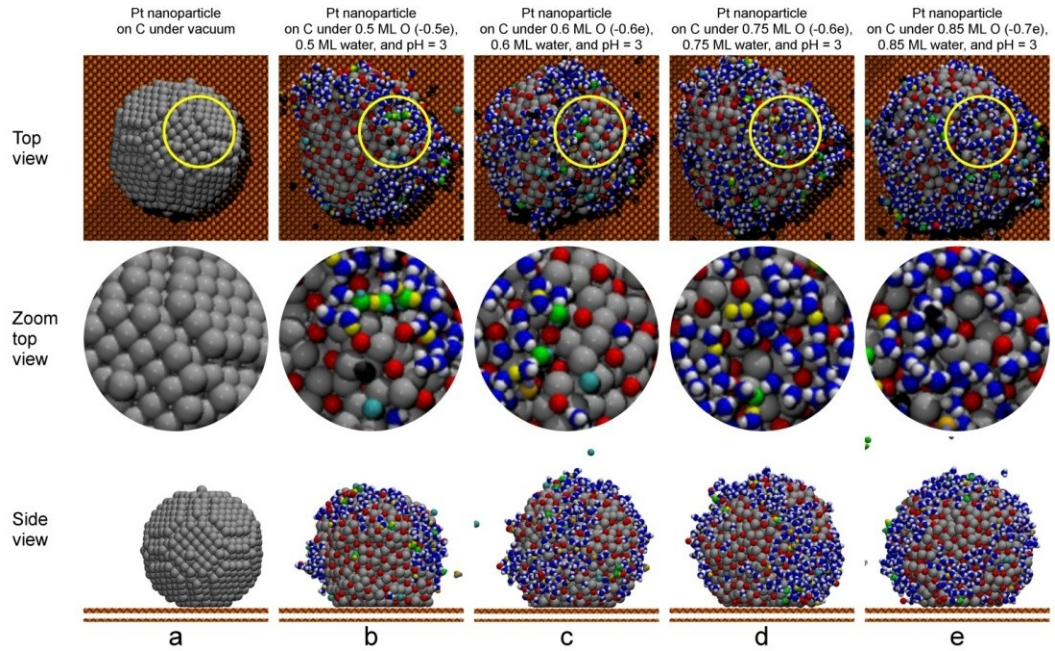

Figure V-3. Snapshots of the supported Pt nanoparticle on C under vacuum (a) and different coverages of oxygen and water (b-e) taken at the end of the simulation using the CF1 model and under pH =3. Color key: platinum-grey, oxygen-red, cation-yellow, OH-green, H2O-blue and white, H3O-orange and purple, anion-cyan, carbon-orange.

The shape of the nanoparticle changes dramatically as oxidation takes place due to the absorption of oxygen atoms, and Co segregation in the alloy system. The oxidized nanoparticles become practically spherical due to absorption of oxygen in the subsurface, their diameter increases with the coverage of oxygen but the core of the nanoparticle remains practically unaffected. Figure V-5 and Figure V-6 show the oxidized nanoparticles but all the adsorbates are hidden. Part of the (111) facets remain intact until the O coverage becomes higher than 0.5 ML when the oxygen atoms begin to migrate to the subsurface distorting the outmost layers due to buckling of metal atoms. In the alloy nanoparticle the segregation of Co atoms also affects the facets of the nanoparticle, generating a disordered outmost layer.

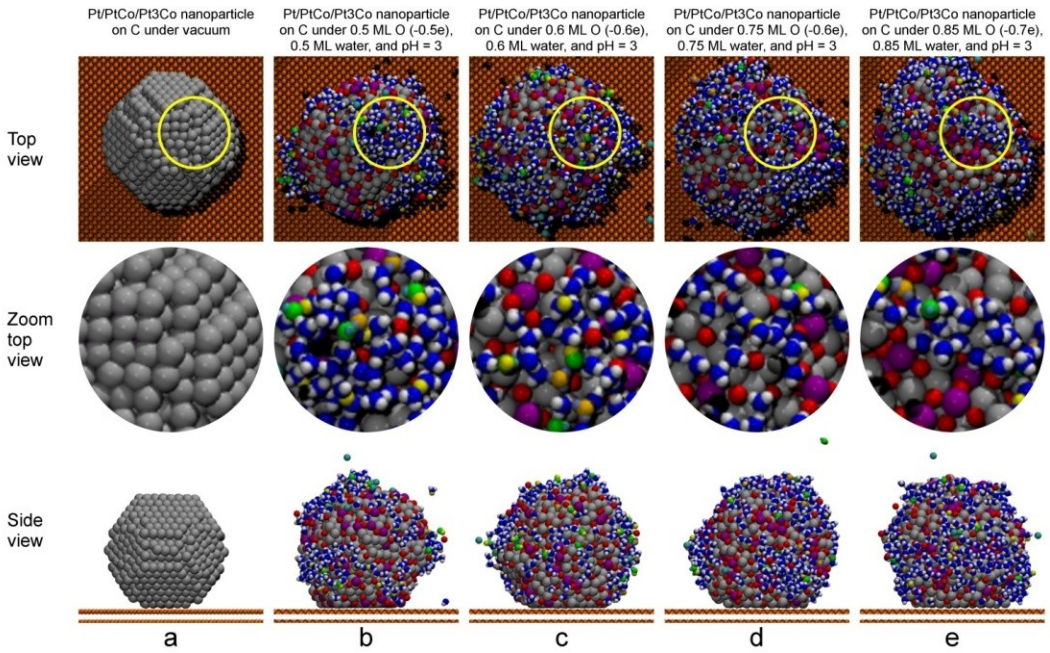

Figure V-4. Snapshots of the supported Pt/PtCo/Pt_3Co nanoparticle on C under vacuum (a) and different coverages of oxygen and water (b-e) taken at the end of the simulation using the CF1 model and under pH =3. Color key: platinum-grey, cobalt-purple, oxygen-red, cation-yellow, OH-green, H2O-blue and white, H3O-orange and purple, anion-cyan, carbon-orange.

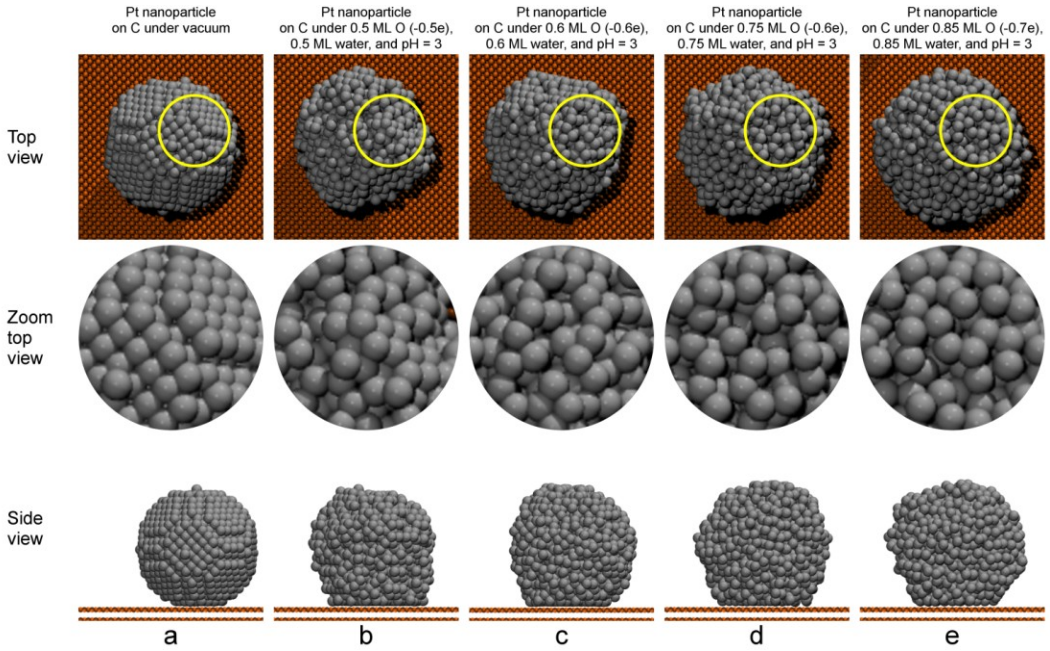

Figure V-5. Snapshots of the supported Pt nanoparticle on C under vacuum (a) and different coverages of oxygen and water (b-e) taken at the end of the simulation using the CF1 model and under pH =3. All the adsorbates are hidden to show the configuration of the metal atoms. Color key: platinum-grey, carbon-orange.

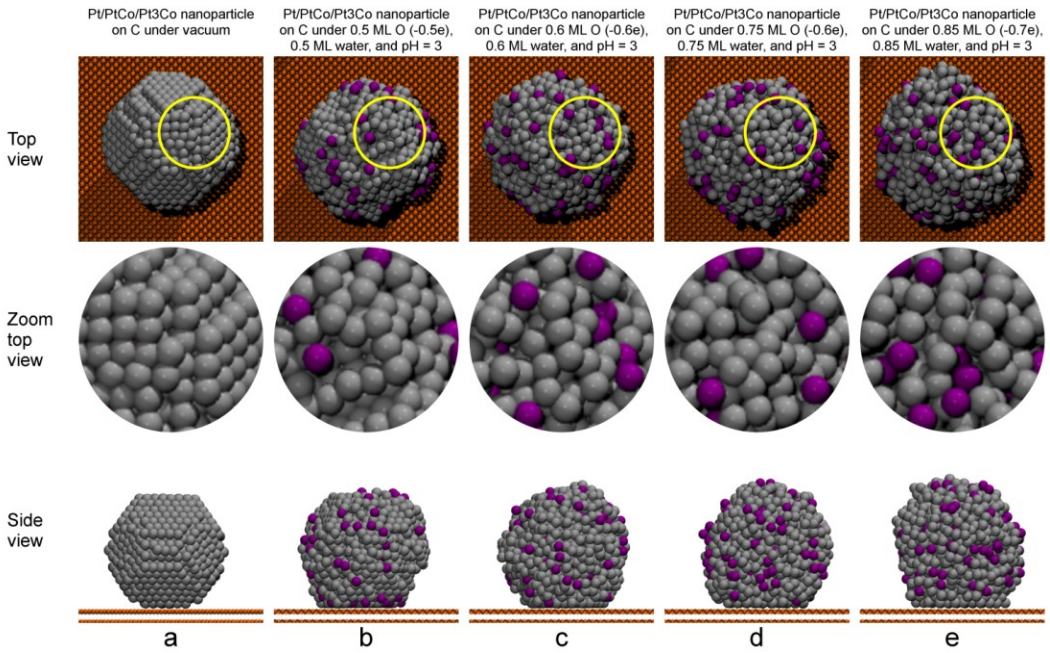

Figure V-6. Snapshots of the supported Pt/PtCo/Pt_3Co nanoparticle on C under vacuum (a) and different coverages of oxygen and water (b-e) taken at the end of the simulation using the CF1 model and under pH =3. All the adsorbates are hidden to show the configuration of the metal atoms. Color key: platinum-grey, cobalt-purple, carbon-orange.

Figure V-7 shows snapshots of regions within the supported alloy nanoparticle, is evident that oxygen atoms are absorbed in the subsurface for coverages greater than 0.60 ML, causing an increasing in the diameter of the nanoparticle (Figure V-7d) and forming an ordered structure facilitated by the presence of vacancies created by the surface segregation of Co atoms.

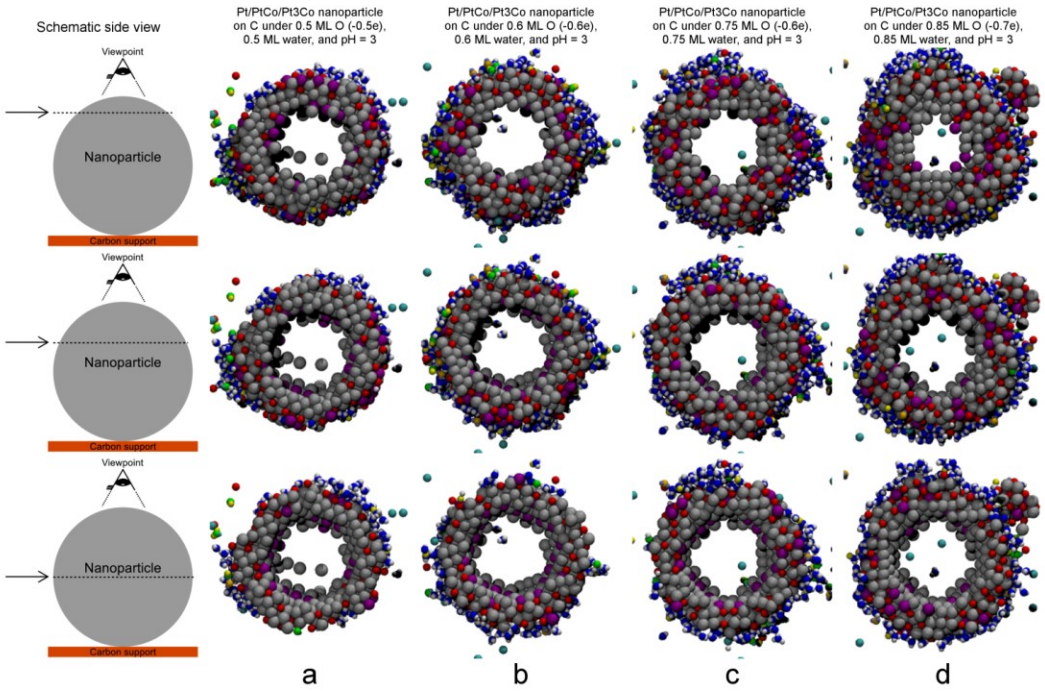

Figure V-7. Snapshots of regions within the supported Pt/PtCo/Pt_3Co nanoparticle on C under different coverages of oxygen and water taken at the end of the simulation using the CF1 model and under pH =3. Only the adsorbates and charged metal atoms are shown. Color key: platinum-grey, cobalt-purple, oxygen-red, cation-yellow, OH-green, H2O-blue and white, H3O-orange and purple, anion-cyan.

Our results indicate that water dissociation on the nanoparticle occurs only when acid is present, unlike the behavior observed in the (111) slab where we observed the formation of OH molecules from dissociation of water even when acid molecules are absent[25]. This is an evidence of the importance of the shape of the catalyst in the ORR kinetics. On the (111) surface, water dissociates in regions having buckled atoms in which the oxygen atoms have not formed an ordered structure in the subsurface as it occurs for the highest oxygen coverage. The acid does not modify the relaxed structure of the surface. However, the dissociated ions enhance the breaking of OH bonds of water molecules due to electrostatic interactions.

The number of adsorbates on the Pt and Pt/PtCo/Pt_3Co supported nanoparticles are reported in Table V-5 and Table V-6. Water dissociation in the Pt/PtCo/Pt_3Co nanoparticle surface is higher in all cases than in pure Pt nanoparticle, indicating a more active catalyst in the framework of our model, in agreement with several experimental reports.[6,13,124] All the acid molecules are dissociated in agreement with experimental and

theoretical reports.[122] The amount of OH molecules decreases with oxygen coverage in the Pt nanoparticle from 0.030 ML to 0.024 ML for oxygen coverages of 0.5 ML and 0.85 ML, respectively. Whereas in the alloy nanoparticle the OH coverage increases with the amount of oxygen in the simulation from 0.033 ML for 0.50 ML of O to 0.042 ML for 0.85 ML of O, supporting the conclusion that the alloy nanoparticle is more active (i.e. favoring an enhanced water dissociation) than the pure Pt one. We observe the presence of H_3O intermediates in all cases in both systems; their amount is lower than the number of OH molecules in all the studied cases.

Table V-5. Number of adsorbates on Pt supported nanoparticle under pH = 3

	0.50 ML O	0.60 ML O	0.75 ML O	0.85 ML O
H	83 (0.125 ML)	75 (0.13 ML)	79 (0.119 ML)	79 (0.119 ML)
OH	20 (0.030 ML)	19 (0.029 ML)	17 (0.026 ML)	16 (0.024 ML)
H3O	8 (0.012 ML)	13 (0.020 ML)	7 (0.011 ML)	6 (0.009 ML)
Dissociated H_2O	30 (9.0%)	33 (8.27%)	25 (5.0%)	23 (4.0%)

Table V-6. Number of adsorbates on Pt/PtCo/Pt_3Co supported nanoparticle under pH = 3

	0.50 ML O	0.60 ML O	0.75 ML O	0.85 ML O
H	82 (0.123 ML)	90 (0.135 ML)	84 (0.126 ML)	95 (0.143 ML)
OH	22 (0.033 ML)	28 (0.042 ML)	25 (0.038 ML)	28 (0.042 ML)
H3O	9 (0.014 ML)	17 (0.026 ML)	10 (0.015 ML)	26 (0.039 ML)
Dissociated H2O	32 (9.6%)	51 (12.8%)	36 (7.2%)	67 (11.8%)

V.3.2 Reduction-oxidation cycles

In order to emulate a cyclic voltammetry experiment we exposed the supported nanoparticle to simulated cycles of reduction and oxidation, in which the charges of the oxygen and metal atoms forming the outmost layers of the nanoparticle under 0.85 ML of oxygen were gradually decreased (reduction steps). Once neutrality was attained, the charges were steadily increased until recovering their original values (oxidation steps).

The R-density profiles and snapshots of the surface of both studied systems after one and ten cycles are shown in Figure V-8 and Figure V-9. The R-density profiles in Figure V-8 indicate that oxygen absorbs deeper in the subsurface as the cycling process occurs in the pure platinum nanoparticle, whereas in the alloy nanoparticle Co atoms migrate from the subsurface to the outmost layers. Note that the presence of species located at distances greater than ~25 Å in Figure V-8 may be regarded as detached from the nanoparticle as a consequence of the degradation process. This causes an apparent broadening of the oxygen absorption towards the surface of the nanoparticle but such oxygen atoms are bonded to detached metal atoms, not adsorbed on the nanoparticle surface. After ten cycles of reduction and oxidation it is observed metal dissolution of atoms forming the outer layers in both systems (Figure V-9a-c and Figure V-9e-g), the estimated decreasing in surface area compared to the area of the nanoparticle under vacuum is presented in Table V-7 and Table V-8. There is a greater loss in surface area of the alloy nanoparticle compared to the one found in the pure Pt system. After the first cycle the ratio of Co atoms to Pt atoms that are detached is approximately 2:1. However, after ten cycles such ratio reverses to 1:4, this implies that the segregated Co atoms dissolve before the Pt atoms which detach after most of the Co atoms near to the surface are dissolved. These findings are in agreement with several experimental reports showing the instability towards dissolution of Pt_3Co nanoparticles after operating cycles[13,132,133]. The dissolution process occurs mainly when the magnitude of the charge of the oxygen atoms is higher than -0.4e (on the reduction branch), the detached metal atoms agglomerate far from the nanoparticle. Interestingly, we found that the dissolution process takes place only when acid molecules are present. The role of the dissociated ions is destabilizing the metal oxide layers due to electrostatic interactions causing the detachment of single metal atoms bonded typically to one or two oxygen atoms. The facets of the nanoparticle are partially recovered when the charge of oxygen atoms is 0.0e, although steps and kinks in the outmost layers are permanent. Water molecules agglomerate in defined regions of the nanoparticle. This behavior is more evident after ten cycles of reduction and oxidation.

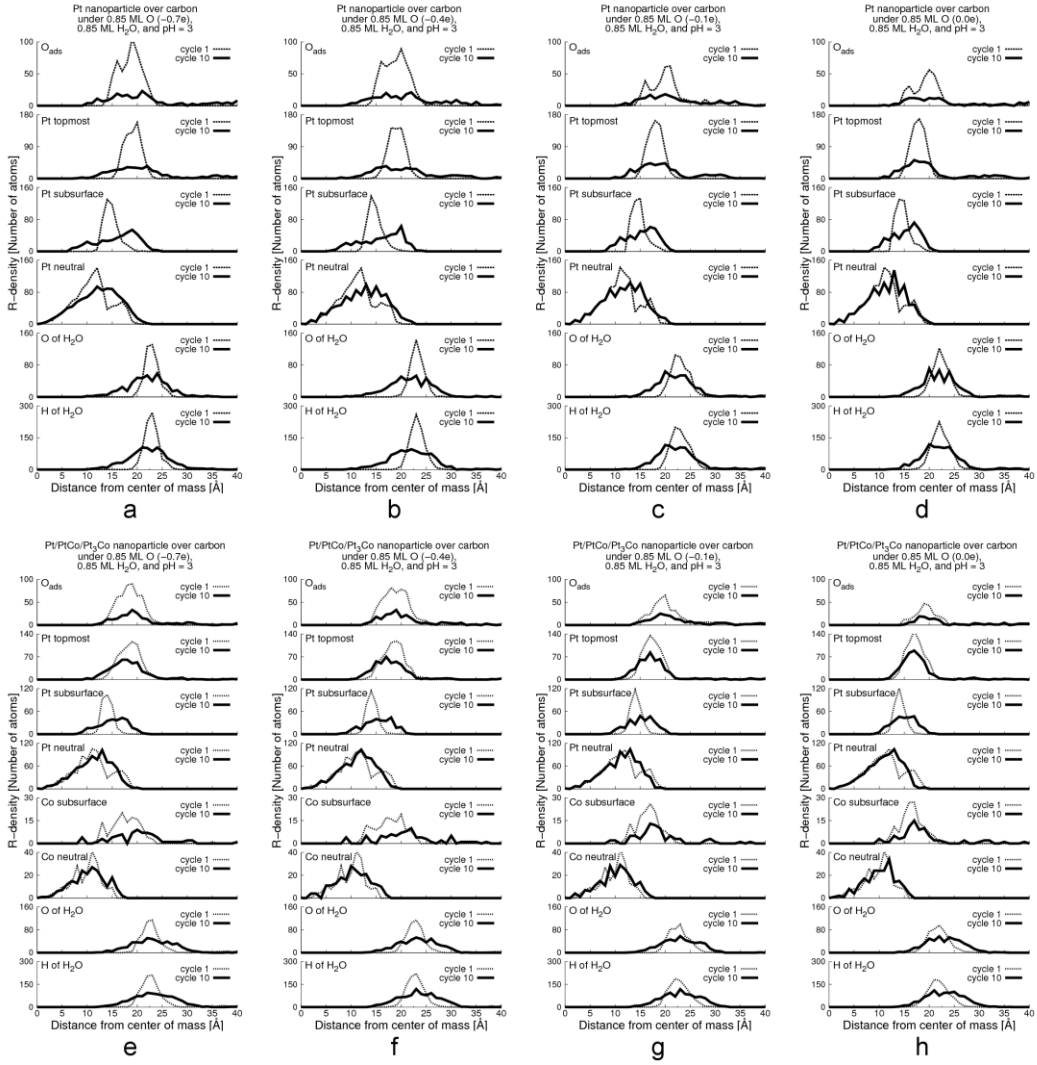

Figure V-8. R-density profiles of Pt (a-d) and Pt/PtCo/Pt_3Co (e-h) supported nanoparticles over C under 0.85 ML of oxygen and water, and pH = 3 after 1 and 10 reduction-oxidation cycles.

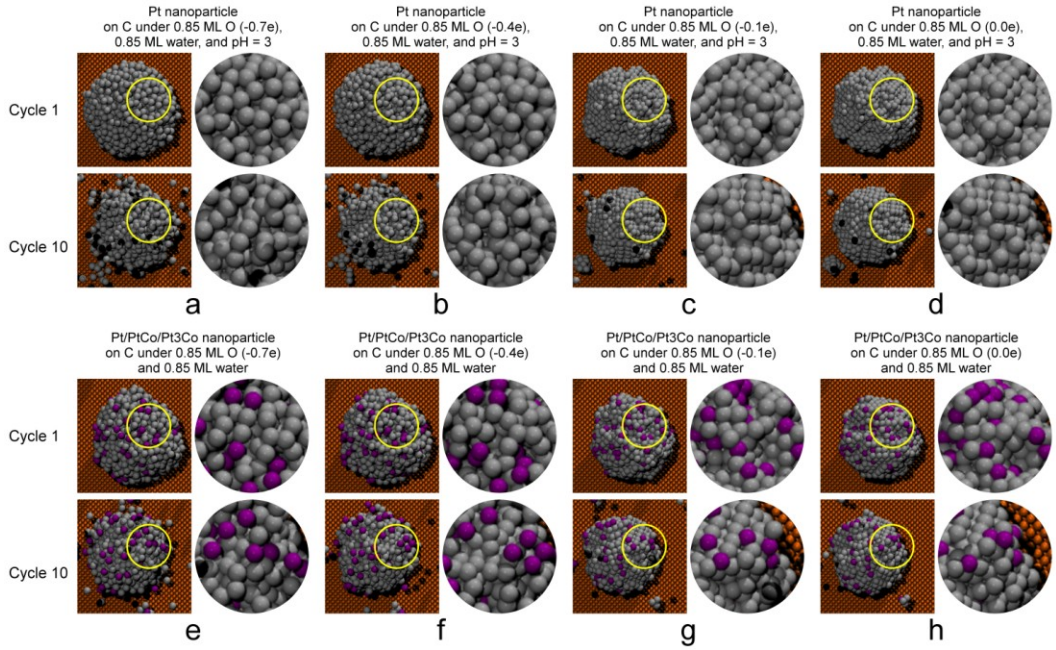

Figure V-9. Snapshots of the supported Pt(a-d) and Pt/PtCo/Pt_3Co(e-h) nanoparticles on C under 0.85 ML of oxygen and water, and pH = 3 taken at the end of the simulation after 1 and 10 reduction-oxidation cycles. All the adsorbates are hidden. Color key: platinum-grey, cobalt-purple, carbon-orange.

Table V-7. Detached Pt atoms and estimated surface area of the supported Pt nanoparticle after reduction-oxidation cycles.

	Cycle 1	Cycle 10
Detached Pt atoms	4	36
Area/Area vacuum	99.02%	90.44%

Table V-8. Detached metal atoms and estimated surface area of the supported Pt/PtCo/Pt_3Co nanoparticle after reduction-oxidation cycles.

	Cycle 1	Cycle 10
Detached Pt atoms	4	36
Detached Co atoms	8	10
Area/Area vacuum	94.26%	86.87%

CHAPTER VI
EFFECT OF SUBSURFACE VACANCIES ON OXYGEN REDUCTION REACTION ACTIVITY OF PT-BASED ALLOYS*

VI.1 Motivation

The electrocatalysis of the ORR is carried out on nanoparticles with the goal of employing the smallest amount of material that is able of maximizing the catalytic activity and stability. Pt-based alloy catalysts reduce the required amount of platinum and some of them have shown enhanced ORR activity compared to pure Pt catalysts, specifically the Pt_3Co alloy[2-4] and recently core-shell catalysts consisting of a Pt monolayer shell over cores made of porous/hollow Pd—Cu alloy,[5] acid treated Pt_3Co alloy,[2,6,7] or dealloyed $PtCu_3$[8,9] have demonstrated remarkable activity.

In the case of the Pt_3Co alloy, the enhanced activity is partially attributed to the formation of a "Pt-skin" structure produced by an exchange of Pt and Co in the first two layers,[3] denoted in this work as $Pt/PtCo/Pt_3Co$. Despite of its enhanced activity, the Pt_3Co catalysts exhibit Co dissolution during the fuel cell operation, decreasing their activity.[13] The dissolution process may involve interactions between the topmost layers of the catalyst, atomic oxygen, oxygenated species, and the electrolyte. The existence of a correlation between the onset of the oxide formation and the concentration of dissolved Pt has been found experimentally.[15] However, the actual mechanism of the dissolution process and particularly its effects on the catalyst structure are not well understood. We recently used a two-stage simulation approach combining density functional theory (DFT) and molecular dynamics (MD) to get insights at the molecular level of the oxidation and metal dissolution effects on degradation of ORR catalysts.[23-25] In agreement with experimental reports,[134] we found that the dissolution mechanism involves migration of less-noble subsurface atoms to the surface along with significant surface reconstruction which leads to dissolution of oxidized surface atoms. As a result

---

of dealloying, a porous matrix structure is expected to arise under certain conditions.[29,31,135] Experimental studies report the formation of hollow structures and porous walls,[26] and computational studies have assessed the lattice contraction effect due to the presence of a hollow structure inside a nanoparticle as a main factor for enhanced activity.[27] These analyses assume that the exterior shell is a perfect lattice. In contrast, we hypothesize that the structure after dissolution/dealloying may contain significant number of defects. Our model includes the presence of vacancies right below the top monolayer, representing defects that would be inherently associated with the dealloying process. Such defective structure may exert additional influence on the surface catalytic activity. Thus, we focus on the role of vacancies in the catalytic subsurface in relation to the enhancement of their reported ORR activity.[2,5-9] Given the success of DFT on describing adsorption and reaction on catalytic surfaces,[38,40,44-52,136] we examine the effect of the presence of vacancies in the subsurface on the ORR activity of the catalyst, computing specific descriptors such as the binding energies of O and OH.[136,137]

VI.2 Computational details

In a first approximation, we model the porous structure of the catalytic nanoparticle using a 2 × 2 simulation cell of 5 layers with (111) orientation in which atoms from the subsurface (second layer) were removed to create vacancies. A schematic representation of the connection between the DFT simulation cell and the catalytic alloy nanoparticle is shown in Figure VI-1.

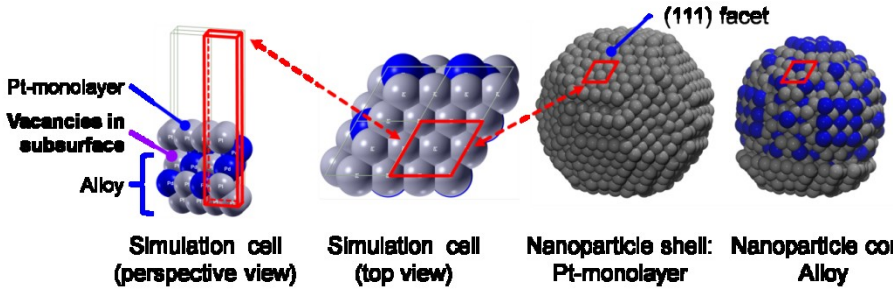

Figure VI-1.Schematic representation of the connection between the DFT simulation cell and the catalytic alloy nanoparticle.

Calculations were done with different number of layers in the slab to verify this effect on the binding energies of O and OH. The size of the adopted system was determined by the computational cost of the DFT calculations; the system size was chosen to be the smallest one able to produce results practically independent of the number of layers in the slab. We performed DFT calculations involving the adsorption of an oxygen atom and an OH molecule separately using the simulation cells shown in Figure VI-2. Since these adsorbates are present in the rate limiting steps of most accepted mechanisms of the ORR,[138] their binding energies are good descriptors of the activity of catalytic surfaces.[139] A number of atoms of the layer right below the Pt-monolayer were removed to create different amount of vacancies in the subsurface (0.25, 0.50, and 0.75 ML of vacancies). We focused on bimetallic cores of Pt-based (Figure VI-2a) and Pd-Cu alloys (Figure VI-2b), the studied systems and their corresponding calculated lattice constants are reported in Table VI-1. In all cases the lattice constant of the alloy cores is smaller than the lattice constant of bulk Pt, causing a reduction on the Pt—Pt distance of the Pt-monolayer which has been associated with weaker binding energies of O[63], therefore an enhanced activity for the ORR is expected.

The DFT calculations were performed using the Vienna Ab-initio Simulation Package (VASP).[54-58] In VASP the Kohn–Sham equations are solved by self-consistent algorithms. In order to improve the calculation efficiency, core electrons were replaced by the projector augmented wave (PAW) pseudo–potentials[59,60] and the valence electrons were described by plane wave basis sets. In this work, the plane wave was expanded up to a cutoff energy of 380 eV. Brillouin zone integration was made in an 8 × 8 × 1 Monkhorst–Pack k-point mesh.[140] The exchange-correlation functional was described within the generalized gradient approximation (GGA) proposed by Perdew, Burke and Ernzerhof (PBE).[61] Spin polarization was taken into account in the calculations and the Methfessel–Paxton method[141] was employed to determine electron occupancies with a smearing parameter σ of 0.2 eV. The convergence criteria for the electronic self-consistent iteration and the ionic relaxation loop were set to 10^{-4} eV and 10^{-3} eV, respectively.

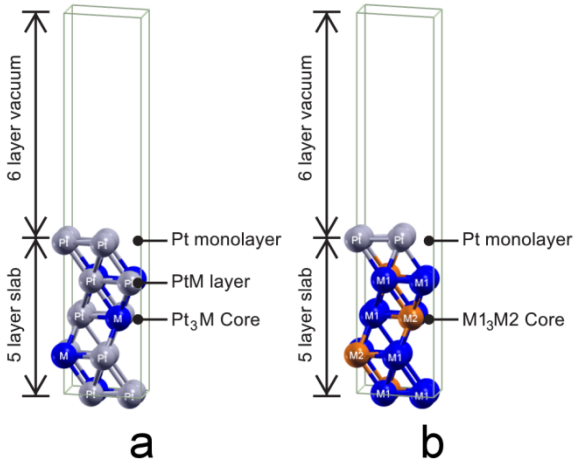

Figure VI-2. Simulation cells for DFT calculations. (a) Binary alloy systems Pt/PtM/Pt_3M (M=Co, Pd, Ir, Cu) and (b) ternary alloy systems, Pt/$M1_3M2$ (M1, M2 = Pd, Cu; M1≠M2). A number of atoms of the layer right below the Pt-monolayer were removed to create different amount of vacancies in the subsurface (0.25, 0.50, and 0.75 ML of vacancies).

Table VI-1. Calculated lattice constant and Pt—Pt nearest neighbor distances of the studied systems.

System	Lattice constant, a [Å]	Nearest neighbor distance [Å]	$(a - a_{Pt})/a_{Pt}$
Pt	3.98	2.81	0.0%
Pt/PtCo/Pt_3Co	3.89	2.75	-2.3%
Pt/PtPd/Pt_3Pd	3.97	2.81	-0.3%
Pt/PtIr/Pt_3Ir	3.95	2.79	-0.8%
Pt/PtCu/Pt_3Cu	3.90	2.76	-2.0%
Pt/Pd_3Cu	3.89	2.75	-2.3%
Pt/$PdCu_3$	3.73	2.64	-6.3%

VI.3 Results and discussion

The adsorption energy of atomic oxygen in the studied systems under 0.25 ML coverage as a function of the amount of vacancies in the subsurface is shown in Figure VI-3a. In the absence of vacancies, all of the alloy systems exhibit weaker or comparable oxygen binding energies than those on pure Pt. For pure Pt, there is a slight decrease of the O binding energy as the number of vacancies in the subsurface increases, until a concentration of vacancies of 0.5 ML, followed by an increase at higher vacancy concentrations. Similar behavior is followed by the Pt/PtPd/Pt_3Pd and Pt/PtIr/Pt_3Ir alloys. In most of the other alloys studied here, the O binding energy increases steadily

as the number of vacancies in the subsurface increases. Interestingly, the oxygen adsorption energies for several of the systems converge to similar values, between -4.0 eV and -4.6 eV, when there is 0.50 ML of vacancies in the subsurface. This could indicate a trend towards a similar behavior which does not depend much on the core content, except when the core is dominated by small size elements such as Co or Cu.

The *d*-band center relative to the energy of the Fermi level (in eV) has been used to correlate the electronic structure of Pt and Pt-3*d* metal alloys with their chemical activity.[142,143] The effect of the presence of vacancies in the subsurface on the *d*-band center of the Pt-monolayer of the surfaces under 0.25 ML of oxygen is shown in Figure VI-3b. Practically in all cases the d-band center shifts towards the Fermi level when the amount of vacancies in the second layer increases. This trend in the d-band center is an indicator of higher surface reactivity; however the changes in oxygen adsorption energy are not that pronounced even in the cases of Pt/Pd_3Cu and $Pt/PtCu/Pt_3Cu$ which show the largest changes in *d*-band center. On the other hand, the adsorption energy of OH decreases for most of the surfaces as the amount of vacancies in the subsurface increases, as it is depicted in Figure VI-3c. The decrease of the OH binding strength is favorable for ORR activity, because OH is a poison that tends to cover the surface becoming an obstacle for the continuation of the main reaction. Thus, the effect of the subsurface vacancies on the adsorption energies of O and OH suggests an overall favorable effect on the ORR, and possibly the existence of an optimum amount of vacancies beneath the Pt-monolayer that maximizes the ORR activity.

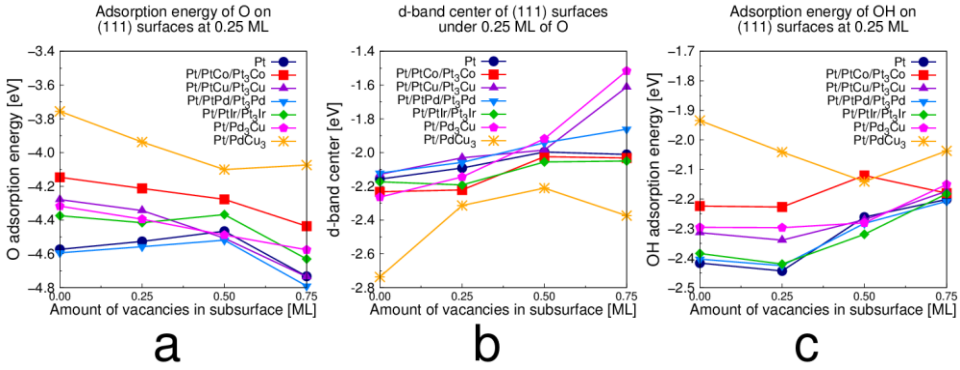

Figure VI-3. Adsorption energy of oxygen (a) and d-band center of topmost Pt atoms (b) on (111) surfaces under 0.25 ML of oxygen. Adsorption energies of OH on (111) surfaces under 0.25 ML coverage.

To find out the relationship between the effects on the O and OH adsorption energies, Figure VI-4 displays the adsorption energy of OH for the studied systems as a function of the adsorption energy of O at constant amount of vacancies in the second layer of the studied surfaces. In absence of vacancies (Figure VI-4a), there is a clear linear behavior of the binding energy of OH revealing a correlation between adsorption of the two species in response to changes in the core electronic structure. This linearity is maintained when vacancies are present in the subsurface; however, the slope first increases slightly, denoting the larger decrease of the OH binding strength in relation to the O adsorption strength for 0.25 ML of vacancies. As the number of vacancies in the subsurface increases (Figure VI-4b, c, and d), the slope decreases showing that the binding energy of OH is less sensitive to changes in the structure of the subsurface than the adsorption energy of O. Interestingly, most of the alloy systems converge to similar binding energies to pure Pt when there is 0.50 ML of vacancies in the subsurface (Figure VI-4c),this implies that under these conditions the alloy surfaces may exhibit catalytic properties similar to those of pure platinum (or Pt-rich alloy) surfaces.

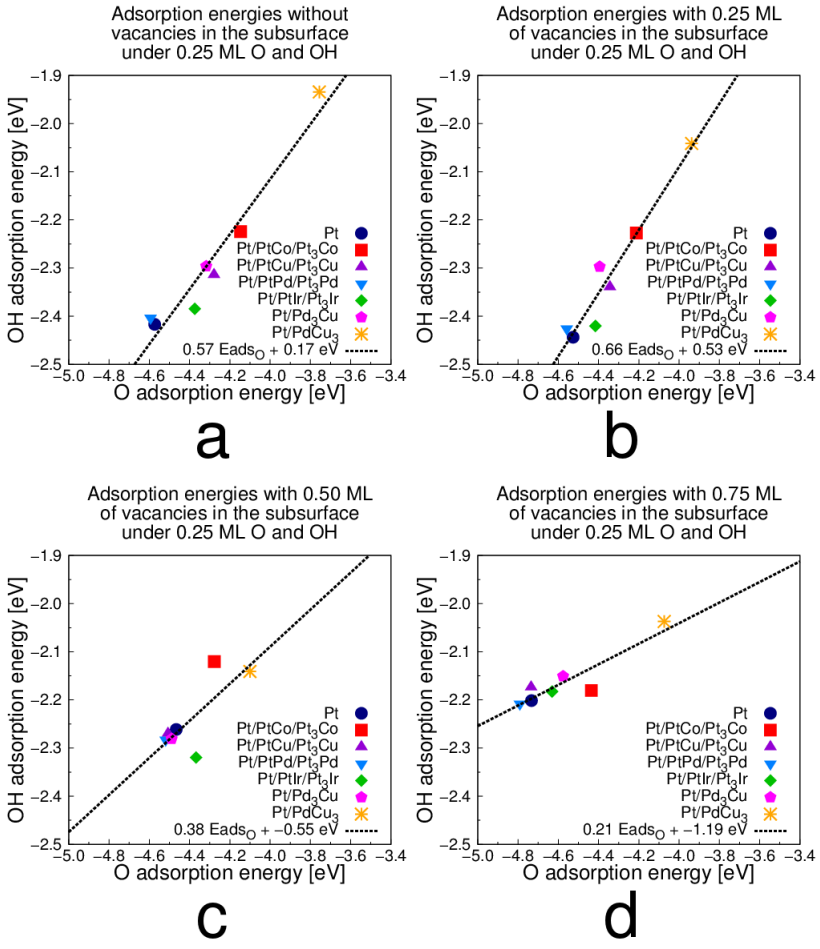

Figure VI-4. Adsorption energy of OH at 0.25 ML as a function of the adsorption energy of O at 0.25 ML on (111) surfaces with vacancy different amount of vacancies in the second layer: (a) No vacancies, (b) 0.25 ML, (c) 0.50 ML, and (d) 0.75 ML.

Good ORR catalysts exhibit relatively low binding energies for oxygen and OH, strong enough to enable the surface to dissociate the O_2 molecule and weak enough to allow the subsequent proton and electron transfer reduction steps that yield H_2O.[138,144] From the above results, the presence of vacancies in the subsurface keep relatively low O binding energies and shift the behavior of most of the systems towards the region of lower binding energies of OH. However, there is an optimum amount of subsurface vacancies, between 0.25 ML and 0.75 ML that weakens the adsorption energies of O and OH, as it can be inferred from Figure VI-3 and Figure VI-4. Moreover, it is observed that the Pt/PtCo/Pt_3Co and Pt/$PdCu_3$systems exhibit low binding energies for both,

atomic oxygen and OH, this behavior makes these alloys interesting candidates to replace pure platinum based on their better ORR activity. These results are in agreement with experimental reports of nanoparticles with a Pt-monolayer on Pd—Cu alloy cores showing 14 times higher Pt mass activity than pure Pt nanoparticles,[5] and acid treated Pt_3Co[2,6,7] alloy nanoparticles with 4 times the ORR activity of their pure Pt counterparts.

The present calculations do not incorporate the effect of an electrochemical potential. However, as shown in previous studies by Norskov et al.[138] a very reasonable assumption introduces the electrochemical potential as an additional term to the free energy of the reaction, while keeping constant the binding energies of the ORR intermediates. Thus, within this assumption, the electrochemical potential modifies the activation barriers much more than the adsorption energies. On the other hand, the electric field created by variation of the electrochemical potential may affect adsorbates that have a dipole (as OH) or higher order multipoles as observed by XPS[17] and EXAFS[78] measurements. Although the change of orientation of the OH dipole due to subsurface vacancies was discussed in Figure VI-7, additional orientational changes due to an electric field that could modify slightly the OH adsorption energies have not been analyzed in this study.

We also examined the effects of the subsurface vacancies on the adsorption energies at higher O coverage, the behavior found is similar to those reported in Figure VI-3a. The effect of the presence of vacancies in the subsurface is also reflected on the geometry of the surface and subsurface layers. The Pt—Pt nearest neighbor distance of the Pt-monolayer of the systems under 0.25 ML of O for different amount of vacancies in the subsurface of the studied systems is shown in Figure VI-5a. There is a decrease in the Pt—Pt distance caused by the subsurface vacancies, a reduction on such distance has been associated to enhanced ORR activity,[145] this fact supports the discussion presented above from which it may be concluded that a certain amount of subsurface vacancies may enhance the ORR activity through a reduction of the binding energies of reaction intermediates. In contrast, the metal—metal nearest neighbor distance within the

subsurface layer is almost unaffected by the presence of the vacancies as it is observed in Figure VI-5b.

The interlayer distances involving the topmost, second and third layers decrease with the presence of subsurface vacancies in most of the systems as it is shown in Figure VI-5c and Figure VI-5d. The overall effect of subsurface vacancies is a change in the metal—metal distances and reduction of the coordination number of some surface atoms of the slab that enhances the ORR activity by influencing the electronic structure as illustrated in Figure VI-3b.

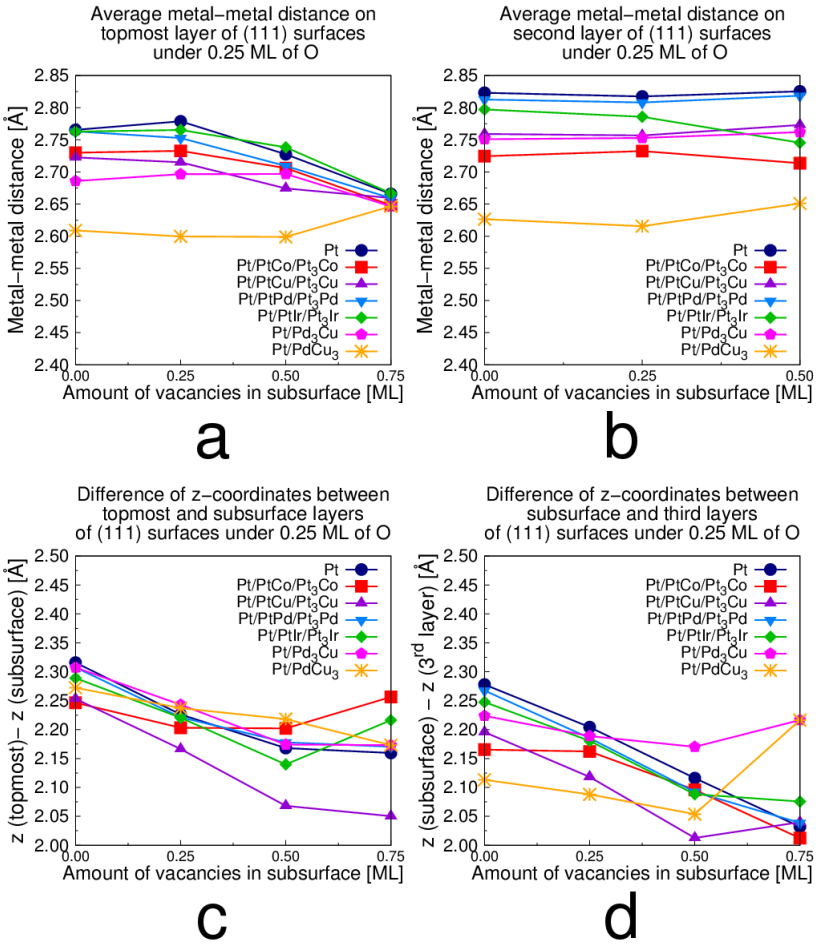

Figure VI-5. Average metal—metal distances and difference in z-coordinates. Pt—Pt nearest neighbor distance in topmost layer (a), metal—metal nearest neighbor distance in subsurface (b), interlayer distance between topmost and second layers (c), interlayer distance between second and third layers (d) of systems under 0.25 ML coverage of O and different amount of vacancies in the subsurface.

The most energetically favorable sites for the adsorption of atomic oxygen are the hollow sites of the (111) surface (involving three platinum nearest neighbors), whereas OH preferably adsorbs atop Pt atoms. The average O—Pt bond and OH—Pt bond as functions of the amount of vacancies of the subsurface on the studied systems are shown in Figure VI-6. For both adsorbates the bond distances to Pt atoms are practically unaffected by the amount of subsurface vacancies, there is a slight decrease in the O—Pt bond with the increase in the amount of vacancies in the subsurface which may be explained by a contraction in the Pt—Pt distance of the topmost layer as discussed above. The distance between the H atom of the adsorbed OH molecule and the closest Pt atom and the corresponding H—O—Pt angle as functions of the amount of subsurface vacancies are shown in Figure VI-7. For all the studied systems the orientation of the OH molecule on the surface does not change considerably with the presence of subsurface vacancies.

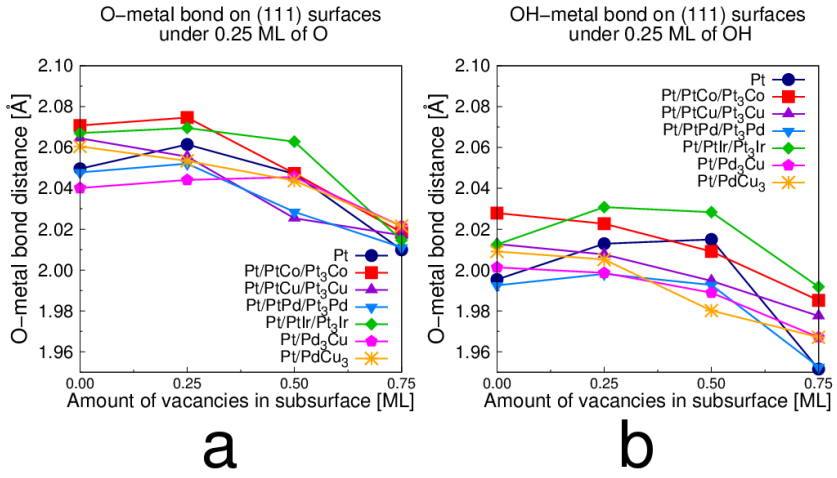

Figure VI-6. Average O—Pt bond distance (a) and OH—Pt bond distance (b) under 0.25 ML coverage and different amount of subsurface vacancies.

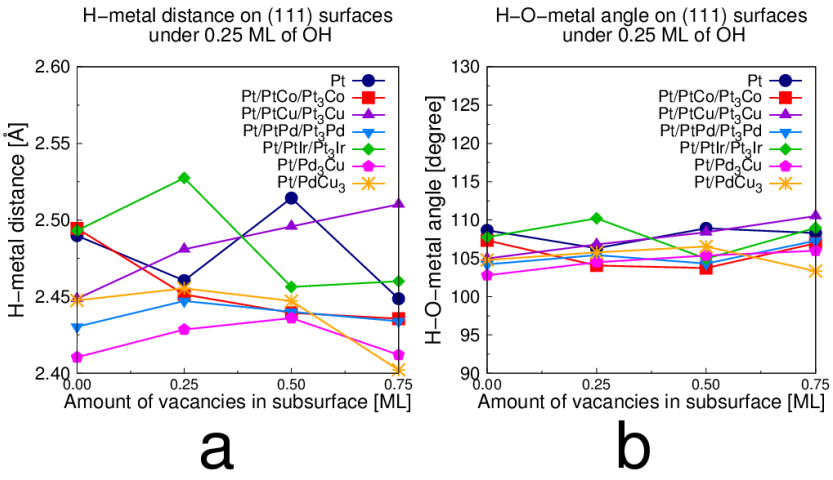

Figure VI-7. Minimum H—Pt distance (a) and H—O—Pt angle (b) under 0.25 ML coverage and different amount of subsurface vacancies.

Contour graphs (Figure VI-8) illustrate the effects of surface oxidation and subsurface vacancies on the reactivity (given by the O adsorption energies) as a function of the lattice parameters of the various alloys in this study. It is observed that the O atoms bind weaker to the surface of the studied systems with the smallest lattice parameters, in agreement with the correlations between lattice strain and reactivity discussed in the literature.[137] Moreover, it is demonstrated that the amount of vacancies in the subsurface of the system influences also the lattice parameter, thus having a direct effect on the ORR mechanism.

It is worth mentioning that surface reconstruction is not observed under any conditions for the studied systems, as it is demonstrated in the selected optimized structures of Pt, Pt/PtCo/Pt_3Co, and Pt/$PdCu_3$ under 0.25 ML O and 0.50 and 0.75 ML of subsurface vacancies in Figure VI-9. However, the strong lattice contraction caused by the $PdCu_3$ core with respect to the pure Pt surface in absence of subsurface vacancies (-6.3% in Table 1) is responsible of its different structure shown in Figure VI-9.

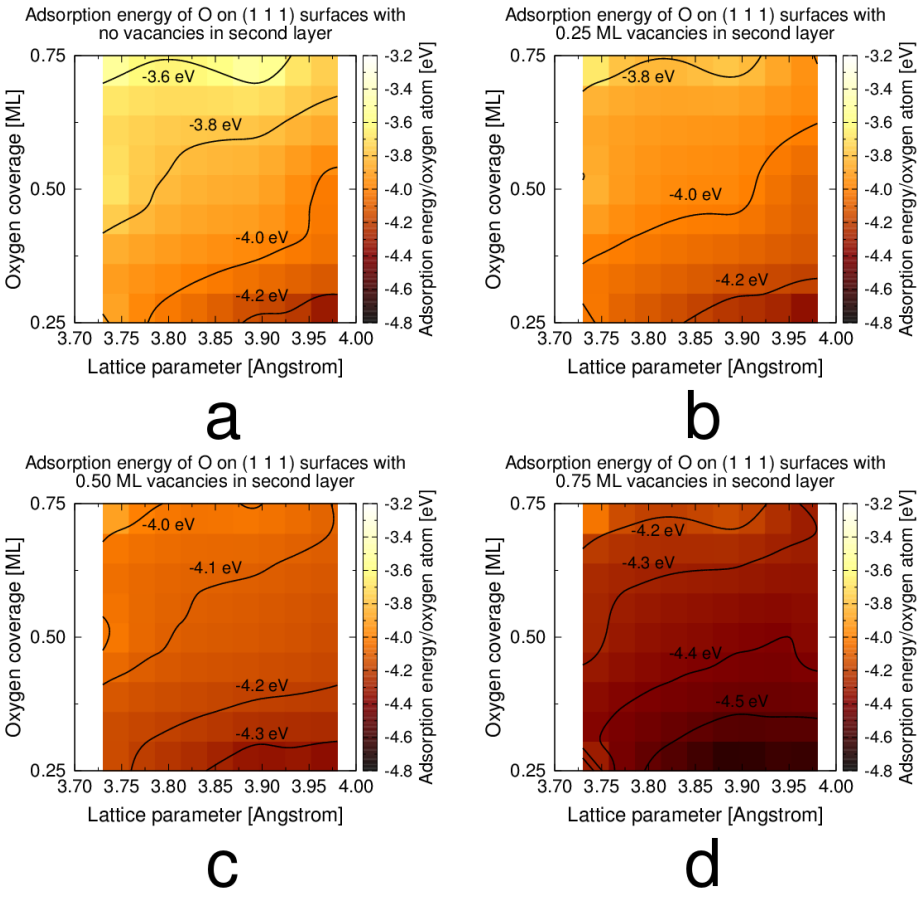

Figure VI-8. Contour graphs reflecting the combined effect of surface oxidation and subsurface vacancies on the oxygen adsorption energies and lattice parameters corresponding to the various alloys in this study.

When vacancies in the subsurface and surface coverages greater than 0.25 ML of O are considered, the geometry of the Pt monolayer is much different to the one observed in the other systems (see Figure VI-9, more evident for 0.75 ML due to absorption of O in the subsurface). The combination of a large lattice contraction due to alloying and subsurface vacancies and the interactions with adsorbates cause the peculiar behavior of this system.

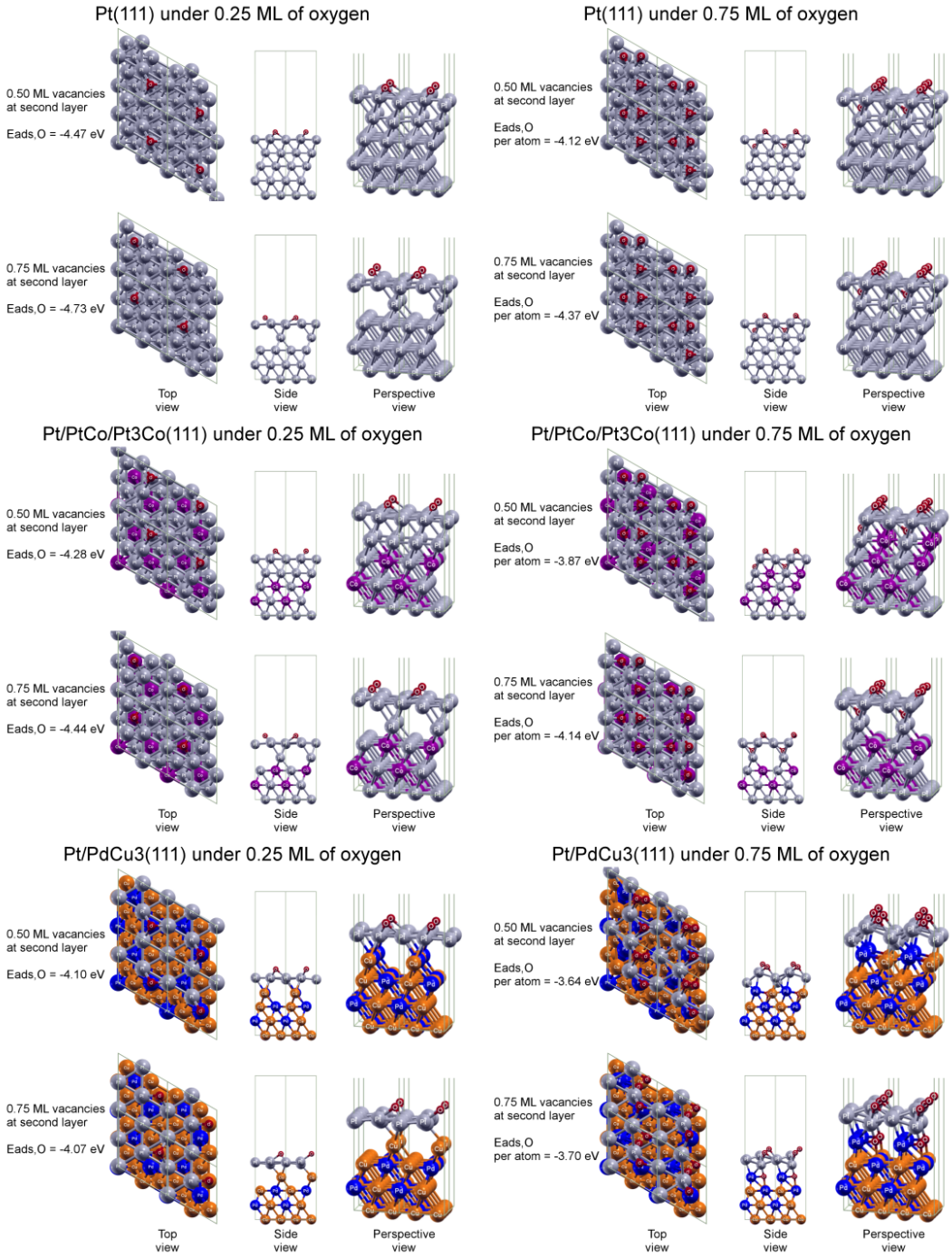

Figure VI-9. Selected optimized structures. Pt (top), Pt/PtCo/Pt_3Co (middle), and Pt/$PdCu_3$ (bottom) under 0.25 ML O and 0.75 ML of oxygen, and 0.50 and 0.75 ML of subsurface vacancies for each case.

CHAPTER VII
KINETIC MONTE CARLO SIMULATIONS OF DEALLOYING PLATINUM-BASED ALLOY CATALYSTS FOR FUEL CELLS

VII.1 Motivation

Dealloying is the selective removal of elements from an alloy. According to recent experimental reports dealloying taking place during the synthesis of ORR catalysts may yield to remarkable activity enhancement by creating characteristic porous or hollow structures. However, the dealloying process that occurs during the fuel cell operation is enhanced by the concomitant presence of oxygen that promotes metal dissolution causes the degradation of the catalyst. We study the driving forces and the effect of dealloying on the structure of alloy nanocatalysts during their synthesis and operation with a multi-scale approach involving kinetic Monte Carlo (KMC) simulations and density functional theory (DFT). The KMC method allows simulating the dynamic evolution of a catalyst in a long time scale, comparable to experiments. The required information for the method is the correct representation of all the relevant processes in the system in the form of rate expressions, the processes are selected based on the magnitude of their rate combined with a random approach. The atoms or species involved in the processes typically occupy sites in 2-D a lattice. However, a main contribution of this work is the development of a 3-D simulation code to study the degradation and dealloying processes in ORR catalysts.

Two cases of study are reported here, the degradation of nanoparticles under different electrochemical potential regimes and the synthesis of highly active hollow nanoparticles by removing the alloy core through dealloying using the Kirkendall effect. Both cases are relevant for the improvement of state-of-the-art ORR catalysts.

VII.2 Computational details

The initial configuration of the system in the KMC model consists of a nanoparticle with 40 Å radius and FCC structure surrounded by electrolyte as is presented in Figure VII-1. For the simulations of degradation under operation a pure Pt

nanoparticle was considered, whereas for the Kirkendall effect simulations (Figure VII-1b) either pure or bi-metallic core/shell systems with and without vacancies in the shell were considered.

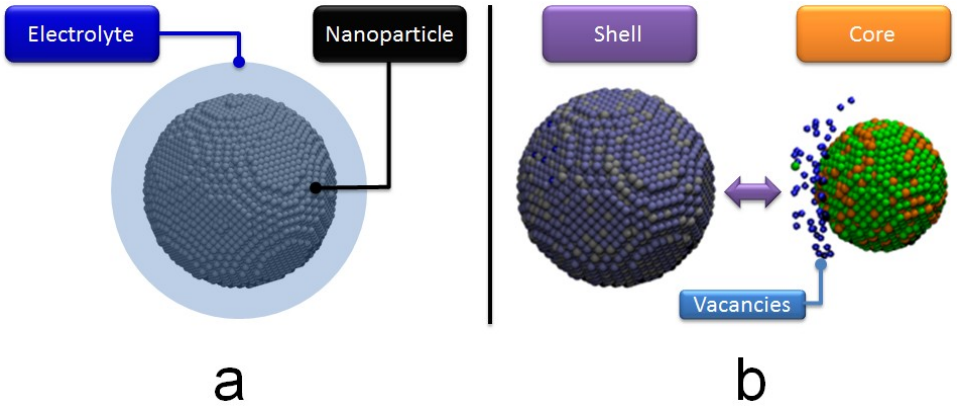

Figure VII-1. Examples of initial configurations for the KMC simulations. (a) Schematic representation of the electrolyte lattice sites surrounding the nanoparticle. (b) multi-metallic systems were considered for the Kirkendall effect simulations, an amount of vacancies were placed in the shell in some cases.

All the species occupy a site in the 3-D simulation lattice and they may participate in the two reactions considered, diffusion and dissolution. The rate $k_{p,i}$ for the reaction p involving site i is calculated with Equation (7.1), where $A_{p,i}$ is the prefactor in sites/s, $E_{B,i}$ is the total bonding energy, given by Equations (7.2) and (7.3), which depends on the number of nearest neighbor sites of type n_j and the pair bonding energy parameter $E_{b,ij}$; $\alpha_{p,i}$ is the transfer coefficient parameter, E is the applied potential, $E_{0p,i}$ is the reference potential, T is the temperature, and k_B is the Boltzmann constant.

$$k_{p,i} = A_{p,i} \exp\left[-\frac{E_{B,i} + \alpha_{p,i}\left(E - E_{0p,i}\right)}{k_B T} \right] \tag{7.1}$$

$$E_{B,i} = \sum_{j}^{\text{Neighbors}} n_j E_{b,ij} \tag{7.2}$$

$$E_{b,ij} = \frac{E_{b,ii} + E_{b,jj}}{2} \tag{7.3}$$

Provided the value of the transfer coefficient $\alpha_{p,i}$, the processes may depend or not on the applied potential. The bonding energy parameters for pure species were calculated from DFT simulations, the change in the total energy of a (111) slab caused by removing an atom from the subsurface layers was divided by the coordination number (12 in the FCC structure). The corresponding bonding parameters for different metals are presented in Table VII-1.

Table VII-1. Bonding parameters for pure metals used in KMC simulations.

Atom i	Bonding parameter $E_{b,ii}$, eV
Pt	0.529
Pd	0.524
Co	0.777
Ni	0.571
Cu	0.382
Rh	0.746
Ir	0.856
Ag	0.285
Au	0.294

The bonding parameters between Pt and the electrolyte were tuned through KMC simulations using the surface diffusion coefficient obtained from experiments[146] and regarded as independent from the applied potential. The effect of the Pt—H_2O bonding parameter on the surface diffusion is shown in Figure VII-2, an average diffusion coefficient of 4.70×10^{-19} cm^2/s corresponds to a solution of 1 M $HClO_4$ and to a Pt—H_2O bonding parameter of 0.384 eV. Using this approach, different electrolytes may be studied by varying the metal—electrolyte bonding parameter. However, in the results reported here a constant value of 0.384 eV was used for all the metals considered.

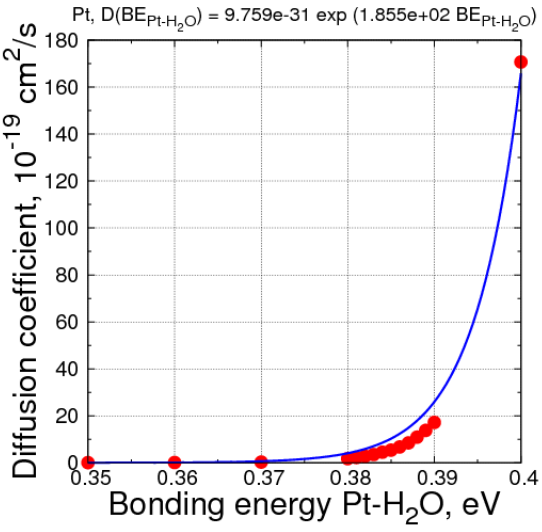

Figure VII-2. Effect of the Pt—H_2O bonding parameter on the surface diffusion of a 40 Å radius nanoparticle. KMC simulation results shown as dots and corresponding fit equation in solid line.

The two processes that are allowed to occur in the KMC simulations are diffusion and dissolution, they are expressed in Equations (7.4) and (7.5), respectively. In the diffusion process two species in neighbor sites exchange coordinates, whereas in the dissolution process a metal site in substituted by an electrolyte site.

$$\text{Diffusion:} \quad \begin{aligned} &\text{species}_1 \text{ at site } i \rightarrow \text{species}_1 \text{ at site } j \\ &\text{species}_2 \text{ at site } j \rightarrow \text{species}_2 \text{ at site } i \end{aligned} \tag{7.4}$$

$$\text{Dissolution:} \quad \text{metal at site } i \rightarrow \text{ electrolyte at site } i \tag{7.5}$$

The selected KMC algorithm was the First-Reaction method[147] (FRM) which is able to simulate processes with time-dependent rates required for the variable potential studies presented in the next section. The FRM has been successfully applied to simulate temperature programmed adsorption and reaction of O_2 on Pt(111) surfaces.[148] The flow diagram of a KMC simulation using the FRM is presented in Figure VII-3, the required random number generator to select the process to occur every simulation step was the Maximally Equidistributed Combined Tausworthe generator by L'Ecuyer.[149,150] An inherent practical issue of the KMC method arises when the studied processes have very different time scales, that is, one process is much faster than the others due to its high

rate. Such fast process occurs in most of the simulation steps, especially using the FRM, consuming practically all the computer time whereas the other processes do not occur, not because they are impossible but due to their lower rate. This problem typically occurs when diffusion is included in the model, as it is in this study which mainly in the nanoparticle—electrolyte interface. The practical solution to this issue is reducing the diffusion rate to make it comparable to that of the other processes,[151,152] the physical interpretation of this approach is to assume that diffusion occurs so fast that it equilibrates the surface before another process has occurred, in such case the precise rate of diffusion is not important. As long as this surface equilibration occurs, the simulation yields correct results.[151] The set of prefactors that were used in Equation (7.1) to evaluate the rates of the considered processes in the cases of study discussed in the next section are shown in Table VII-2. The prefactor for the metal dissolution in the degradation study was tuned to a Pt dissolution rate determined experimentally,[15] whereas for the Kirkendall effect simulations, the prefactors of diffusion and dissolution were adjusted to reproduce the qualitative time scales reported from experiments,[26,153-155] The transfer coefficient for the dissolution processes was set to 0.5 in both cases of study, as well as for the diffusion of core species in the Kirkendall effect simulations, whereas the transfer coefficient of the diffusion processes in the catalyst degradation study was set to 0.0, i.e. the potential has no effect on the diffusion of the species.

Table VII-2. Prefactors used in to evaluate the rates of the considered processes in the cases of study.

Process	Prefactor used in catalyst degradation simulations (sites/s)	Prefactor used in Kirkendall effect simulations (sites/s)
Metal diffusion	1.0×10^{9}	1.0×10^{4}
Metal dissolution	1.0×10^{9}	1.0×10^{4}

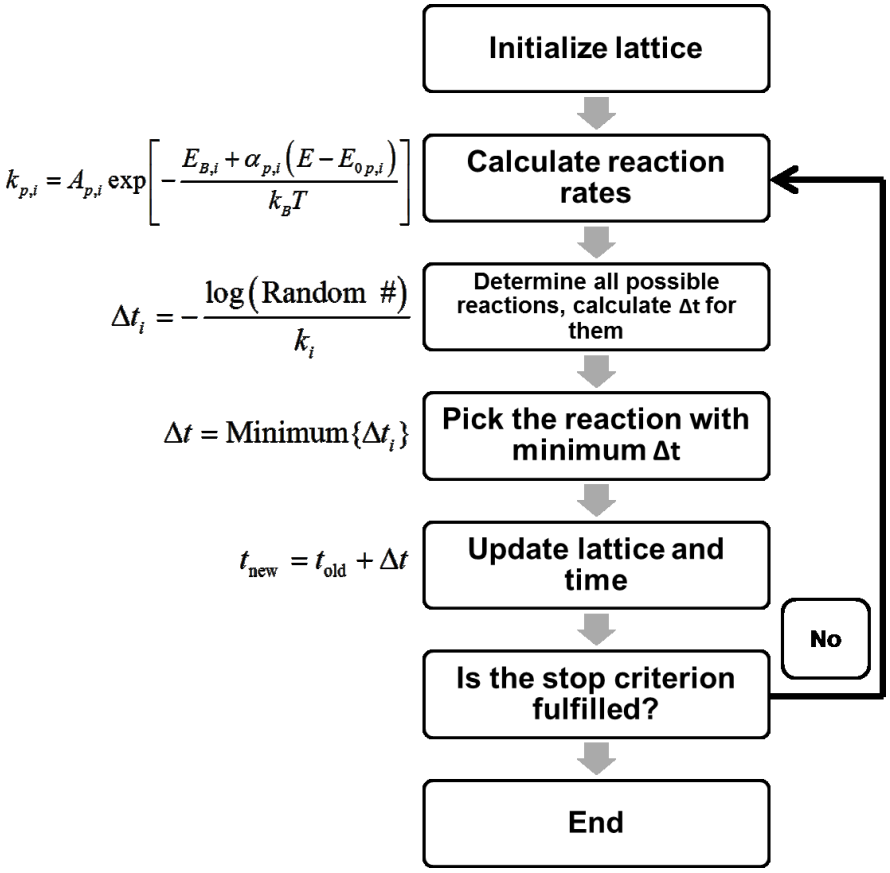

Figure VII-3. Flow diagram of a KMC simulation using the FRM method.

The surface area of the nanoparticle, A, was calculated using Equation (7.6) where a is the lattice parameter, $CN_{\text{fcc}} = 12$ is the maximum coordination number of the FCC structure, and CN_i is the coordination number of the exposed site i. During the simulations the surface atoms, which form the metal—electrolyte interface, were identified and the surface area was calculated to determine changes due to degradation.

$$A = \sum_{i}^{\text{Number of sites}} \underbrace{\left(\frac{CN_{\text{fcc}} - CN_i}{CN_{\text{fcc}}}\right)}_{\text{Exposed fraction based on coordination number}} 4\pi \underbrace{\left(\frac{1}{2}\frac{\sqrt{2}}{2}a\right)^2}_{\text{Metallic radius}} = \sum_{i}^{\text{Number of sites}} \left(1 - \frac{CN_i}{CN_{\text{fcc}}}\right)\frac{\pi a^2}{2} \qquad (7.6)$$

The reference potential for the dissolution of metal species was taken as the standard reduction potential from the literature.[156] Based on the calculated reduction potential as a function of the ion concentration for different metals using the Nernst

equation presented in Figure VII-4, the contribution of the metal ion concentration on the equilibrium potential was neglected in the concentration range of interest for this study.

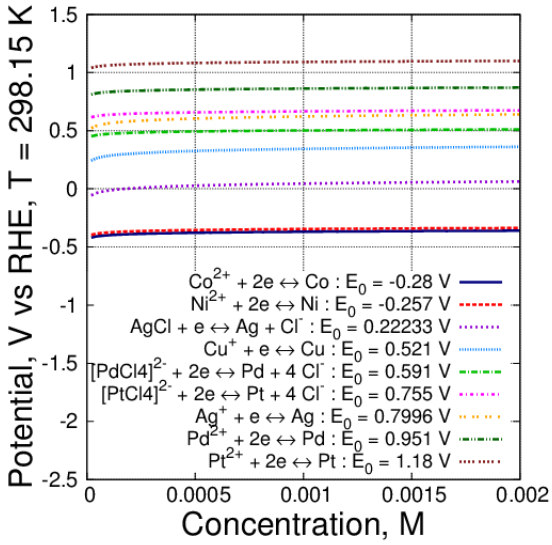

Figure VII-4. Effect of the ion concentration in the reduction potential using the Nernst equation.

VII.3 Results and discussion

In this section we present the two different cases of study that were approached with the KMC method. The results of the degradation of nanoparticles under different electrochemical potential regimes are discussed first. The simulations of the synthesis of hollow nanoparticles by removing the alloy core through dealloying are reported afterwards.

VII.3.1 Catalyst degradation

During the fuel cell operation in cars, the catalyst is exposed to different potential regimes (e.g. during start and stop of the vehicle) with the associated changes in coverage of oxygen. The degradation of the electrode-catalyst is expected to strongly depend on the history of potential to which the catalyst is exposed. In order to analyze this situation, the simulations were carried out under the variable potential regimes

presented in Figure VII-5, as well as under constant potential. Each variable potential regime was repeated during all the simulation period, each regime was studied separately in different runs. It is worth mentioning that in the following results the oxide layer that passivates the surface is not considered. Such layer is formed after a period of time at potentials greater than approximately 0.9 V[15,105] in pure Pt, its effect has an impact on the overall degradation process which needs to be considered in future studies, this issue will be discussed in CHAPTER VIII.

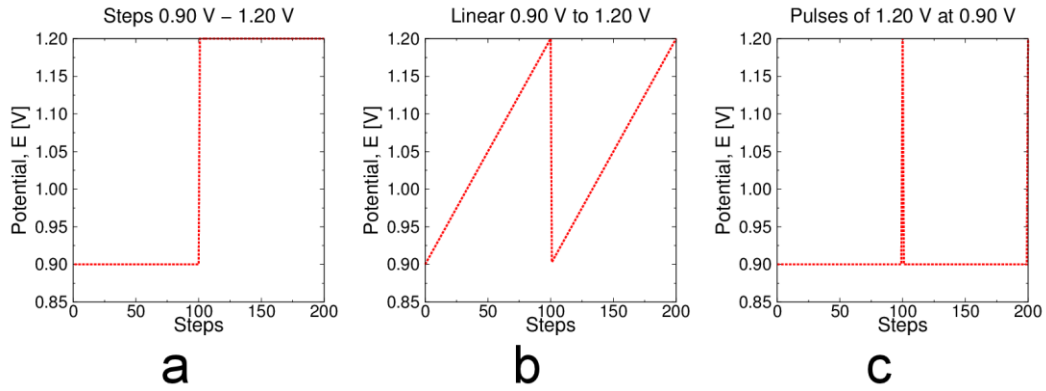

Figure VII-5. Variable potential regimes simulated. (a) Steps 0.9 V—1.20V, (b) linear increase from 0.9 V to 1.2 V, and (c) pulses of 1.2 V at 0.9 V.

The time evolution of the normalized surface area with respect to the initial area and the average coordination number distribution of surface atoms in a Pt nanoparticle under constant potential are presented in Figure VII-6. The nanoparticle under 0.9 V (Figure VII-6a) practically does not show degradation during the simulated time, whereas the systems under 1.1 V and 1.2 V exhibit Pt loss. Such loss is evident in Figure VII-6b and Figure VII-6c as the increase on the normalized area due to the appearance of exposed sites under these conditions which are observed in Figure VII-8, where the corresponding snapshots of the nanoparticles presented. Moreover, the nanoparticle under 1.2 V is completely dissolved after approximately 2.6 days (Figure VII-6c and Figure VII-8, bottom row). The total dissolution of the nanoparticle under 1.2 V occurs after an increase in the normalized area due to the formation of some low coordination sites caused by the dissolution of Pt atoms, followed by a sudden area decrease after 2.5

days of operation (Figure VII-6c) caused by the fast creation of low coordinated sites that are prone to dissolve.

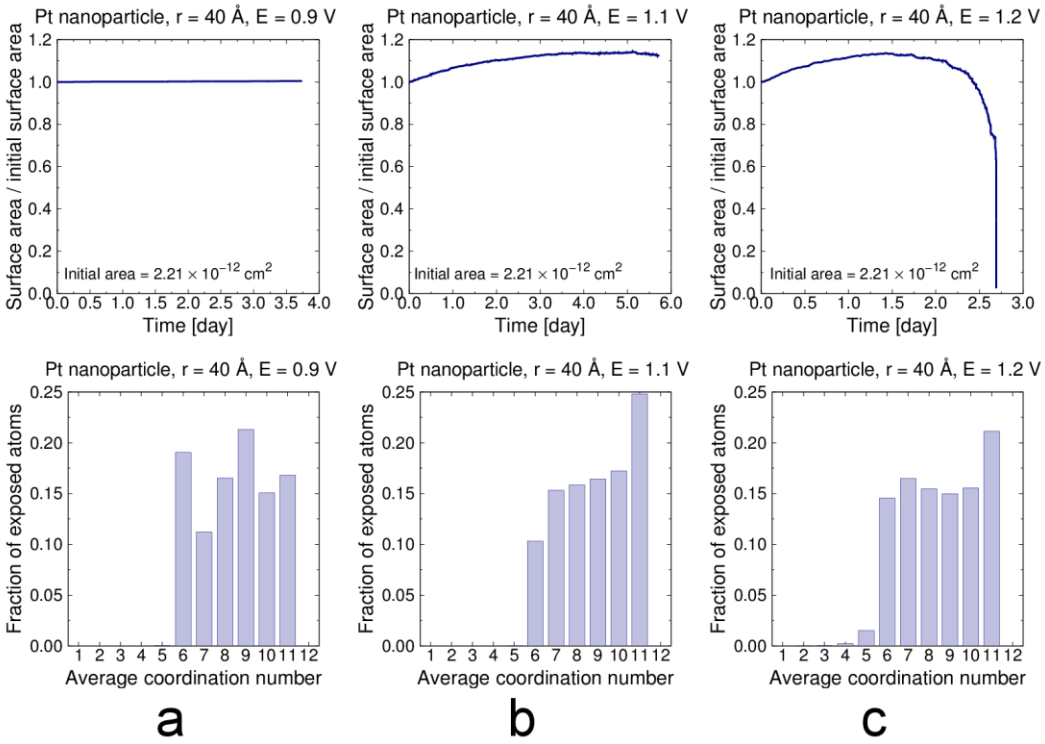

Figure VII-6. Normalized surface area (top row) and average coordination number distribution of surface atoms (bottom row) in a Pt nanoparticle under constant potential. (a) 0.9 V, (b) 1.1 V, and (c) 1.2V.

The average coordination number distributions of the nanoparticles under constant potential are shown in the bottom row of Figure VII-6, to facilitate the discussion a snapshot of a pristine FCC nanoparticle of 40 Å showing the coordination number of the surface atoms is presented in Figure VII-7, a coordination number of 9 corresponds mainly to (111) facets. The nanoparticle under 0.9 V has the typical distribution of a FCC nanoparticle of the corresponding radius with a predominant coordination number of 9 which indicates the presence of (111) facets whose good catalytic properties for the ORR are well known. In contrast, the nanoparticle under 1.1 V shows a higher amount of sites with coordination number of 11, corresponding to atoms only exposed due to the absence of one metal neighbor (red sites in Figure VII-7),

this confirms the removal of the (111) facets observed in Figure VII-8 after approximately 4 days of operation, implying a degradation in the ORR catalytic performance, since it is expected that the abundant step sites that remain in the surface will bind the ORR intermediates stronger, reducing the overall ORR rate.

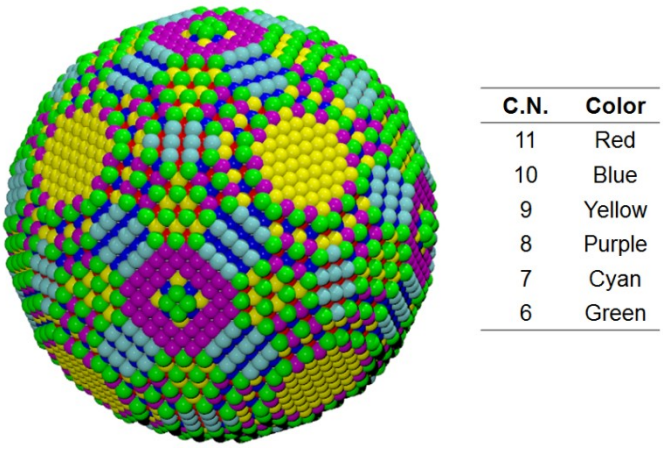

Figure VII-7. Pristine FCC nanoparticle of 40 Å radius showing the coordination number (C.N.) of the surface atoms.

The metal dissolution process involves the low coordinated sites, especially those surrounding the (111) facets. This is observed in Figure VII-9 where the dissolved sites are displayed as a red surface, the effect is more dramatic for the nanoparticle under 1.2 V whose entire initial surface is practically dissolved after 1.4 days of operation.

With the KMC approach discussed here it is possible to determine the dynamic evolution of the coordination number of the exposed atoms on the nanoparticle, as it is depicted in Figure VII-10. For the nanoparticle under 0.9 V whose degradation is negligible, the distribution of the coordination number of the exposed sites is constant with time (Figure VII-10). The particles exposed to higher potentials undergo changes in the distribution of the coordination number with time, showing a growth of the exposed sites and a decrease in the (111) facets due to dissolution. It is expected that such dynamics impacts the ORR performance of the nanoparticle and accelerates its degradation caused by the creation of low-coordinated sites susceptible to dissolve.

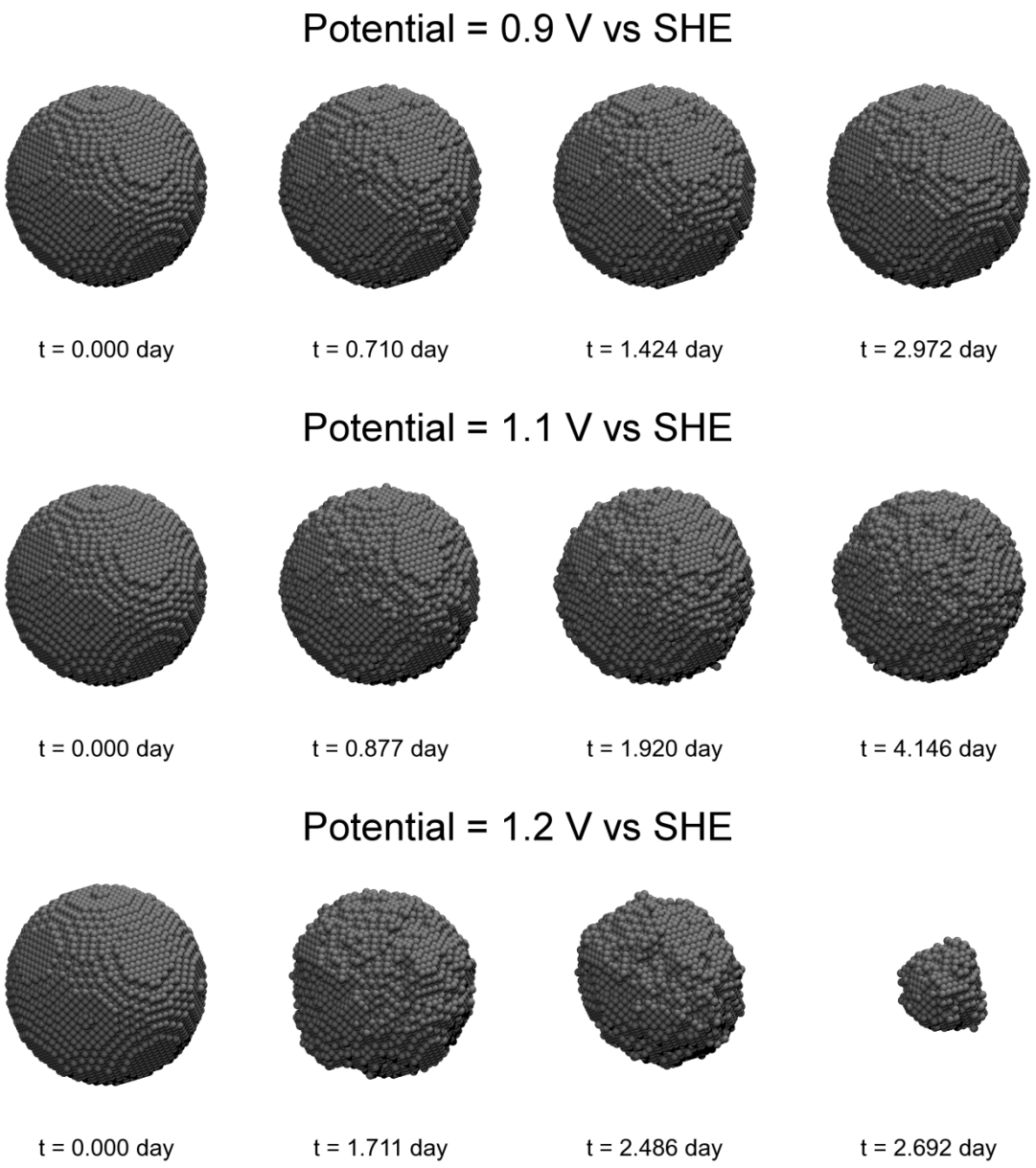

Figure VII-8. Snapshots of a Pt nanoparticle under constant potentials at different times during the simulation, 0.9 V (top row), 1.1 V (middle row), and 1.2 (bottom row).

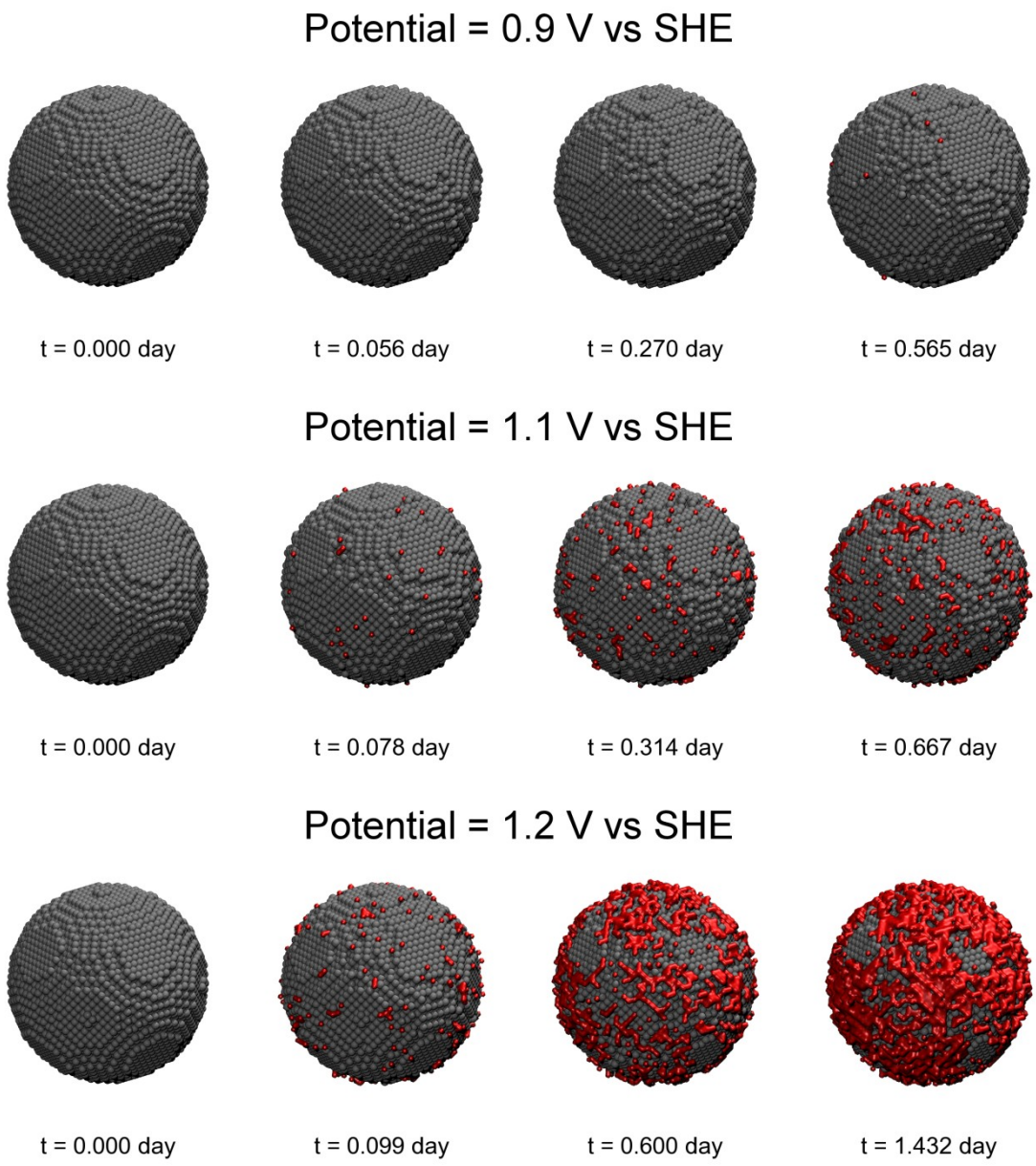

Figure VII-9. Snapshots of a Pt nanoparticle under constant potentials at different times during the simulation showing the dissolved sites (red surface), 0.9 V (top row), 1.1 V (middle row), and 1.2 (bottom row).

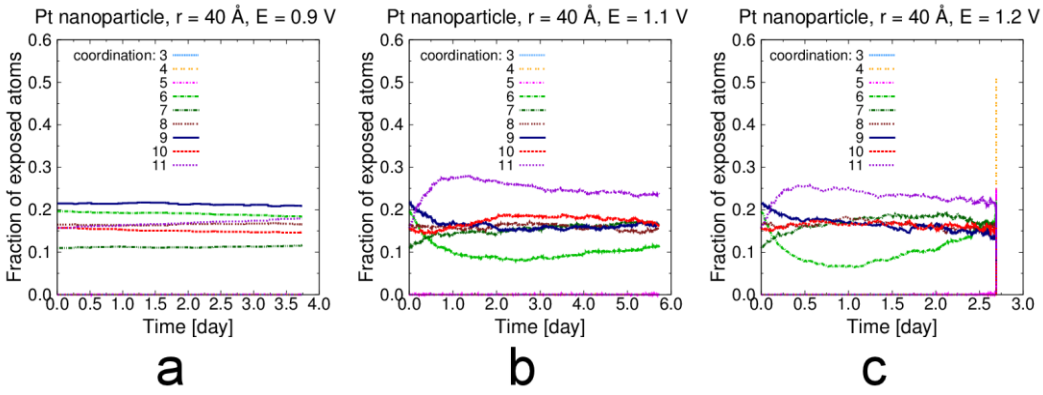

Figure VII-10. Dynamic evolution of the coordination number of surface atoms in a Pt nanoparticle under constant potential. (a) 0.9 V, (b) 1.1 V, and (c) 1.2V.

The effect of the variable potential regimes on the surface area of the nanoparticle is shown in Figure VII-11. All the regimes accelerate the degradation of the nanoparticle with respect to the observed behavior at constant 0.9 V. The pulses of 1.2 V have a slight effect in the degradation within the simulated time but the formation of low-coordinated sites is still noticeable. The nanoparticle under potential steps of 0.9 V and 1.2 V experience total dissolution at approximately 3.30 days, that is a 20% longer life than the nanoparticle operating at constant 1.2 V. Although the nanoparticle exposed to the linear regime did not undergo complete dissolution within the simulated time, one may infer that it will be completely dissolved if the regime continues, based in the increase of the area caused by Pt dissolution.

Figure VII-12 shows the average coordination number distribution of the surface atoms in the nanoparticles under the studied potential regimes. The distribution of the nanoparticles that are dissolved completely within the simulation (constant 1.2 V and steps regime) is very similar, suggesting that the mechanism of dissolution is the same in both cases. The pulses of 1.2 V promote the formation of sites with coordination number of 11 by dissolving the edges of the (111) terraces, whereas the linear and step regimes erode faster the (111) terraces of the nanoparticle which becomes more spherical, as it is observed in the snapshots in Figure VII-13.

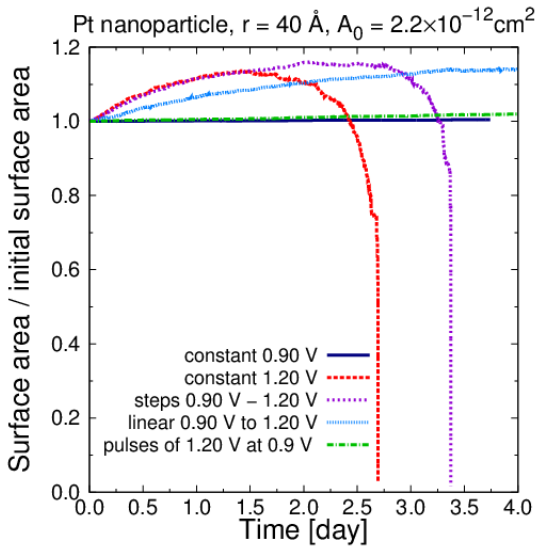

Figure VII-11. Comparison of the normalized surface area loss in a Pt nanoparticle under different variable potential regimes.

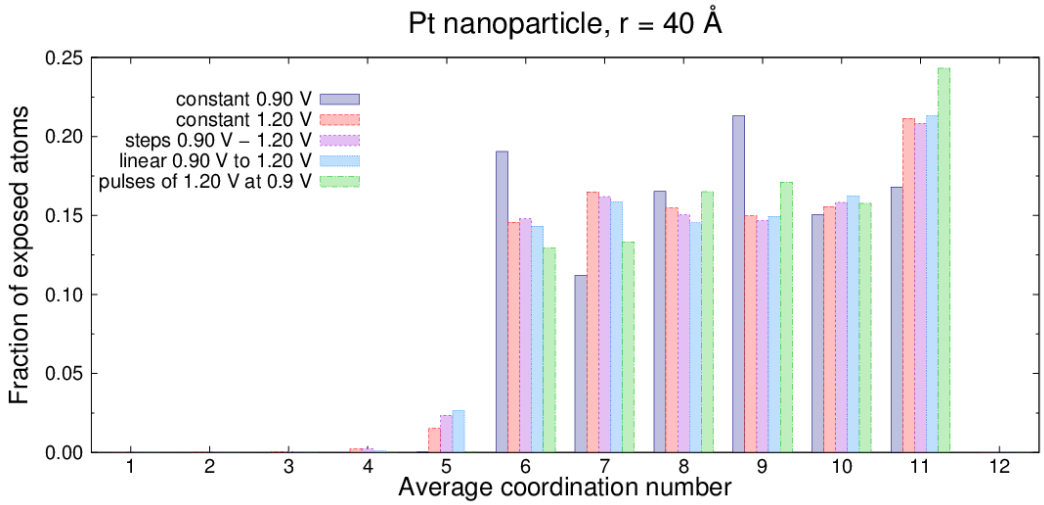

Figure VII-12 Average coordination number distribution of surface atoms in a Pt nanoparticle under different variable potential regimes.

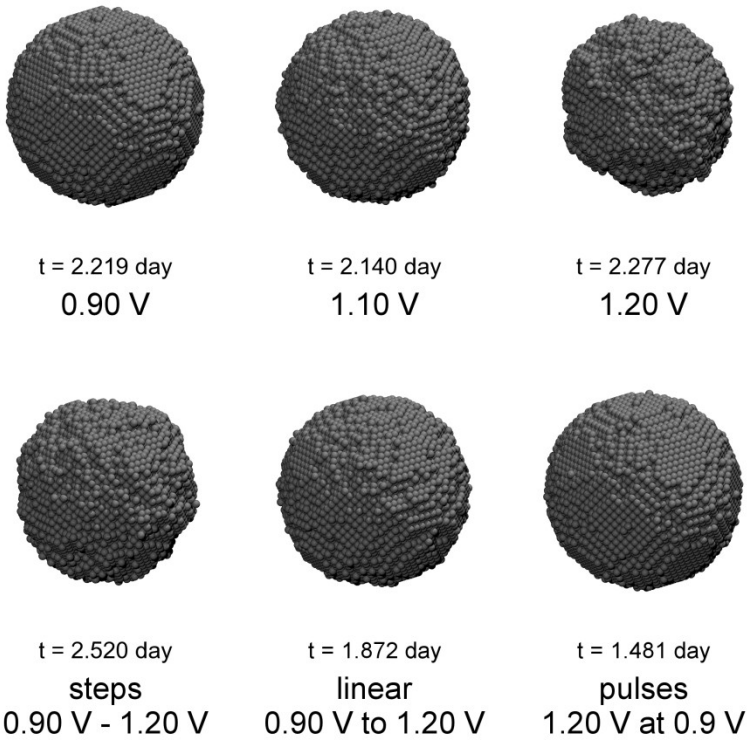

Figure VII-13. Snapshots of a Pt nanoparticle at different times during the simulation under constant (top row) and variable potential (bottom row) regimes.

VII.3.2 Kirkendall effect in hollow catalysts synthesis

The novel and highly active hollow or porous catalysts for different applications have drawn the attention of several experimental reports.[26-28,153,157-160] Here use the KMC method to study specifically the core removal process during the synthesis of Pt-hollow nanoparticles[26] for the ORR. However, the scope of our model can be expanded to simulate the entire synthesis of porous or hollow catalytic nanoparticles, starting from the galvanic replacement, followed by the formation of their characteristic structure through dealloying, until the analysis of their performance during operation.

The synthesis of Pt-hollow nanoparticles[26] with remarkable ORR activity consists in the galvanic replacement from a Ni nanoparticle by Pt atoms, once a Pt-shell/Ni-core nanoparticle is formed, the Ni core is removed by either potential cycling or acid leaching. Such removal of the non-noble metal involves the Kirkendall effect in which the boundary layer between two metals (or alloys) moves as due to the difference

in diffusion rates of the metal atoms. The initial configuration for the KMC simulations was a nanoparticle with a radius of 30 Å, formed by a Ni core of 20 Å surrounded by a Pt shell of 10 Å, as it is shown in Figure VII-14. In order to analyze the effect of vacancies on the core removal process and final structure of the hollow nanoparticle, systems with 1 vacancy per every 100 metal sites in the nanoparticle were considered, such vacancies were placed randomly only in the shell. The bonding parameters required to evaluate Equation (7.1) were set to 0.0 for the vacancies.

The results indicate that the applied potential must enhance the diffusion of the core species. A potential of 12 V is required to remove the Ni core, since the core atoms are strongly bonded to their metal neighbors, such potential is required to cause the diffusion of the core atoms through the shell. The absence of vacancies implies that core atoms must follow a high energy path by exchanging positions directly with other metal atoms. The final structure under these conditions is show in the bottom row of Figure VII-14, it is observed that some Ni atoms remain within the shell after the core is practically removed, in agreement with experimental reports showing a residual amount of Ni after acid leaching[26]. When vacancies are introduced into the system, the core totally removed under the same 12 V of applied potential, as shown in Figure VII-15. The role of the vacancies in the process of removing the core is to create a path with less resistance facilitating the migration of the non-noble atoms to be dissolved. The vacancies remain in the shell and they distribute into it forming some cavities of approximately 5 Å (Figure VII-15c), which may cause an enhancement in the ORR activity[5], in addition to the inherent lattice constraint due to the hollow configuration.

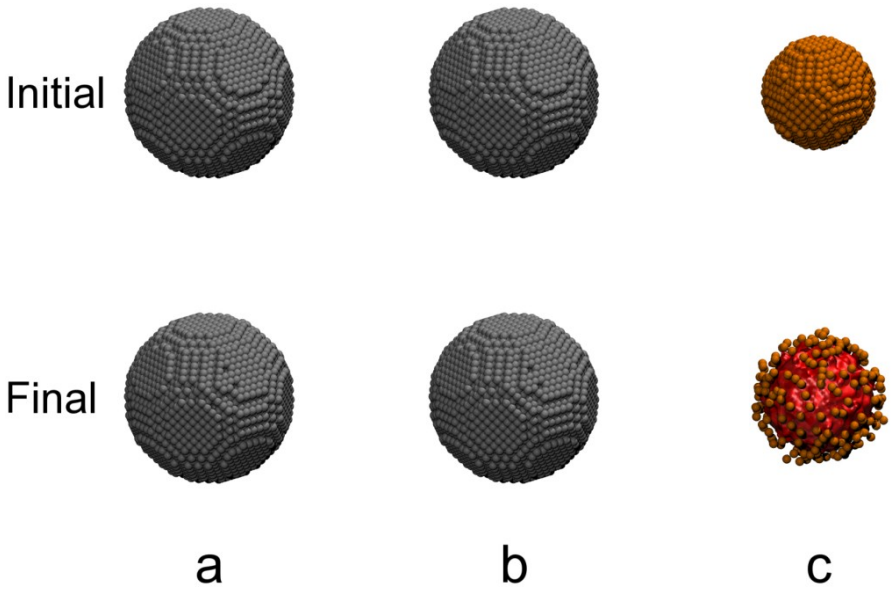

Figure VII-14. Initial and final configurations of the Pt-shell/Ni-core nanoparticle without vacancies. (a) Pt shell, (b) Pt-shell showing the absence of dissolved spots, and (c) Ni core. Pt, and Ni atoms are shown in grey and orange spheres, respectively. The dissolved region is presented as a red surface.

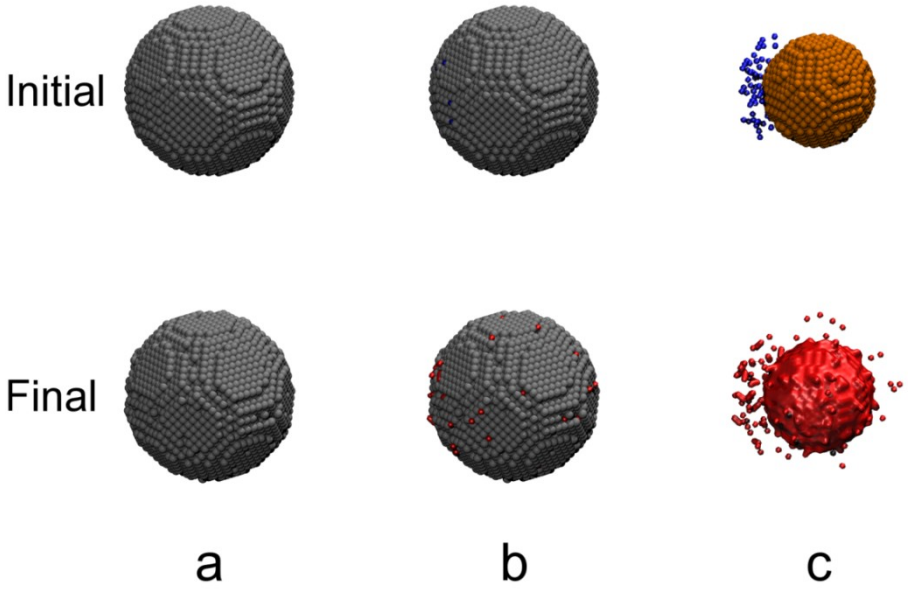

Figure VII-15. Initial and final configurations of the Pt-shell/Ni-core nanoparticle with 0.01 vacancies per metal site in the shell. (a) Pt shell, (b) Pt-shell showing dissolved spots, and (c) Ni core. Pt, and Ni atoms are shown in grey and orange spheres, respectively. The vacancies and dissolved regions are presented as blue and red surfaces, respectively.

The complete dissolution of the Ni core when vacancies are present is observed in the snapshots of regions inside of the hollow nanoparticle at the end of the simulation in Figure VII-16. In the absence of vacancies, Ni is encapsulated within the Pt shell but close to the hollow region (Figure VII-14c and Figure VII-16 top row), the radial distribution functions (RDFs) of Pt—Ni and Ni—Ni shown in Figure VII-17 confirm that the remaining Ni is within the shell creating Ni-rich regions. Similar studies considering a 0.01 composition of Ni in the shell in the initial configuration were conducted, showing equivalent results. Ni remained encapsulated in the absence of vacancies whereas the Ni atoms originally in the shell were dissolved leaving a porous structure. A higher amount of vacancies (0.10 vacancies per site) in the shell was considered as well, it was found that the Ni core was removed entirely in all cases. The remaining shell has a porous structure after the vacancies distribute in it.

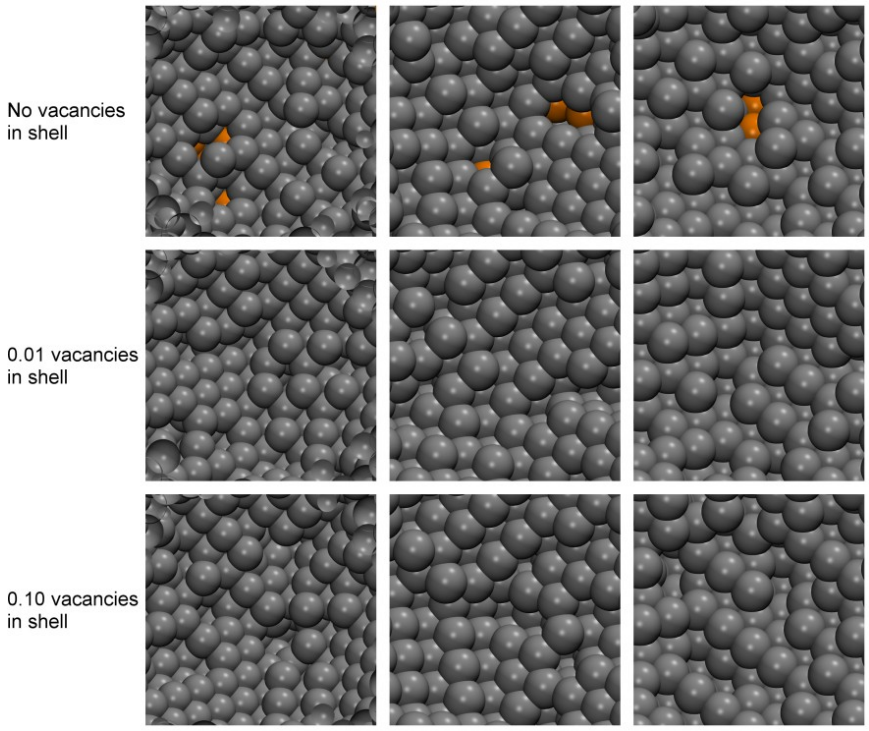

Figure VII-16. Snapshots of the interior of the hollow nanoparticles at the end of the simulation. Each column shows a different region and each row corresponds to a different amount of vacancies in the shell. In the absence of vacancies (top row) Ni remains encapsulated within the shell. Pt and Ni atoms are represented by grey and orange spheres, respectively.

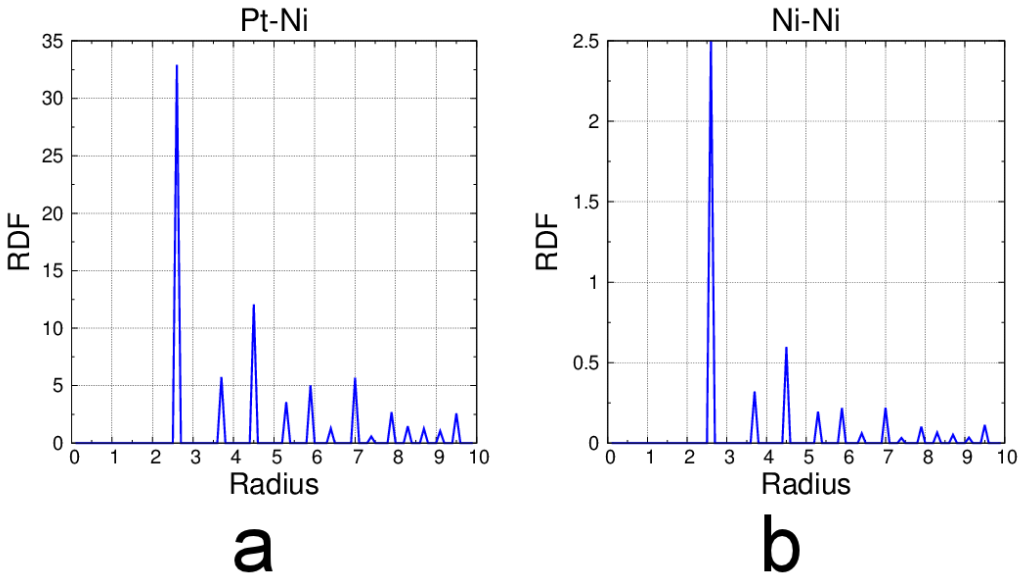

Figure VII-17. Radial distribution function of Pt—Ni of the last configuration in the hollow nanoparticle without vacancies in the shell, in which Ni remain encapsulated.

Since some porous/hollow Pt alloys have demonstrated enhanced ORR activity,[26,28,29,153,157-159] the dealloying process in bimetallic shells on bimetallic cores are interesting systems for further studies. Here the results of a $Pt_{0.25}Pd_{0.75}$ shell on $Ni_{0.25}Cu_{0.75}$ core are presented. The simulations were carried out using the same methodology as discussed above for the Pt-Ni systems. It was found that in the absence of vacancies, the potential of 12 V is not capable of removing the non-noble core due to the higher reduction potential of Cu than the one of Ni (see Figure VII-4). However, when the 0.01 vacancies per site are included in the shell, the hollow nanoparticle is formed, as it is observed in Figure VII-18, the dissolution occurs fast once a channel of vacancies is used by the core atoms that are diffusing though the shell, the preferred sites of the non-noble elements for their dissolution are those with coordination number lower than 9 (see Figure VII-18b and Figure VII-7 as reference). Based on these observations it is expected that the porosity of these nanoparticles do not involve the (111) facets.

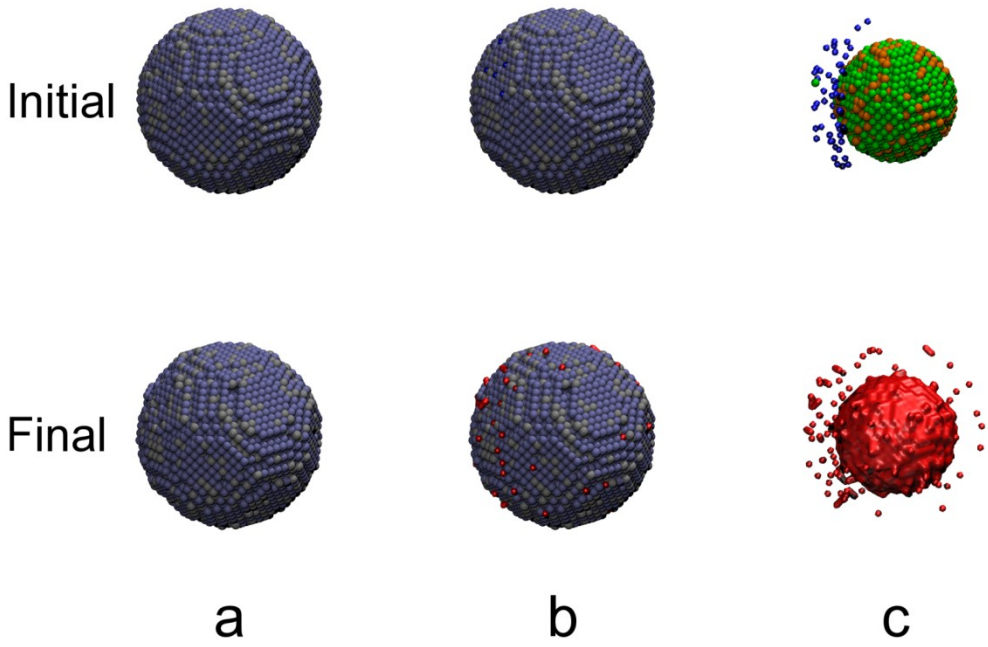

Figure VII-18. Initial and final configurations of the $Pt_{0.25}Pd_{0.75}$-shell/ $Ni_{0.25}Cu_{0.75}$-core nanoparticle with 0.01 vacancies per metal site in the shell. (a) $Pt_{0.25}Pd_{0.75}$ shell, (b) $Pt_{0.25}Pd_{0.75}$ shell showing dissolved spots, and (c) $Ni_{0.25}Cu_{0.75}$ core. Pt, Pd, Ni, and Cu atoms are shown in grey, blue, orange, and green spheres, respectively. The vacancies and dissolved regions are presented as blue and red surfaces, respectively.

CHAPTER VIII
CONCLUSIONS AND RECOMMENDATIONS

The successful application of proton exchange membrane fuel cells in automobiles requires the development of nanocatalysts for the oxygen reduction reaction (ORR) with enhanced activity and sustained durability. In this study we approached the design and analysis of ORR alloy catalysts using molecular simulation, providing insight at molecular level towards the understanding of the relationship between the composition and structure of the catalyst and its activity and resistance to degradation.

The role of the adsorption of oxygen and its effect on surface segregation in (211) surfaces of Pt(shell)/M(core) and Pt_3M (M=Co, Ir) alloys is studied using DFT. It is found that the most energetically favorable oxygen adsorption site is the bridge site over and parallel to the (100) step. The calculated adsorption energies are higher than those reported for Pt(111) surfaces. However, the oxygen binding energy in the Pt/Ir(core) system is only 0.1 eV higher. We observed Pt surface segregation in Pt_3Co and Pt_3Ir taking place through terrace sites, and Co segregation through the step site in Pt/Co(core) structures. The Pt/Ir(core) structure was the only one, among the studied systems, that showed antisegregation behavior of Ir even in presence of oxygen adsorbed. The antisegregation energy in step sites is much higher than that found in (111) surfaces of Pt/Ir(core) systems. The required stability of the Pt shell is one of the most important aspects that are needed for efficient ORR catalysis.

In order to understand the metal dissolution mechanisms, the oxide growth in presence of water on Pt(111) and Pt/PtCo/Pt_3Co(111) surfaces was simulated using classical molecular dynamics. The electrostatic interactions between the adsorbates and the two topmost layers of the surface (that were modeled based on DFT calculations) were crucial for the model to be able of describing the oxidation process. The results indicate that oxygen and water produce changes in the structure and local composition of the near-surface layers which may affect the activity and stability of the catalyst. Such changes are strongly dependent on the amount of adsorbed oxygen and may include the formation of oxide structures in the subsurface layers due to absorption of oxygen at

high coverages. In agreement with previous experimental and theoretical studies of Pt-Co alloys,[52,74,75,83,84,106-108] the results of this work confirm that for the Pt/PtCo/Pt_3Co(111) surface, oxygen enhances the segregation of cobalt to the topmost layer. In addition, calculated Pourbaix diagrams[84,161] have illustrated that oxidized surfaces become favorable at high electrochemical potentials in acid medium, promoting the dissolution of cobalt atoms. Our current results about Co segregation and buckling link the oxidation with the dissolution suggesting a strong effect on the activity and stability of the catalyst, through the formation of surface zones rich in platinum and leaving low-coordinated Pt atoms prone to further dissolution.

Since the role of the oxidation of water molecules and anion interactions may be crucial to the complete understanding of the complex mechanisms of the oxide formation and dissolution of platinum-based alloy catalysts, the interactions between water and the oxidized Pt(111) and Pt/PtCo/Pt_3Co(111) surfaces were studied using MD simulations with the CF1 central force model to represent the dissociation of water molecules under the presence of acid molecules. The water—surface oxide interactions do not affect dramatically the overall structure of the catalyst. However, such interactions define the identity and the amount of ORR intermediates such as OH or H_3O. As has been found experimentally on Pd oxide films,[127] water binds strongly over the surface oxides. Both studied surfaces restructure at high oxidation conditions, forming stepped surfaces similar to a (101) facet. The restructuring process is caused by the absorption of oxygen into the subsurface and by the surface segregation of Co in the alloy system. Thus, strong bonds develop between water and low-coordination metal atoms, inducing the formation of agglomerates of water molecules over regions of the surface. OH and H_3O formation occurs mostly on the boundaries of such regions. The presence of the dissociated acid species enhances water dissociation and again the formation of water clusters on the surface. The proposed model is able to reproduce in a qualitative way the degradation of the catalyst after cycles of reduction and oxidation. The observed increased surface roughness upon cycling has been described from in situ STM observations.[17]

The effect of different surface planes on the oxidation process it is taken into account in the molecular dynamics simulations of the surface oxidation on Pt and Pt/PtCo/Pt_3Co nanoparticles supported over carbon using the CF1 central force model to represent water molecules and considering the presence of acid molecules. It was found that water dissociation occurs only in presence of acid molecules which do not modify the relaxed structure of the nanoparticles. However, the dissociated ions enhance the breaking of OH bonds of water molecules due to electrostatic interactions. The Pt/PtCo/Pt_3Co nanoparticle is more active in terms of water dissociation but it shows a greater area loss after ten cycles of reduction and oxidation. The metal dissolution mechanism after reduction-oxidation cycles in the alloy nanoparticle involves 1) adsorption of oxygen, 2) surface segregation of non-noble alloy atoms, 3) oxygen absorption in the subsurface, 4) destabilization of the oxide phase due to electrostatic interactions with ions in the solvent, and 5) detachment of single metal atoms bonded to oxygen atoms

The relationship between the characteristic structure caused by vacancies in subsurface layers of novel porous/hollow catalysts and their enhanced activity is investigated with DFT calculations. It is concluded that an optimum amount of subsurface vacancies may enhance the ORR activity of Pt-monolayer catalysts over certain alloy cores through changes in the binding energies of O and OH. Specifically, for pure Pt, or cores containing Pd or Ir, the O binding energies become slightly weaker, whereas for cores containing smaller size elements such as Co or Cu, there is a moderate increase of the O binding energies although their values are still much weaker than those on pure Pt. On the other hand, the presence of the subsurface vacancies considerably weakens the OH binding energies for all the studied systems. Analysis of the d-band center shift along with observed geometric changes such as reduction of the Pt—Pt surface distances suggest that both electronic and geometric effects due to the defective structure may result in an effective ORR enhancement. It is noted that the stability of porous nanoparticles requires additional studies, since the migration of atomic oxygen to the subsurface of the catalyst may be facilitated due to the presence of vacancies, as it

was reported before,[24,25,162] causing the nanoparticles to become unstable after cycles of operation.

Finally, the driving forces and the effect of dealloying on the structure of alloy nanocatalysts during their synthesis and operation is studied with the kinetic Monte Carlo method. A versatile a 3-D simulation code is developed whose scope can be expanded to simulate the entire synthesis of porous or hollow catalysts, starting from the galvanic replacement, followed by the formation of their characteristic structure through dealloying, until the analysis of their performance during operation. Two relevant cases of study for the improvement of state-of-the-art ORR catalysts are reported. The studies on the degradation of Pt nanoparticles under different potential regimes demonstrate that the metal dissolution depends on the potential path to which the nanocatalyst is exposed. Moreover, the metal detachment involve low-coordinated sites, especially those in the boundaries of the (111) facets, which are practically dissolved entirely under high potentials, reducing the activity of the nanoparticle since such facets are well known as efficient for the ORR catalysts. On the other hand, the formation of Pt hollow nanoparticles by the Kirkendall effect is studied, the role of vacancies is crucial in the removal of the non-noble core that yields to the hollow nanoparticle. If vacancies are not present, the core atoms must follow a high resistance path and its removal is not complete, whereas the vacancies provide a route that facilitates the diffusion of the core atoms to be dissolved. The remaining vacancies rearrange in the shell forming some cavities, which may cause an enhancement in the ORR activity, in addition to the inherent lattice constraint due to the hollow configuration. The dealloying in nanoparticles with a $Pt_{0.25}Pd_{0.75}$ shell on a $Ni_{0.25}Cu_{0.75}$ core is studied, the dissolution of non-noble atoms occurs fast once a channel of vacancies is used by the atoms that are diffusing through the shell. The dissolution takes pace mainly in low coordination sites.

The KMC simulations of the Pt degradation under operation did not consider the oxide layer that passivates the surface. Such layer is formed after a period of time at potentials greater than approximately 0.9 V in pure Pt, its effect has an impact on the overall degradation process which needs to be considered in future studies. The

implementation of this aspect in the model is not trivial. It is required to take into account the local oxide composition in the rate expressions of diffusion and dissolution. Also, the simulation lattice needs to be modified to allocate the adsorption and absorption sites considering the modification of the surface due to dissolution. Preliminary results presented in Figure VIII-1 demonstrate that the 3-D KMC code is able to take into account such lattice modification, in addition to model ions in the electrolyte which also would improve the accuracy and versatility of the model.

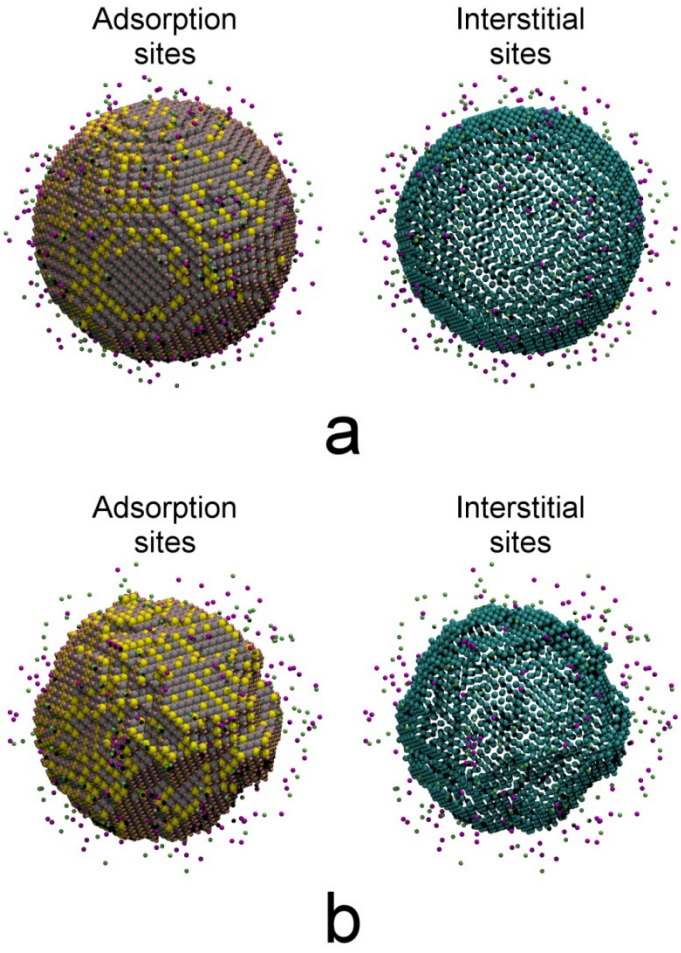

Figure VIII-1. Snapshots displaying the required adsorption (left) and interstitial (right) sites to incorporate the local effect of oxygen and other adsorbates in the KMC simulations. (a) Initial configuration, (b) configuration after metal dissolution. Note how the adsorption sites (pink spheres on the nanoparticle in left images) and interstitial sites (cyan sphere in right images) change as the metal dissolution takes place from (a) to (b). The green and purple spheres around the nanoparticle represent ions in the electrolyte whose effect may be incorporated in the simulations.

The multi-scale approach reported here to study nanocatalysts used in fuel cells may be applied to other areas, such as the improvement of the durability of layered-spinel lithium-ion batteries (LIBs). Specifically, the important problem of voltage decay in novel layered electrodes may be addressed by the elucidation of the structural changes in the electrode due to electrochemical cycling and transport of lithium ions. Since the processes involving Li ions mostly determine the amount of energy obtained from the LIB, the structural rearrangements of the 'layered-spinel' interface in the cathode that impede the transport of lithium ions, decreasing the capacity of the battery may be determined with the molecular simulation techniques presented here. Moreover, the solid-electrolyte interface (SEI) layer may be studied, which is formed by the oxidation of the electrolyte at the cathode surface decreasing the mobility of Li ions. The simulation scheme may involve two levels: 1) DFT calculations to identify i) stable structures of composite cathodes as a function of the Li composition, considering rearrangement of species and different Li-vacancy configurations, ii) oxidation states of the involved elements, and iii) formation of new chemical species involved due to SEI reactions, 2) coarse-grained methods (MD, MC, and KMC) using the information from DFT to consider the effect of temperature, electric potential, larger systems, and long-time scales which cannot be easily included in DFT calculations, thus providing information about structural changes, diffusion of Li through coatings, evolution of the structure and growth of the SEI layer. The multi-scale model may be validated with experimental information such as high-resolution X-ray diffraction, pair distribution function measurements, high-resolution transmission electron microscopy, and voltammetry experiments.

REFERENCES

(1) Wang, B. *Journal of Power Sources* **2005**, *152*, 1.

(2) Stamenkovic, V. R.; Mun, B. S.; Mayrhofer, K. J. J.; Ross, P. N.; Markovic, N. M. *Journal of the American Chemical Society* **2006**, *128*, 8813.

(3) Stamenkovic, V.; Schmidt, T. J.; Ross, P. N.; Markovic, N. M. *The Journal of Physical Chemistry B* **2002**, *106*, 11970.

(4) Duong, H. T.; Rigsby, M. A.; Zhou, W.-P.; Wieckowski, A. *The Journal of Physical Chemistry C* **2007**, *111*, 13460.

(5) Shao, M.; Shoemaker, K.; Peles, A.; Kaneko, K.; Protsailo, L. *Journal of the American Chemical Society* **2010**, *132*, 9253. doi: 10.1021/ja101966a.

(6) Chen, S.; Ferreira, P. J.; Sheng, W.; Yabuuchi, N.; Allard, L. F.; Shao-Horn, Y. *Journal of the American Chemical Society* **2008**, *130*, 13818. doi: 10.1021/ja802513y.

(7) Chen, S.; Sheng, W.; Yabuuchi, N.; Ferreira, P. J.; Allard, L. F.; Shao-Horn, Y. *The Journal of Physical Chemistry C* **2008**, *113*, 1109. doi: 10.1021/jp807143e.

(8) Yang, R.; Leisch, J.; Strasser, P.; Toney, M. F. *ChemInform* **2010**, *41*, no. doi: 10.1002/chin.201046010.

(9) Dutta, I.; Carpenter, M. K.; Balogh, M. P.; Ziegelbauer, J. M.; Moylan, T. E.; Atwan, M. H.; Irish, N. P. *The Journal of Physical Chemistry C* **2010**, *114*, 16309. doi: 10.1021/jp106042z.

(10) Mukerjee, S.; Srinivasan, S.; Soriaga, M. P. *Journal of The Electrochemical Society* **1995**, *142*, 1409.

(11) Paulus, U. A.; Wokaun, A.; Scherer, G. G.; Schmidt, T. J.; Stamenkovic, V.; Markovic, N. M.; Ross, P. N. *Electrochimica Acta* **2002**, *47*, 3787. doi: 10.1016/s0013-4686(02)00349-3.

(12) Toda, T.; Igarashi, H.; Uchida, H.; Watanabe, M. *Journal of The Electrochemical Society* **1999**, *146*, 3750.

(13) Chen, S.; Gasteiger, H. A.; Hayakawa, K.; Tada, T.; Shao-Horn, Y. *Journal of The Electrochemical Society* **2010**, *157*, A82.

(14) Ferreira, P. J.; la O, G. J.; Shao-Horn, Y.; Morgan, D.; Makharia, R.; Kocha, S.; Gasteiger, H. A. *Journal of The Electrochemical Society* **2005**, *152*, A2256.

(15) Wang, X.; Kumar, R.; Myers, D. J. *Electrochemical and Solid-State Letters* **2006**, *9*, A225.

(16) Hyman, M. P.; Medlin, J. W. *The Journal of Physical Chemistry C* **2007**, *111*, 17052. doi: 10.1021/jp075108g.

(17) Wakisaka, M.; Asizawa, S.; Uchida, H.; Watanabe, M. *Physical Chemistry Chemical Physics* **2010**, *12*, 4184.

(18) Gu, Z.; Balbuena, P. B. *Journal of Physical Chemistry A* **2006**, *110*, 9783.

(19) Gu, Z.; Balbuena, P. B. *The Journal of Physical Chemistry C* **2007**, *111*, 9877.

(20) Gu, Z.; Balbuena, P. B. *The Journal of Physical Chemistry C* **2007**, *111*, 17388.

(21) Gu, Z.; Balbuena, P. B. *The Journal of Physical Chemistry C* **2008**, *112*, 5057. doi: 10.1021/jp711875e.

(22) Martínez de la Hoz, J. M.; León-Quintero, D. F.; Hirunsit, P.; Balbuena, P. B. *Chemical Physics Letters* **2010**, *498*, 328. doi: 10.1016/j.cplett.2010.08.083.

(23) Callejas-Tovar, R.; Liao, W.; Mera, H.; Balbuena, P. B. *The Journal of Physical Chemistry C* **2011**, *115*, 23768. doi: 10.1021/jp208286g.

(24) Callejas-Tovar, R.; Liao, W.; Martinez de la Hoz, J. M.; Balbuena, P. B. *The Journal of Physical Chemistry C* **2011**, *115*, 4104. doi: 10.1021/jp110436e.

(25) Callejas-Tovar, R.; Balbuena, P. B. *Physical Chemistry Chemical Physics* **2011**, *13*, 20461. doi: 10.1039/C1CP22490E.

(26) Wang, J. X.; Ma, C.; Choi, Y.; Su, D.; Zhu, Y.; Liu, P.; Si, R.; Vukmirovic, M. B.; Zhang, Y.; Adzic, R. R. *Journal of the American Chemical Society* **2011**, *133*, 13551. doi: 10.1021/ja204518x.

(27) Zhang, H.; Jin, M.; Liu, H.; Wang, J.; Kim, M. J.; Yang, D.; Xie, Z.; Liu, J.; Xia, Y. *ACS Nano* **2011**, *5*, 8212. doi: 10.1021/nn202896q.

(28) Bae, S. J.; Yoo, S. J.; Lim, Y.; Kim, S.; Lim, Y.; Choi, J.; Nahm, K. S.; Hwang, S. J.; Lim, T.-H.; Kim, S.-K.; Kim, P. *Journal of Materials Chemistry* **2012**, *22*, 8820.

(29) Mani, P.; Srivastava, R.; Strasser, P. *Journal of Power Sources* **2011**, *196*, 666. doi: 10.1016/j.jpowsour.2010.07.047.

(30) Principi, E.; Witkowska, A.; Dsoke, S.; Marassi, R.; Di Cicco, A. *Physical Chemistry Chemical Physics* **2009**, *11*, 9987.

(31) Erlebacher, J.; Aziz, M. J.; Karma, A.; Dimitrov, N.; Sieradzki, K. *Nature* **2001**, *410*, 450.

(32) Policastro, S. A.; Carnahan, J. C.; Zangari, G.; Bart-Smith, H.; Seker, E.; Begley, M. R.; Reed, M. L.; Reynolds, P. F.; Kelly, R. G. *Journal of The Electrochemical Society* **2010**, *157*, C328.

(33) Liu, Y.; Bliznakov, S.; Dimitrov, N. *Journal of The Electrochemical Society* **2010**, *157*, K168. doi: 10.1149/1.3454753.

(34) Alayoglu, S.; Nilekar, A. U.; Mavrikakis, M.; Eichhorn, B. *Nature Materials* **2008**, *7*, 333.

(35) Greeley, J.; Mavrikakis, M. *Nat Mater* **2004**, *3*, 810.

(36) Greeley, J.; Mavrikakis, M. *Catalysis Today* **2006**, *111*, 52.

(37) Knudsen, J.; Nilekar, A. U.; Vang, R. T.; Schnadt, J.; Kunkes, E. L.; Dumesic, J. A.; Mavrikakis, M.; Besenbacher, F. *Journal of the American Chemical Society* **2007**, *129*, 6485.

(38) Bhatia, B.; Sholl, D. S. *The Journal of Chemical Physics* **2005**, *122*, 204707.

(39) Antolini, E. *Journal of Materials Science* **2003**, *38*, 2995.

(40) Calvo, S. R.; Balbuena, P. B. *Surface Science* **2007**, *601*, 165.

(41) Calvo, S. R.; Balbuena, P. B. *Surf. Sci.* **2007**, *601*, 4786.

(42) Lamas, E. J.; Balbuena, P. B. *J. Chem. Theor. Comp.* **2006**, *2*, 1388.

(43) Sotelo, J. C.; Seminario, J. M. *Journal of Chemical Physics* **2007**, *127*, 244706.

(44) Sidik, R. A.; Anderson, A. B. *J. Electroanal. Chem.* **2002**, *528*, 69.

(45) Seminario, J. M.; Agapito, L. A.; Yan, L.; Balbuena, P. B. *Chemical Physics Letters* **2005**, *410*, 275.

(46) Xu, Y.; Greeley, J.; Mavrikakis, M. *Journal of the American Chemical Society* **2005**, *127*, 12823.

(47) Gu, Z.; Balbuena, P. B. *The Journal of Physical Chemistry A* **2006**, *110*, 9783.

(48) Nørskov, J. K.; Scheffler, M.; Toulhoat, H. *Mrs Bulletin* **2006**, *31*, 669.

(49) Greeley, J.; Nørskov, J. K. *Surface Science* **2007**, *601*, 1590.

(50) Karlberg, G. S.; Rossmeisl, J.; Nørskov, J. K. *Physical Chemistry Chemical Physics* **2007**, *9*, 5158.

(51) Stamenkovic, V. R.; Fowler, B.; Mun, B. S.; Wang, G.; Ross, P. N.; Lucas, C. A.; Markovic, N. M. *Science (Washington, DC, United States)* **2007**, *315*, 493.

(52) Ma, Y.; Balbuena, P. B. *Surface Science* **2008**, *602*, 107.

(53) Orita, H.; Inada, Y. *The Journal of Physical Chemistry B* **2005**, *109*, 22469.

(54) Kresse, G.; Furthmüller, J. *Phys. Rev. B* **1996**, *54*, 11169.

(55) Kresse, G.; Furthmüller, J. *Computational Materials Science* **1996**, *6*, 15.

(56) Kresse, G.; Hafner, J. *Phys. Rev. B* **1993**, *48*, 13115.

(57) Kresse, G.; Hafner, J. *Phys. Rev. B* **1993**, *47*, 558.

(58) Kresse, G.; Hafner, J. *Phys. Rev. B* **1994**, *49*, 14251.

(59) Blochl, P. E. *Phys. Rev. B* **1994**, *50*, 17953.

(60) Kresse, G.; Joubert, D. *Phys. Rev. B* **1999**, *59*, 1758.

(61) Perdew, J. P.; Burke, K.; Ernzerhof, M. *Phys. Rev. Lett.* **1996**, *77*, 3865.

(62) Kootte, A.; Haas, C.; de Groot, R. A. *Journal of Physics: Condensed Matter* **1991**, *3*, 1133.

(63) Xu, Y.; Ruban, A. V.; Mavrikakis, M. *Journal of the American Chemical Society* **2004**, *126*, 4717.

(64) Bharadwaj, S.; Tripathi, S.; Chandrasekharaiah, M. *Journal of Phase Equilibria* **1995**, *16*, 460.

(65) Wiarda, D.; Raether, F.; Lieb, K. P.; Chevallier, J.; Weyer, G. *Hyperfine Interactions* **1989**, *51*, 893.

(66) Mehl, M. J.; Papaconstantopoulos, D. A. *Phys. Rev. B* **1996**, *54*, 4519.

(67) Kitakami, O.; Sato, H.; Shimada, Y.; Sato, F.; Tanaka, M. *Phys. Rev. B* **1997**, *56*, 13849.

(68) Gambardella, P.; Šljivančanin, Ž.; Hammer, B.; Blanc, M.; Kuhnke, K.; Kern, K. *Physical Review Letters* **2001**, *87*, 056103.

(69) Feibelman, P. J.; Esch, S.; Michely, T. *Phys. Rev. Lett.* **1996**, *77*, 2257.

(70) Gland, J. L. *Surface Science* **1980**, *93*, 487.

(71) Winkler, A.; Guo, X.; Siddiqui, H. R.; Hagans, P. L.; Yates, J. T. *Surface Science* **1988**, *201*, 419.

(72) Yeo, Y. Y.; Vattuone, L.; King, D. A. *The Journal of Chemical Physics* **1997**, *106*, 392.

(73) Ma, Y.; Balbuena, P. B. *The Journal of Physical Chemistry C* **2008**, *112*, 14520.

(74) Menning, C. A.; Hwu, H. H.; Chen, J. G. *The Journal of Physical Chemistry B* **2006**, *110*, 15471.

(75) Menning, C. A.; Chen, J. G. *The Journal of Chemical Physics* **2008**, *128*, 164703.

(76) Ramirez-Caballero, G. E.; Balbuena, P. B. *Chemical Physics Letters* **2008**, *456*, 64.

(77) Strasser, P.; Koh, S.; Greeley, J. *Physical Chemistry Chemical Physics* **2008**, *10*, 3670.

(78) Imai, H.; Izumi, K.; Matsumoto, M.; Kubo, Y.; Kato, K.; Imai, Y. *Journal of the American Chemical Society* **2009**, *131*, 6293. doi: 10.1021/ja810036h.

(79) Uchimura, M.; Sugawara, S.; Suzuki, Y.; Zhang, J.; Kocha, S. S. *ECS Transactions* **2008**, *16*, 225.

(80) Smith, W.; Forester, T. R. *Journal of Molecular Graphics* **1996**, *14*, 136.

(81) Smith, W.; Todorov, I. T. *Molecular Simulation* **2006**, *32*, 935.

(82) Smith, W.; Yong, C. W.; Rodger, P. M. *Molecular Simulation* **2002**, *28*, 385.

(83) Ma, Y.; Balbuena, P. B. *Surface Science* **2009**, *603*, 349.

(84) Hirunsit, P.; Balbuena, P. B. *Surface Science* **2009**, *603*, 912.

(85) Rafii-Tabar, H.; Sulton, A. P. *Philosophical Magazine Letters* **1991**, *63*, 217. doi: 10.1080/09500839108205994.

(86) Sutton, A. P.; Chen, J. *Philosophical Magazine Letters* **1990**, *61*, 139.

(87) Liem, S. Y.; Chan, K.-Y. *Surface Science* **1995**, *328*, 119. doi: 10.1016/0039-6028(95)00016-x.

(88) Wu, G.-W.; Chan, K.-Y. *Journal of Electroanalytical Chemistry* **1998**, *450*, 225.

(89) Kaszkur, Z. A.; Mierzwa, B. *Philosophical Magazine A* **1998**, *77*, 781.

(90) Berendsen, H. J. C.; Grigera, J. R.; Straatsma, T. P. *The Journal of Physical Chemistry* **1987**, *91*, 6269.

(91) Ewald, P. P. *Ann. Phys.* **1921**, *369*, 253.

(92) Rapaport, D. C. *Art of Molecular Dynamics Simulation*; Cambridge University Press, 2004.

(93) Henkelman, G.; Jónsson, H.; Arnaldsson, A.; Uberuaga, B.; Stier, W. Transition State Tools for VASP; http://theory.cm.utexas.edu/vtsttools/, 2010.

(94) Tang, W.; Sanville, E.; Henkelman, G. *Journal of Physics: Condensed Matter* **2009**, *21*, 084204.

(95) Sanville, E.; Kenny, S. D.; Smith, R.; Henkelman, G. *Journal of Computational Chemistry* **2007**, *28*, 899.

(96) Henkelman, G.; Arnaldsson, A.; Jónsson, H. *Computational Materials Science* **2006**, *36*, 354.

(97) Hafner, J. *Computer Physics Communications* **2007**, *177*, 6.

(98) Humphrey, W.; Dalke, A.; Schulten, K. *Journal of Molecular Graphics* **1996**, *14*, 33.

(99) Williams, T.; Kelley, C.; et al. Gnuplot 4.4: an interactive plotting program; http://gnuplot.sourceforge.net/, 2010.

(100) Project, s. sK1 illustration program; http://sk1project.org/index.php, 2010.

(101) Nagy, Z.; You, H. *Electrochimica Acta* **2002**, *47*, 3037. doi: 10.1016/s0013-4686(02)00223-2.

(102) Teliska, M.; Murthi, V. S.; Mukerjee, S.; Ramaker, D. E. *The Journal of Physical Chemistry C* **2007**, *111*, 9267.

(103) You, H.; Zurawski, D. J.; Nagy, Z.; Yonco, R. M. *The Journal of Chemical Physics* **1994**, *100*, 4699.

(104) Kikuchi, H.; Ouchida, W.; Nakamura, M.; Goto, C.; Yamada, M.; Hoshi, N. *Electrochemistry Communications* **2010**, *12*, 544.

(105) Jerkiewicz, G.; Vatankhah, G.; Lessard, J.; Soriaga, M. P.; Park, Y.-S. *Electrochimica Acta* **2004**, *49*, 1451.

(106) Hirunsit, P.; Balbuena, P. B. *Surface Science* **2009**, *603*, 3239. doi: 10.1016/j.susc.2009.09.011.

(107) Ramirez-Caballero, G. E.; Ma, Y.; Callejas-Tovar, R.; Balbuena, P. B. *Physical Chemistry Chemical Physics* **2010**, *12*, 2209. doi: 10.1039/B917899F.

(108) Ruban, A. V.; Skriver, H. L.; Nørskov, J. K. *Physical Review B* **1999**, *59*, 15990.

(109) Darling, R. M.; Meyers, J. P. *Journal of The Electrochemical Society* **2003**, *150*, A1523.

(110) Hawkins, J. M.; Weaver, J. F.; Asthagiri, A. *Physical Review B* **2009**, *79*, 125434.

(111) Martínez de la Hoz, J. M.; León-Quintero, D. F.; Hirunsit, P.; Balbuena, P. B. *Chemical Physics Letters* **2010**, *498*, 328. doi: 10.1016/j.cplett.2010.08.083.

(112) Balbuena, P. B.; Calvo, S. R.; Callejas-Tovar, R.; Gu, Z.; Ramirez-Caballero, G. E.; Hirunsit, P.; Ma, Y. *Challenges in the Design of Active and Durable Alloy Nanocatalysts for Fuel Cells: Theory and Experiment in Electrocatalysis*; Springer New York, 2010. doi: 10.1007/978-1-4419-5594-4_9.

(113) Getman, R. B.; Xu, Y.; Schneider, W. F. *The Journal of Physical Chemistry C* **2008**, *112*, 9559. doi: 10.1021/jp800905a.

(114) Hirunsit, P.; Balbuena, P. B. *The Journal of Physical Chemistry C* **2010**, *114*, 13055. doi: 10.1021/jp1033728.

(115) Duh, D.-M.; Perera, D. N.; Haymet, A. D. J. *The Journal of Chemical Physics* **1995**, *102*, 3736.

(116) Stillinger, F. H.; Rahman, A. *The Journal of Chemical Physics* **1978**, *68*, 666.

(117) Hofmann, D.; Kuleshova, L.; D'Aguanno, B. *Journal of Molecular Modeling* **2008**, *14*, 225. doi: 10.1007/s00894-007-0265-9.

(118) Haymet, A. D. J. *Journal of Molecular Liquids* **1995**, *65–66*, 139. doi: 10.1016/0167-7322(95)00848-8.

(119) Arthur, J. W.; Haymet, A. D. J. *Fluid Phase Equilibria* **1998**, *150-151*, 91. doi: 10.1016/s0378-3812(98)00279-9.

(120) Balbuena, P. B.; Johnston, K. P.; Rossky, P. J. *The Journal of Physical Chemistry* **1996**, *100*, 2706. doi: 10.1021/jp952194o.

(121) David, R. L. *CRC Handbook of Chemistry and Physics: Molecular Structure and Spectroscopy*, 91 ed.; CRC, 2011.

(122) Gutberlet, A.; Schwaab, G.; Birer, Ö.; Masia, M.; Kaczmarek, A.; Forbert, H.; Havenith, M.; Marx, D. *Science* **2009**, *324*, 1545. doi: 10.1126/science.1171753.

(123) Koper, M. T. M. *Fuel Cell Catalysis: A Surface Science Approach*; Wiley, 2009.

(124) Chen, S.; Sheng, W.; Yabuuchi, N.; Ferreira, P. J.; Allard, L. F.; Shao-Horn, Y. *The Journal of Physical Chemistry C* **2009**, *113*, 1109.

(125) Ogasawara, H.; Yoshinobu, J.; Kawai, M. *Chemical Physics Letters* **1994**, *231*, 188. doi: 10.1016/0009-2614(94)01251-2.

(126) Han, B. C.; Miranda, C. R.; Ceder, G. *Physical Review B* **2008**, *77*, 075410.

(127) Kan, H. H.; Colmyer, R. J.; Asthagiri, A.; Weaver, J. F. *The Journal of Physical Chemistry C* **2009**, *113*, 1495. doi: 10.1021/jp808008k.

(128) Gong, Y.; Zhou, M. *ChemPhysChem* **2010**, *11*, 1888. doi: 10.1002/cphc.201000104.

(129) Ataka, K.-i.; Yotsuyanagi, T.; Osawa, M. *The Journal of Physical Chemistry* **1996**, *100*, 10664. doi: 10.1021/jp953636z.

(130) Callejas-Tovar, R.; Balbuena, P. B. *Surface Science* **2008**, *602*, 3531 doi: 10.1016/j.susc.2007.09.052.

(131) Huang, S.-P.; Balbuena, P. B. *Molecular Physics* **2002**, *100*, 2165.

(132) Maillard, F.; Dubau, L.; Durst, J.; Chatenet, M.; André, J.; Rossinot, E. *Electrochemistry Communications* **2010**, *12*, 1161. doi: 10.1016/j.elecom.2010.06.007.

(133) Dubau, L.; Maillard, F.; Chatenet, M.; André, J.; Rossinot, E. *Electrochimica Acta* **2010**, *56*, 776. doi: 10.1016/j.electacta.2010.09.038.

(134) Matsumoto, M.; Miyazaki, T.; Imai, H. *The Journal of Physical Chemistry C* **2011**, *115*, 11163. doi: 10.1021/jp201959h.

(135) Snyder, J.; Asanithi, P.; Dalton, A. B.; Erlebacher, J. *Advanced Materials* **2008**, *20*, 4883. doi: 10.1002/adma.200702760.

(136) Greeley, J.; Stephens, I. E. L.; Bondarenko, A. S.; Johansson, T. P.; Hansen, H. A.; Jaramillo, T. F.; Rossmeisl, J.; Chorkendorff, I.; Nørskov, J. K. *Nature Chemistry* **2009**, *1*, 552. doi: 10.1038/nchem.367.

(137) Strasser, P.; Koh, S.; Anniyev, T.; Greeley, J.; More, K.; Yu, C. F.; Liu, Z. C.; Kaya, S.; Nordlund, D.; Ogasawara, H.; Toney, M. F.; Nilsson, A. *Nature Chemistry* **2010**, *2*, 454. doi: 10.1038/nchem.623.

(138) Nørskov, J. K.; Rossmeisl, J.; Logadottir, A.; Lindqvist, L.; Kitchin, J. R.; Bligaard, T.; Jónsson, H. *The Journal of Physical Chemistry B* **2004**, *108*, 17886. doi: 10.1021/jp047349j.

(139) Nørskov, J. K.; Bligaard, T.; Logadottir, A.; Bahn, S.; Hansen, L. B.; Bollinger, M.; Bengaard, H.; Hammer, B.; Sljivancanin, Z.; Mavrikakis, M.; Xu, Y.; Dahl, S.; Jacobsen, C. J. H. *Journal of Catalysis* **2002**, *209*, 275.

(140) Monkhorst, H. J.; Pack, J. D. *Physical Review B* **1976**, *13*, 5188.

(141) Methfessel, M.; Paxton, A. T. *Physical Review B* **1989**, *40*, 3616.

(142) Kitchin, J. R.; Nørskov, J. K.; Barteau, M. A.; Chen, J. G. *The Journal of Chemical Physics* **2004**, *120*, 10240.

(143) Hammer, B.; Nørskov, J. K. *Surface Science* **1995**, *343*, 211.

(144) Wang, Y.; Balbuena, P. B. *The Journal of Physical Chemistry B* **2005**, *109*, 18902. doi: 10.1021/jp0543779.

(145) Nilekar, A.; Xu, Y.; Zhang, J.; Vukmirovic, M.; Sasaki, K.; Adzic, R.; Mavrikakis, M. *Topics in Catalysis* **2007**, *46*, 276.

(146) Hidalgo, M.; Marcos, M. L.; Velasco, J. G. *Applied Physics Letters* **1995**, *67*, 1486.

(147) Gillespie, D. T. *The Journal of Physical Chemistry* **1977**, *81*, 2340.

(148) Mainardi, D. S.; Calvo, S. R.; Jansen, A. P. J.; Lukkien, J. J.; Balbuena, P. B. *Chemical Physics Letters* **2003**, *382*, 553.

(149) L'Ecuyer, P. *Math. Comput.* **1996**, *65*, 203. doi: 10.1090/s0025-5718-96-00696-5.

(150) L'Ecuyer, P. *Math. Comput.* **1999**, *68*, 261.

(151) Jansen, A. P. J. An Introduction To Monte Carlo Simulations Of Surface Reactions; eprint arXiv:cond-mat/0303028, 2003.

(152) Jansen, A. P. J.; Lukkien, J. J. *Catalysis Today* **1999**, *53*, 259.

(153) Hong, J. W.; Kang, S. W.; Choi, B.-S.; Kim, D.; Lee, S. B.; Han, S. W. *ACS Nano* **2012**, *6*, 2410. doi: 10.1021/nn2046828.

(154) Dubau, L.; Durst, J.; Maillard, F.; Guétaz, L.; Chatenet, M.; André, J.; Rossinot, E. *Electrochimica Acta* **2011**, *56*, 10658. doi: 10.1016/j.electacta.2011.03.073.

(155) Yin, Y.; Rioux, R. M.; Erdonmez, C. K.; Hughes, S.; Somorjai, G. A.; Alivisatos, A. P. *Science* **2004**, *304*, 711. doi: 10.1126/science.1096566.

(156) David, R. L. *CRC Handbook of Chemistry and Physics: Electrochemical Series*, 90 ed.; CRC, 2010.

(157) Xu, C.; Liu, Y.; Wang, J.; Geng, H.; Qiu, H. *ACS Applied Materials & Interfaces* **2011**, *3*, 4626. doi: 10.1021/am201057t.

(158) Qiu, H.; Huang, X. *Journal of Materials Chemistry* **2012**, *22*, 7602.

(159) Qiu, H.; Zou, F. *ACS Applied Materials & Interfaces* **2012**, *4*, 1404. doi: 10.1021/am201659n.

(160) Rabis, A.; Rodriguez, P.; Schmidt, T. J. *ACS Catalysis* **2012**, 864. doi: 10.1021/cs3000864.

(161) Hansen, H. A.; Rossmeisl, J.; Nørskov, J. K. *Physical Chemistry Chemical Physics* **2008**, *10*, 3722.

(162) Balbuena, P.; Callejas-Tovar, R.; Hirunsit, P.; Martínez de la Hoz, J.; Ma, Y.; Ramírez-Caballero, G. *Topics in Catalysis* **2012**, *55*, 322. doi: 10.1007/s11244-012-9800-8.